Universidade Federal do Rio de Janeiro
Centro de Ciências Matemáticas e da Natureza
Observatório do Valongo

Galaxy Mass Evolution from a Cosmological Perspective

Doctorate thesis
of

Amanda Reis Lopes

Supervisors: Marcelo Byrro Ribeiro and Carlotta Gruppioni

Rio de Janeiro/2016

Amanda Reis Lopes

GALAXY MASS EVOLUTION FROM A COSMOLOGICAL PERSPECTIVE

Tese de doutorado apresentada ao Programa de Pós-graduação em Astronomia do Observatório do Valongo, da Universidade Federal do Rio de Janeiro, como parte dos requisitos necessários a obtenção do título de doutor em Ciências - Astronomia.

Orientador: Prof. Dr. Marcelo Byrro Ribeiro
Co-orientadora: Dra. Carlotta Gruppioni

Rio de Janeiro
Maio de 2016

Galaxy Mass Evolution from a Cosmological Perspective

Amanda Reis Lopes

Dr. Marcelo Byrro Ribeiro (Orientador)
Dra. Carlotta Gruppioni (Coorientadora)

Tese de doutorado submetida ao Programa de Pós-Graduação em Astronomia, Observatório do Valongo, da Universidade Federal do Rio de Janeiro - UFRJ, como parte dos requisitos necessários à obtenção do título de Doutora em Ciências - Astronomia.

Aprovada por:

Presidente, Prof. Dr. Marcelo Byrro Ribeiro(Orientador) – IF-OV/UFRJ

Prof. Dr. José Carlos Neves de Araújo– (Avaliador Externo) – INPE

Prof. Dr. Maurício Ortiz Calvão - (Avaliador Externo) - IF/RJ

Prof. Dr. Miguel Boavista Quartin – (Avaliador Interno) – IF-OV/UFRJ

Prof. Dr. Ribamar Rondon de Rezende dos Reis – (Avaliador Interno) – IF-OV/UFRJ

Rio de Janeiro
Maio de 2016

Lopes, Amanda Reis

L864g Galaxy Mass Evolution from a Cosmological Perspective / Amanda Reis Lopes - Rio de Janeiro: UFRJ/OV, 2016.

xiv, 110f.:il; 30cm.

Orientador: Marcelo Byrro Ribeiro

Coorientadora: Carlotta Gruppioni

Tese (doutorado) - Universidade Federal do Rio de Janeiro, Observatório do Valongo, Programa de Pós-graduação em Astronomia, 2016.

Referências Bibliográficas: f:103-112.

1. Galáxias: Função de Massa 2. Cosmologia: Teoria 3. Galáxias: Formação I. Ribeiro, Marcelo Byrro, orient. II. Gruppioni, Carlotta, coorient. III. Título.

This thesis is dedicated to the memory of my parents, John Milton da Silveira Lopes and Ademilde de Barros Reis. Saudades.

"Life is a play that does not allow testing. So, sing, cry, dance, laugh and live intensily, before the curtain closes and the piece ends with no applause."

Anonymous author, usually attributed to Charlie Chaplin

"Cada um de nós é um grão de pó que o vento da vida levanta, e depois deixa cair."

Fernando Pessoa

Acknowledgements

I would to thank my family for unconditional support and patience throughout these four years of dedication to my PhD. A special thanks to my sister Juliana Reis Lopes, who half-way through this journey started to live with me and had to deal with crazy routines of work, eventual bad moods and a lot of complaints, and to my niece Indaiá Lopes Oliveira, who is a constant source of inspiration for me to become a better person and to set a good example.

To my parents, John Milton da Silveira Lopes and Ademilde Barros Reis, for the life lessons and love that will last a lifetime and for teaching me to never give up on my goals and dreams. I will forever miss them and shall always see them as a reference of professionalism and character.

To my supervisor, Marcelo Byrro Ribeiro, for never ending patience and support during these four years, especially on a phase when a lot of personal and technical problems appeared, leading to a big delay on the work progress. This thesis would not be possible without him, and words are no enough to express my gratitude.

To Carlotta Gruppioni, my co-supervisor who accepted to work with me in a heartbeat and made me feel very welcome during my time in Bologna Astronomical Observatory (OABO), and Lucia Pozzetti. Both of them are amazing people who I had the honor and pleasure to get to know and work with in Bologna for a year.

To my best friend Tatiana Moura, who besides the distance had always have the time and patience to listen to my never ending complains and moments of doubt and despair. Thank you for everything.

To my office mates and graduate fellows on OABO and Valongo Observatory (OV) for the friendship and helpful discussions.

To all teachers and staff on OV and OABO for the productive work environment in both institutes.

I acknowledge the financial support from Fundação de Apoio à Pesquisa do Estado do Rio de Janeiro (FAPERJ) and Coordenação de Aperfeiçoamento de Pessoal de Nível Superior (CAPES) for three years of my PhD in Brazil and one year in Italy, respectively.

Abstract

GALAXY MASS EVOLUTION FROM A COSMOLOGICAL PERSPECTIVE

Amanda Reis Lopes
Supervisors: Marcelo Byrro Ribeiro and Carlotta Gruppioni

Abstract of the PhD thesis submitted to the graduate program in Astronomy, Valongo Observatory, at the Federal University of Rio de Janeiro - UFRJ, as part of the necessary requirements for obtaining a Doctoral Degree in Science - Astronomy.

The goal of this work is to analyze the mass evolution of galaxies from a cosmological perspective. This thesis is organized in two parts: the first describes the effect of different cosmologies on the galaxy stellar mass function (GSMF), and the second discusses an alternative tool to analyze the galaxy mass evolution based on a semi-empirical relativistic approach that uses observational data provided by galaxy redshift surveys, the galaxy cosmological mass function (GCMF).

In the first topic, the GSMF is computed for a sample of about 220,000 K_S-band selected galaxies from the UltraVISTA survey up to $z \sim 4$, assuming the observationally constrained Lemaître-Tolman-Bondi (LTB) "giant-void" and the standard model. Then, three separated analysis were made based on full, red and blue samples, to verify a possible change in the galaxy evolution scenario caused by cosmology. It was found that the variation due to cosmology is not large enough to change the shape of the function, which means that the GSMF is robust under a change of cosmology, if one assumes an observationally constrained cosmological model. It was also verified that the red galaxies seem to be more affected by the change of cosmology than the blue galaxies.

The second part of this thesis introduces the GCMF, a new function based on the redshift evolution of the average galactic mass. This mass can be derived using two methods, or combining luminosity function and mass-to-light ratio data, or alternatively estimated by GSMF data, which can potentially create a bias on the results. In order to verify this bias, it was used a sample of 5558 objects from FORS Deep Field galaxy survey in the redshift range $0.5 < z < 5$. The results showed that the approach which uses GSMF data is less biased than the other. Then, the GCMF can be calculated and adjusted by a simple Schechter function with very different fitted parameters from the ones found in the literature for the GSMF. At last, to check how dependent the GCMF is to the choice of the survey and the cosmology, the UltraVISTA GSMF obtained in the first part was used. The distinct results from FORS Deep Field and UltraVISTA data leads to a conclusion that the choice of survey is essential to the GCMF analysis. The GCMF behavior follows the theoretical predictions from the cold dark matter models in which the less massive objects form first, followed later by more massive ones, the "bottom-up" theory. This general trend is seen in the GCMF for different cosmological models, with only a significant difference on the best-fit parameters related to the low mass regime.

Keywords: galaxies: mass function - cosmology: theory - galaxies: formation

Rio de Janeiro
May 2016

Resumo

EVOLUÇÃO DE MASSA GALÁCTICA SOB UMA PERSPECTIVA COSMOLÓGICA

Amanda Reis Lopes
Orientadores: Marcelo Byrro Ribeiro e Carlotta Gruppioni

Resumo da Tese de Doutorado submetida ao Programa de Pós-graduação em Astronomia, Observatório do Valongo, da Universidade Federal do Rio de Janeiro - UFRJ, como parte dos requisitos necessários à obtenção do título de Doutor em Ciências - Astronomia.

O objetivo desse trabalho é analisar a evolução da massa das galáxias a partir de uma perspectiva cosmológica. Essa tese está organizada em duas partes: a primeira descreve os efeitos de diferentes cosmologias na função de massa estelar (GSMF) e a segunda discute uma ferramenta alternativa para analisar a evolução da massa galáctica baseada em um método semi-empírico relativístico que usa dados observacionais derivados de levantamentos de galáxias, a função de massa cosmológica (GCMF).

No primeiro tópico, a GSMF é computada para uma amostra de ~ 220000 galáxias selecionadas na banda K_S do levantamento UltraVISTA até $z \sim 4$, assumindo os modelos padrão e Lemaître-Tolman-Bondi (LTB) li-mitados pelas observações. Então, foram desenvolvidas três análises separadas considerando a amostra completa, ou com apenas galáxias vermelhas ou azuis, para verificar uma possível mudança no cenário evolutivo das galáxias causada pela cosmologia. Verificou-se que a variação devido à cosmologia não é grande o suficiente para mudar o perfil da função, o que significa que a GSMF é robusta sob uma mudança de modelo cosmológico se este for obtido usando diversas observações cosmológicas. Também verificou-se que as galáxias vermelhas parecem ser mais afetadas pela mudança de cosmologia do que as azuis.

A segunda parte desta tese introduz a GCMF, uma nova função baseada na evolução da massa galáctica média. Esta massa pode ser derivada usando dois métodos, ou combinando dados da função de luminosidade e de razão massa-luminosidade, ou, alternativamente, através dos dados da GSMF, o que pode criar um viés nos resultados. Para estudar tal viés, usou-se uma amostra de 5558 objetos do levantamento FORS Deep Field na faixa de $0.5 < z < 5$. Os resultados revelaram que a abordagem que usa a GSMF é mais confiável. A GCMF pôde então ser calculada e ajustada por uma função de Schechter simples com os parâmetros ajustados exibindo valores bem diferentes dos encontrados na literatura para a GSMF. Por fim, para verificar o quão dependente a GCMF é da escolha do catálogo de galáxias, foi usada a GSMF do catálogo photométrico UltraVISTA derivada na primeira parte desta tese. Os diferentes resultados provenientes dos dados do FORS Deep Field e do UltraVISTA conduzem a conclusão de que a escolha da amostra observacional é essencial para a análise da GCMF. O comportamento da GCMF segue as predições teóricas dos modelos de matéria escura fria, no qual objetos menos massivos formam primeiro do que os mais massivos, ou seja, de acordo com a teoria "bottom-up". Essa tendência geral é observada na GSMF para diferentes modelos cosmológicos, com apenas o parâmetro da função de Schechter relativo ao regime de baixa massa apresentando uma diferença significativa.

Palavras-chaves: galáxias: função de massa - cosmologia: teoria - galáxias: formação

Rio de Janeiro
Maio de 2016

Contents

Glossary

ΛCDM cosmological model based on a FLRW metric, also known as standard model. 1

BB Big Bang. 26

CDM Cold Dark Matter. 25

CGBH described by García-Bellido & Haugbølle (2008), is a cosmological model based on a LTB metric for a flat Universe. 19

FDF FORS Deep Field. 7

GCMF Galaxy cosmological mass function. 5

GSMF Galaxy stellar mass function. 2

IMF Initial mass function. 2

LF Galaxy luminosity function. 3

LTB Lemaître-Tolman-Bondi. 3

NIR Near-infrared. 4

NUV Near-ultraviolet. 4

OCGBH described by García-Bellido & Haugbølle (2008), is a cosmological model based on a LTB metric for an open Universe. 20

SED Spectral energy distribution. 2

SFH Star formation history. 40

SNIa Type Ia supernovae. 1

SPS Stellar population synthesis. 41

UVISTA UltraVISTA. 4

List of Figures

List of Tables

Introduction

Cosmology is the area of physics that studies the origin and evolution of the entire content of the Universe, and its underlying physical processes. Thus, a theoretical picture of the overall structure and evolution of the Universe is known as a cosmological model, which is based on a set of assumptions, including a gravitational theory, and, usually, has its predictions compared with the observational data. Currently, the most widely used and adopted as a standard model is the Big Bang cosmology which assumes the general relativity theory and fits very well the results from independent observables, such as the luminosity distance-redshift relation stemming from type Ia supernovae (SNIa) surveys (e.g., Riess *et al.* 1998; Perlmutter *et al.* 1999), the power spectrum of the cosmic microwave background radiation (e.g., Komatsu *et al.* 2011), and the angular size scale obtained from baryonic acoustic oscillation studies (e.g., Percival *et al.* 2010), under the so-called cold dark matter with a non-vanishing cosmological constant parametrization (ΛCDM; e.g., Komatsu *et al.* 2009). Note that the ΛCDM model assumes two additional components, a non-baryonic one, named dark matter, which is considered a good explanation for the discrepancies observed between the dynamics and the visible mass in galaxies and galaxy clusters, and a exotic one, known as dark energy, which would explain the acceleration of the Universe's expansion rate. Nevertheless, other cosmological models can also be found in the literature, whether with alternative spacetime geometry descriptions or with different matter and energy contents for the Universe.

Based on the standard cosmology, the main theory of galaxy formation and evolution, the hierarchical merging, states that structure grows hierarchically, with small objects collapsing first and merging continuously to form larger and more massive ones (e.g., Cole *et al.* 2000; De Lucia *et al.* 2006). However, observational evidence for large and red galaxies already in place at very high redshifts contradicts this paradigm and reinforces an alternative theory called monolithic collapse (e.g., Eggen, Lynden-Bell & Sandage 1962), which the gas cloud collapsed to form a galaxy and its spin is what determines what type of galaxy will be created. From this theory, the galaxy properties are defined at the moment of its birth.

In order to verify how well these theoretical predictions describe observations and to obtain insights about physical processes involved in the formation and evolution of galaxies one uses the galaxy redshift surveys. A basic measure derived from these surveys is the stellar mass, i.e., mass contained in form of stars, and its respective cosmic time evolution. This information is captured by the widely used *galaxy stellar mass function* (GSMF), in whose calculation it is necessary first to estimate the stellar mass from a galaxy sample. This is done using a broadband spectral energy distribution (SED) fitting, which uses multi-wavelength photometric observational data to calculate the galaxy physical properties through the application of a series of models and assumptions. This technique relies on the choice of a number of astrophysical parameters, such as the stellar population synthesis models (e.g., Bruzual & Charlot 2003; Maraston 2005), a grid of metallicity, an extinction law, an initial mass function (IMF), and a cosmological model. The SED fitting programs (e.g., `MAGPHYS`, `HyperZ`) are written assuming a ΛCDM model. It follows that the whole analysis based on this procedure is cosmological dependent. But how exactly does this dependency work? And how strong is it? These are some of the questions we will discuss in this thesis.

The GSMF describes the number density of galaxies per logarithmic stellar mass interval. Several works calculating and fitting the GSMF by a simple or double Schechter function in different redshift ranges down to low mass limits ($\mathcal{M} \sim 10^8\ \mathcal{M}_\odot$) can be found in the literature, e.g., Pérez-González *et al.* (2008); Baldry *et al.* (2008, 2012); Drory *et al.* (2009); Kajikawa *et al.* (2009); McLure *et al.* (2009); Ilbert *et al.* (2010); Bolzonella *et al.* (2010); Pozzetti *et al.* (2010); Domínguez-Sánchez *et al.* (2011); Caputi *et al.* (2011); Mortlock *et al.* (2011); Santini *et al.* (2012). However, all these analyses present a cosmological model dependency related to both the stellar mass and the comoving volume. Although, one might argue that the current precision for the constraints on the cosmological model are good enough to render a similar GSMF in all cosmologies fitted by the observations, this assertion, nevertheless, was never tested, and the question remains of how robust is the GSMF under a change of cosmology.

Conroy *et al.* (2009) studied the uncertainties in the stellar masses derived using the SED fitting technique, and found a factor of about 0.3 dex if the uncertainties related to all astrophysical assumptions were taken into account. Other papers emphasized the importance of an specific assumption in the stellar mass results, e.g., star formation history (Maraston *et al.* 2010; Pforr *et al.* 2012), and the stellar population synthesis model (Kannappan & Gawiser 2007; Wuyts *et al.* 2007; Cimatti *et al.* 2008; Longhetti & Saracco 2009; Muzzin *et al.* 2009). Moreover, Marchesini *et al.* (2009) made an comprehensive study of the systematic and random uncertainties of the GSMF analysis. These authors used different sets of IMF, metallicity, stellar population synthesis models and extinction curve in the SED modelling to quantify the systematic errors. It was found that the evidence for mass-dependent evolution, with the low-mass end evolving more rapidly than the high-mass end, is no longer robust when the systematic uncertainties from the set of SED-modelling assumptions are taken into account. The present work follows a similar approach but it aims to understand how the assumed cosmological model affects the GSMF. Therefore all other parameters are unchanged.

In order to answer the previous questions, we need at least two different cosmological models parametrized to reproduce observational constrains, such as the SNIa and the baryonic acoustic oscillation data. For this purpose, besides the ΛCDM model, we chose the parametrization of García-Bellido & Haugbølle (2008) for the Lemaître-Tolman-Bondi (LTB) dust model. One of the reasons to choose an inhomogeneous cosmology such as LTB lies on many recent advances on the development of this model (e.g., Hellaby & Alfedeel 2009; Alfedeel & Hellaby 2010; Meures & Bruni 2012; Humphreys *et al.* 2012; Nishikawa *et al.* 2012; Bull & Clifton 2012; Valkenburg *et al.* 2012; Wang & Zhang 2012; Hellaby 2012) and several tests and fits to different observables (e.g., February *et al.* 2010; Bolejko *et al.* 2011; Bull *et al.* 2012; de Putter *et al.* 2013; Hoyle *et al.* 2013). Great effort has been made to establish inhomogeneous models as a viable alternative or generalisation of the standard model.

From an observational perspective, recent papers sought for evidence of a large local void. Keenan *et al.* (2013) studied the K-band galaxy luminosity function (LF) from the UKIRT Infrared Deep Sky Survey (UKIDSS) and Two Micron All Sky Survey (2MASS) with spectroscopy from the Sloan Digital Sky Survey (SDSS), Two-degree-Field Galaxy Redshift Survey (2dFGRS), Six-degree-Field Galaxy Redshift Survey (6dFGRS) and Galaxy And Mass Assembly (GAMA), finding an underdense region inside a radius of about $300h^{-1}$ Mpc, at $z \leq 0.07$. Whitbourn & Shanks (2014) analyzed the galaxy density distribution of $\sim 250,000$ galaxies out to $z \sim 0.1$ based on the 2MASS K-band photometry and the combination of the 6dFRGS, GAMA, and SDSS spectroscopic data for different sky regions: the south Galactic cap, the southern part of the north Galactic cap, and the northern part of the north Galactic cap. They found a large underdense region within a radius of $150h^{-1}$ Mpc in the south Galactic cap, a less pronounced underdensity in the northern part of the north Galactic cap and no underdensity in the southern part of the north Galactic cap. If confirmed, an underdense region of $200 - 300h^{-1}$ Mpc would explain the apparent tension between the direct measurements of the Hubble constant and those inferred by Planck, because any cosmology would have to account for the local void before fitting the SNIa Hubble diagram. However, Böhringer *et al.* (2015) analysis argues differently. They studied the local density distribution in the southern sky with the ROSAT-ESO Flux-Limited X-ray galaxy cluster survey (REFLEX II) and compared results with the two previously mentioned papers. They found a local underdensity that is not isotropic and limited to a size significantly smaller than 300 Mpc radius. The authors stated that the other works that detect a local void are dominated by galaxy data preferentially from regions in the south Galactic cap near the equator and near the South Galactic Pole, which are indeed underdense while other sky regions are not underdense at low redshift. Therefore, this topic remains open to discussion.

Additionally, other papers (e.g., Moss *et al.* 2011, Zibin & Moss 2011) used different types of data to constrain models with LTB metric and dark energy, named ΛLTB cosmology, but these models were ruled out.

Following the choice of the cosmological models, we proceed to perform our analysis of the GSMF in different cosmologies by selecting the galaxy sample described in Ilbert *et al.* (2013), which was based on the data taken by the VIRCAM (Emerson & Sutherland 2010) on the VISTA telescope as a project named UltraVISTA (hereafter, UVISTA). This sample was selected in the K_S-band from UVISTA data (McCracken *et al.* 2012) with photometric redshifts calculated using a 29-band multi-wavelength catalogue that includes the four near-infrared (NIR) filters from UVISTA, the broad and intermediate/narrow bands from COSMOS (Capak *et al.* 2007), the Infrared Array Camera (IRAC)-bands from *Spitzer* (Ilbert *et al.* 2010) and the near-ultraviolet (NUV) band from GALEX (Zamojski *et al.* 2007). Ilbert *et al.* (2013) estimated the GSMF up to

$z = 4$ for a full, star-forming and quiescent samples in the standard cosmology, therefore we followed a similar approach to compute the stellar mass and GSMF in the void models described by Zumalacárregui *et al.* (2012). In order to guarantee a result with no systematics, we also recalculate the GSMF in the ΛCDM model. And, finally, we compared the redshift evolution of the GSMF in the standard and alternative models.

It must be stressed that the approach described here is very general, from the estimation of the stellar mass to the GSMF calculation, and it can also be applied to any type of cosmology, like models based on the modified gravity (e.g., Tsujikawa 2010) or the Szekeres solution (e.g., Peel, Ishak & Troxel 2012).

It is also important to emphasize that the present work does not aim at cosmological model selection. Although it uses alternative cosmologies and compares results with those derived with the standard model, our goal is to ascertain how robust the stellar mass analysis is under a change of cosmology constrained by observations. Moreover, this work focuses on the possible dependency between galaxy evolution and cosmology.

Other papers have similarities with the present work due to the study of the effects of the cosmology in the observational analysis. Iribarrem *et al.* (2013) computed the far-infrared LF for the *Hershel*/PACS evolutionary probe survey assuming both the standard and LTB-void models. These authors concluded that the LF slopes at the faint-end depend on the cosmology, and therefore, either the standard model is over-estimating the number density of faint sources or the void models are under-estimating them. Marulli *et al.* (2012) described the effects of the cosmology dependency of the distance-redshift relation on the clustering of galaxies. Aside from the different goals and the different quantities under analysis, this work performs for the first time a SED-fitting adopting an alternative cosmological model. Moreover, this is the first time a galaxy evolution scenario is presented for a LTB model. The analysis and results from this topic are summarised in Lopes *et al.* (2016a).

Another interesting point is that the GSMF is estimated applying an statistical method to a galaxy stellar mass sample, therefore the GSMF is observationally driven, and the cosmological theory is only implicit. Here we propose a different approach to study the galactic mass, starting from a relativistic cosmology framework, then relating the theoretical to observational quantities, and finally defining a new tool to study the mass evolution of galaxies, the *galaxy cosmological mass function* (GCMF), symbolized as ζ.

Similar to the GSMF, ζ is a quantity defined in the framework of relativistic cosmology that measures the distribution of galactic masses in a given volume within a certain redshift range of an evolving universe defined by a spacetime geometry. It is important to emphasize that the GCMF evaluates the average mass evolution and not the stellar mass, this is because from a theoretical perspective all quantities such as luminosity and mass are considered to be general, i.e., the luminosity is bolometric and the masses are averaged assuming all its content, stellar, gas, dust and dark matter. To reconcile the theory with the observations, appropriate adaptations are needed. And, this generic definition can be turned into an operational one by following the approach advanced by Ribeiro & Stoeger (2003), which connects the mass-energy density given by the right-hand side of Einstein field equations, and the associated theoretically derived galaxy number counts, with the astronomically determined LF and mass-to-light ratio. In this way, the GCMF contains information about the number density evolution of all galaxies at a certain z, as well as their average mass $\mathcal{M}_g(z)$ in that redshift. Therefore, $\zeta \mathrm{d}\mathcal{M}_g$ provides the number density of galaxies with mass in the range $\mathcal{M}_g$, $\mathcal{M}_g + \mathrm{d}\mathcal{M}_g$. Since $\mathcal{M}_g(z)$ is the average mass at a specific redshift value, the quantity $\zeta \mathrm{d}\mathcal{M}_g$ is given in the redshift range z, $z + \mathrm{d}z$.

Although the GSMF is a well-established tool to study galaxy evolution, our goal here is to develop a methodology capable of estimating the GCMF using observational data, since the GCMF itself is a derived quantity and is, therefore, directly linked to the underlying cosmological theory. The study of this function could provide some insights about how, or even *if*, effects of relativistic nature can affect the mass evolution analysis.

The GCMF can be seen as an application of the general model connecting cosmology theory to the astronomical data, introduced by Ribeiro & Stoeger (2003), and further developed by Albani*et al.* (2007) and Iribarrem *et al.* (2012). These authors aimed at providing a relativistic connection for the observed number counts data produced by observers and studying its relativistic dynamics. In this thesis we extend both goals to the mass function of galaxies. This theoretical connection allows us to study these quantities in other spacetime geometries than the Friedmann-Lemaître-Robertson-Walker, metric of the Universe in the ΛCDM model, and then trying to ascertain to what extent the underlying choice of spacetime geometry affects these quantities, that is, to what extent galaxy evolution might be affected by the spacetime geometry. Here we analyzed the mass function for the average galactic mass at some redshift interval and provided an illustration of our methodology by means of deep galaxy redshift survey data. We used available observations of the galaxy LF, luminosity density, and stellar masses to estimate the redshift evolution of the average galactic mass and luminosity. These two pieces of information are crucial to our analysis because they cannot be obtained through cosmological principles, but have direct implications for a range of theoretical considerations and the determination of an important quantity, the differential number counts of galaxies. With the redshift evolution of $\mathcal{M}_g$ and the equations presented in Ribeiro & Stoeger (2003) we can obtain the GCMF.

For a first discussion, we used the LF parameters of the FORS Deep Field (FDF) galaxy survey presented by Gabasch *et al.* (2004) in the B-band and redshift range $0.5 < z < 5.0$ to calculate the selection function ψ and the luminosity density j, to then obtain the average luminosity evolution, L_B. Next we computed the galaxy stellar mass-to-light ratio using the galaxy stellar masses presented by Drory *et al.* (2005). These two results lead to a redshift evolution of the average galactic mass. Alternatively, we estimated $\mathcal{M}_g(z)$ using the ratio between the stellar mass density and number density, both quantities derived from the GSMF presented by Drory & Alvarez (2008) for the same FDF sample of galaxies. A comparison between these two methodologies to calculate $\mathcal{M}_g$ enables us to discuss the intrinsic biases introduced by ψ, j and the mass-to-light ratio in the calculation of the average galactic mass. We found that the first methodology is less reliable because of its strong dependence on the selection function and luminosity density with the limit of the survey, in addition to uncertainties related to the average mass-to-light ratio. As conclusion, we chose the second method to obtain the $\mathcal{M}_g(z)$. The next step was to calculate $\mathrm{d}\mathcal{M}_g/\mathrm{d}z$, the theoretical quantities of interest, such as the differential number counts $\mathrm{d}N/\mathrm{d}z$, and its observational counterparts, $[\mathrm{d}N/\mathrm{d}z]_{obs}$, derived from the association between theory and the selection function. Finally, the GCMF was computed assuming a comoving volume, which allowed us to compare its results with predictions from galaxy evolution models found in the literature.

Although the GSMF and GCMF present similar behaviors and can be described by a Schechter analytical form, both functions are not directly comparable, due to their definition. An example of this affirmation can be seen in the Schechter parameter ϕ^*, which are always positive for the GSMF but it can assume negative values for the GCMF. The negative values are a reflection of the $\mathrm{d}\mathcal{M}_g/\mathrm{d}z$ used in the definition of ζ.

In order to extend the analysis, we used the GSMF results from UVISTA in the ΛCDM and LTB models to estimate the GCMF. These data allowed us to obtain a deeper understanding of the implications regarding the different morphological types to the GCMF. Moreover, we verified the effect of different cosmologies to this function. The discussion and results of the GCMF based on FDF and UVISTA are presented in Lopes *et al.* (2014, 2016b).

This thesis is organized as follows. Chapter 1 summarises the relevant theoretical concepts and equations from the standard and void-LTB cosmologies. In Chapter 2 we give a brief description of the galaxy formation and evolution theory. Chapter 3 describes the SED fitting procedure and its assumptions to estimate the stellar masses of galaxies. A detailed description of the UVISTA catalogue and its subsamples, the results for the stellar masses and the GSMF for the full, blue and red galaxy samples in all cosmologies are presented in Chapter 4. In Chapter 5 we discuss the semi-empirical relativistic approach to obtain a GCMF, along with the results based on the GSMF from UVISTA and FDF. Finally, the thesis ends with a summary of our conclusions.

Chapter 1

Cosmological background

> "The Universe is not only queerer then we suppose, it is queerer than we can suppose."
>
> *J. B. S. Haldane*

Cosmological models form the background framework of all galaxy mass analysis, therefore a change in those models may affect the physical interpretation of the masses in the context of galaxy formation and evolution. In this chapter I shall describe the basic theoretical concepts of both standard and giant-void cosmological models, focusing in the differences on the evolution of various quantities, such as the luminosity distance and time regarding the different cosmologies. This information is essential and its connection to the observational quantities will be explored in Chapters 4 and 5. The relation between the cosmological models and galaxy formation theory is introduced in Chapter 2.

1.1 The Standard model

The standard cosmological model, also known as concordance cosmology and ΛCDM (cold dark matter) model, is based on the assumptions of homogeneity and isotropy at sufficiently large scales. This premise allows the evolution of the Universe to be described in terms of a few cosmological parameters that can be measured from astronomical observations.

Moreover, observational analysis first from Lemaître, then from Edwin Hubble found that most galaxies were moving away from us with a recessional velocity proportional v to their separation distance D (Hubble 1929),

$$v = H_0 D, \tag{1.1}$$

where the constant of proportionality is H_0 known as the Hubble constant. This relation called *Hubble Law* implies that earlier on these sources were closer to us, and assuming the isotropy and homogeneity, they were also closer to any other point in the Universe. Thus, the distance between any two points is growing, in other words, the space itself is expanding. This process led to the conclusion that at some point in the past all the matter and energy in the Universe must have been in a very concentrated state, resulting in the formulation of the *Big Bang Theory*.

Another key aspect of the standard cosmology scenario is the mass distribution in the Universe, in which an essential "invisible" component is the *dark matter*. One of the first evidences of dark matter was claimed by Zwicky (1933), which studied the velocities in the Coma cluster and found that the total mass necessary to sustain the system in equilibrium had to be much more than the observed visible matter. Later studies confirmed this result, including theoretical and observational advances (e.g., Kent 1986; Persic *et al.* 1996; Clowe *et al.* 2006). In theory, three types of dark matter can be postulated, a 'cold dark matter' (CDM) composed by particles with non-relativistic speed, $v/c < 0.1$, a 'hot dark matter' composed by ultra-relativistic, $v/c > 0.95$, and a 'warm dark matter' composed by relativistic particles, $0.1 < v/c < 0.95$. However, the CDM is the only component good enough to properly explain observed features, such as the galactic rotational curves, velocity dispersions and weak lensing properties.

Later on, the dimming in the redshift-distance relation of SNIa yield an unexpected result (e.g., Riess *et al.* 1998; Perlmutter *et al.* 1999), the SNIa moving away with growing recessional velocity, which, in a spatially homogeneous universe implies in a accelerated Universe's expansion rate. However, as this contradicts the theory in which the gravity is an ever-attractive force, an extra component that acts as a repulsive gravitational source had to be introduced. This exotic component that causes the acceleration, namely *dark energy*, can be understood in terms of a cosmological constant or a fluid with negative pressure. In the first approach, effectively the cosmological constant acts as a energy density independent of the expansion of the Universe ρ_Λ, and therefore interpreted as the energy density of the vacuum. However the energy density of the vacuum predicted by the quantum field theory $\rho_{vac} \sim 10^{95}$ kg m^{-3} are 121 orders of magnitude larger than the measurements of $\rho_\Lambda \sim 10^{-26}$ kg m^{-3}. For the second approach there must be some exotic component with negative pressure driving the accelerated expansion of the Universe, and following this concept there have been proposed many different alternative models of dark energy, e.g., quintessence, generalized Chaplygin gas (for details on dark energy models see Copeland, Sami & Tsujikawa 2006; Amendola & Tsujikawa 2010; Tsujikawa 2010). Hence, we still do not understand the dark energy is physical nature and currently much effort has been applied in this subject.

In the ΛCDM parametrization of the standard model, the Universe is assumed to be flat with 3 main components, $\sim 70\%$ is made of dark energy, $\sim 25\%$ is due to CDM and the remaining $\sim 5\%$ is related to the baryonic matter. This parametrization successfully predicts the aforementioned expansion of the Universe, the relative abundances of light elements, the existence of the Cosmic Microwave Background, its spectrum of anisotropies (both in temperature and polarization) and the distribution of matter on large scales, the large scale structure of the Universe.

Together with the unknown nature of the DE, there are other open issues associated to the standard model. An example is the so-called coincidence problem, in which the time of the equality between matter and Λ, $z_{eq} \simeq 0.3$, and the moment at which the expansion begins to accelerate $z_{acc} \simeq 0.7$ are remarkably close to the present time $z = 0$, but there is no reason why this should be so.

1.1.1 FLRW metric

Assuming spatial homogeneity and isotropy, we can write the Friedmann-Lemaître-Robertson-Walker line element as,

$$\mathrm{d}s^2 = -c^2\mathrm{d}t^2 + S^2\left[\frac{\mathrm{d}r^2}{1-kr^2} + r^2(\mathrm{d}\theta^2 + \sin^2\theta\mathrm{d}\phi^2)\right], \tag{1.2}$$

where t is the time coordinate, r, θ, ϕ are the spatial coordinates, $S = S(t)$ is the cosmic scale factor, k is the curvature parameter ($k = +1, 0, -1$), and c is the light speed. The combination of Eq. (1.2) with the perfect fluid energy-momentum tensor renders a solution to the Einstein's field equations with the cosmological constant Λ, known as the Friedmann equation (e.g., Roos 1994),

$$H(t)^2 = \left(\frac{\dot{S}}{S}\right)^2 = \frac{8\pi G\rho_m}{3} + \frac{\Lambda}{3} + \frac{kc^2}{S^2}, \quad (1.3)$$

where G is the gravitational constant, ρ_m is the matter density and the Hubble parameter is defined as

$$H(t) \equiv \frac{1}{S(t)}\frac{\mathrm{d}S(t)}{\mathrm{d}t}, \quad \Longrightarrow \quad H_0 = \frac{1}{S_0}\frac{\mathrm{d}S}{\mathrm{d}t}\bigg|_{t=t_0}, \quad (1.4)$$

in which S_0 is the scale factor at the present time and H_0 is the Hubble constant. Throughout this text, the index "0" is used to indicate quantities at the present time, an example being Hubble constant H_0, which is the Hubble parameter at the present time. Let me define other densities, such as the vacuum energy density in terms of the cosmological constant,

$$\rho_\Lambda \equiv \frac{\Lambda}{8\pi G}, \quad (1.5)$$

and the critical density at the present time, given by,

$$\rho_{0,c} \equiv \frac{3H_0^2}{8\pi G}, \quad (1.6)$$

which is Eq. (1.3) assuming a flat Universe with no cosmological constant, $k = \Lambda = 0$. Also, we establish that the following relative-to-critical density parameter relations holds,

$$\Omega_0 \equiv \Omega_{m_0} + \Omega_{\Lambda_0} = \frac{\rho_0}{\rho_{0,c}} = \frac{\rho_{m_0}}{\rho_{0,c}} + \frac{\rho_{\Lambda_0}}{\rho_{0,c}}. \quad (1.7)$$

Notice that since Λ is a constant, then $\rho_\Lambda = \rho_{\Lambda_0}$. From the definitions (1.7) we can rewrite Eq. (1.3) as follows,

$$kc^2 = H_0^2 S_0^2(\Omega_0 - 1). \quad (1.8)$$

Furthermore, in the matter dominated era, the law of conservation of energy applied to the zero pressure holds that,

$$\rho_m \propto S^{-3}, \quad \Longrightarrow \quad \rho_{m_0} \propto S_0^{-3}, \quad (1.9)$$

which leads to,

$$\frac{\rho_m}{\rho_{m_0}} = \frac{S_0^3}{S^3}, \quad \Longrightarrow \quad \Omega_m = \Omega_{m_0}\frac{S_0^3 H_0^2}{S_3 H_2}. \quad (1.10)$$

Rewriting the matter-density parameter in terms of the critical density we have that,

$$\Omega_m = \frac{\rho_m}{\rho_c} = \frac{8\pi G}{3H^2}\rho_m. \tag{1.11}$$

Applying the results of Eqs. (1.4)-(1.11) in Eq. (1.3), we obtain a differential equation in terms of the scale factor $S(t)$,

$$\frac{\mathrm{d}S}{\mathrm{d}t} = H_0 \left[\frac{\Omega_{m_0} S_0^3}{S} + \Omega_{\Lambda_0} S^2 - (\Omega_0 - 1) S_0^2\right]^{1/2}. \tag{1.12}$$

Following Iribarrem *et al.* (2012), the previous equation can be solved by taking the radial coordinate r as the independent variable in order to numerically calculate the function $S(r)$ along the past light cone, yielding,

$$\frac{\mathrm{d}S}{\mathrm{d}r} = \frac{\mathrm{d}S}{\mathrm{d}t}\frac{\mathrm{d}t}{\mathrm{d}r}. \tag{1.13}$$

Now considering the past radial null geodesic ($\mathrm{d}s^2 = 0$) in the geometry given by the metric (1.2),

$$\frac{\mathrm{d}t}{\mathrm{d}r} = -\left(\frac{S}{c\sqrt{1-kr^2}}\right), \tag{1.14}$$

and using Eq. (1.8), it becomes,

$$\frac{\mathrm{d}t}{\mathrm{d}r} = -\left[\frac{S^2}{c^2 - H_0^2 S_0^2(\Omega_0 - 1)r^2}\right]^{1/2}. \tag{1.15}$$

From Eqs. (1.13) and (1.15), we are able to write a first order ordinary differential equation for the scale factor in terms of the radial coordinate r,

$$\frac{\mathrm{d}S}{\mathrm{d}r} = -H_0 \left[\frac{(\Omega_{\Lambda_0})S^4 - S_0^2(\Omega_0 - 1)S^2 + (\Omega_{m_0} S^3)S}{c^2 - H_0^2 S_0^2(\Omega_0 - 1)r^2}\right]^{1/2}. \tag{1.16}$$

To find solutions for $S(r)$ we used the fourth-order Runge-Kutta method with the initial condition r_0 set as zero, whereas S_0 can be derived considering that as $r \to 0$ the spacetime is approximately Euclidean, that is $k \sim 0$. This leads, from Eq. (1.14), to $ct = -r$ as well as $S_0 = 1$. Furthermore, the redshift z can be written as

$$1 + z = \frac{S_0}{S}, \tag{1.17}$$

where a numerical solution of the scale factor immediately gives us a numerical result for $z[S(r)]$. Summarizing, based on Eqs. (1.15), (1.16) and (1.17) we constructed a table with r, $S(r)$, $t(r)$ and $z[S(r)]$ which allows us to obtain all others quantities of interest. Alternatively, we can rewrite the derivatives in terms of the z instead of r. From Eq. (1.17) it follows that,

$$\frac{\mathrm{d}t}{\mathrm{d}z} = -\frac{S}{1+z}\left(\frac{\mathrm{d}S}{\mathrm{d}t}\right)^{-1} = -\frac{1}{1+z}\frac{S}{\dot{S}}, \tag{1.18}$$

and combining Eqs. (1.15) and (1.18), we find

$$\frac{\mathrm{d}r}{\mathrm{d}z} = \left(\frac{\mathrm{d}t}{\mathrm{d}r}\right)^{-1}\frac{\mathrm{d}t}{\mathrm{d}z} = \frac{1}{1+z}\frac{\sqrt{c^2 - H_0^2 S_0^2(\Omega_0 - 1)r^2}}{\dot{S}}, \tag{1.19}$$

which allows us to obtain the scale factor in terms of z as,

$$\frac{\mathrm{d}S}{\mathrm{d}z} = \frac{\mathrm{d}S}{\mathrm{d}r}\frac{\mathrm{d}r}{\mathrm{d}z}, \tag{1.20}$$

by using Eqs. (1.16) and (1.19). A table with the results from Eqs. (1.18), (1.19) and (1.20) are equivalent to the one derived with Eqs. (1.15), (1.16) and (1.17).

1.1.2 Distances and volumes

The area distance d_A, also known as angular diameter distance, is defined by a relation between the intrinsically measured cross-sectional area element $\mathrm{d}\sigma$ of the source and the observed solid angle $\mathrm{d}\Omega$ (Ellis 1971, 2007; Plebánski & Krasiński 2006),

$$(d_A)^2 = \frac{\mathrm{d}\sigma}{\mathrm{d}\Omega} = \frac{S^2 r^2(\mathrm{d}\theta^2 + \sin^2\theta\mathrm{d}\phi^2)}{(\mathrm{d}\theta^2 + \sin^2\theta\mathrm{d}\phi^2)} = (Sr)^2, \tag{1.21}$$

as can be seen in Fig. 1.1.

The luminosity distance d_L is defined as a relation between the observed flux F and the intrinsic luminosity L of a source. In a flat and static universe it can be described by

$$F = \frac{L}{4\pi d_L^2}, \tag{1.22}$$

and it can be easily obtained from d_A, Eq. (1.21), by invoking the Etherington's reciprocity law (Etherington 1933; Ellis 1971, 2007),

$$d_L = (1+z)^2 d_A, \tag{1.23}$$

resulting in

$$d_L = S_0^2\left(\frac{r}{S}\right). \tag{1.24}$$

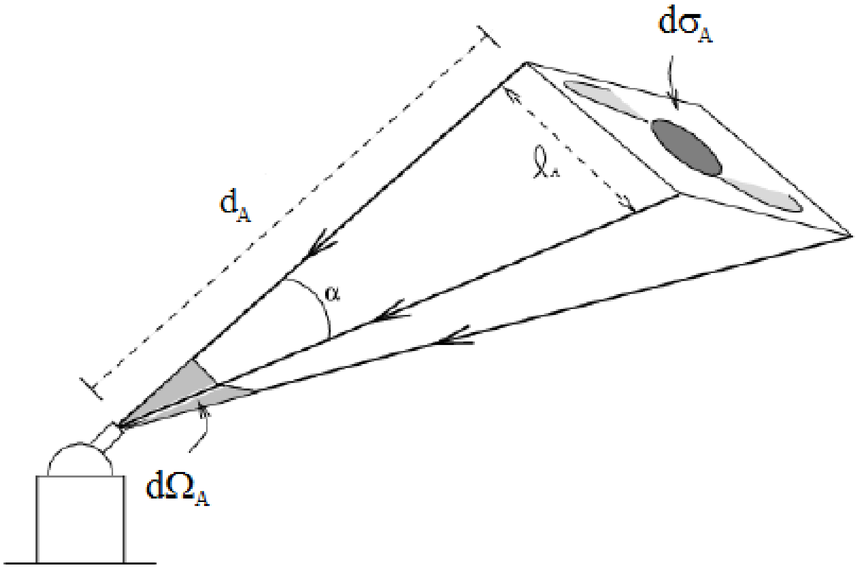

Figure 1.1: Schematic view of the angular diameter distance d_A, based on its definition. The definition of d_A in terms of the cross-sectional area element $\mathrm{d}\sigma$ of the source and the observed solid angle $\mathrm{d}\Omega$ is general, i.e., valid in all cosmologies. However, its translation in cosmological quantities, such as the scale factor, depends on the adopted metric (Ribeiro 2005).

The observations are usually obtained assuming a comoving volume V_C, however the theory often assumes a proper volume V_{Pr}. The proper distance and its respective volume are defined as

$$d_{Pr} = \frac{S}{S_0}\,r, \quad \Rightarrow \quad V_{Pr} = \frac{4}{3}\pi\left(\frac{S}{S_0}\,r\right)^3, \tag{1.25}$$

which entails that this distance changes due to the expansion of the Universe. The comoving volume depends only on the comoving distance d_C, also known as comoving coordinate r,

$$V_C = \frac{4}{3}\pi r^3. \tag{1.26}$$

Fig. 1.2 shows the redshift evolution of the cosmological distances, d_A, d_L and d_C, and the volumes, V_{Pr} and V_C. From metric (1.2) the conversion of volume units can be given by

$$dV_{Pr} = \frac{S^3}{\sqrt{1-kr^2}}r^2\mathrm{d}r\sin\theta\mathrm{d}\theta\mathrm{d}\phi = S^3\mathrm{d}V_C. \tag{1.27}$$

Hence, the relation between n_C and n, which are the number densities of cosmological sources respectively given in terms of comoving and proper volumes, can be written as,

$$n_C = S^3 n. \tag{1.28}$$

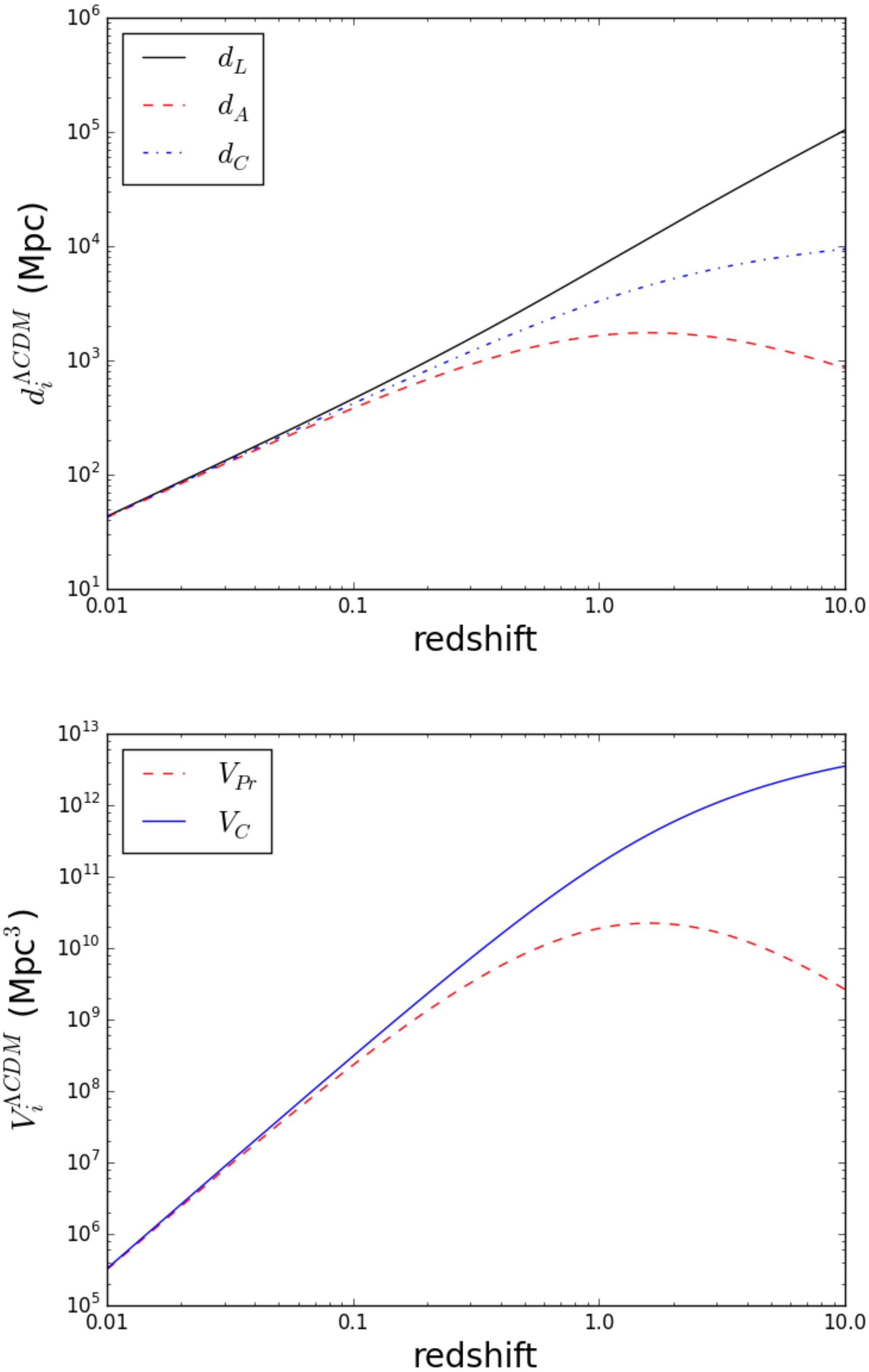

Figure 1.2: *Top panel:* Three cosmological distances in the ΛCDM model, adopting $H_0 = 70$ km s^{-1} Mpc^{-1}, $\Omega_{m_0} = 0.3$ and $\Omega_{\Lambda_0} = 0.7$. The proper distance was not plotted because in this framework $d_{Pr} \equiv d_A$. At lower redshifts, $z \sim 0$, all distances become the same, as in an Euclidean space. *Bottom panel:* Proper and comoving volumes in terms of the redshift.

1.2 LTB models

The LTB model assumes a spatially inhomogeneous and isotropic geometry, and it has three arbitrary functions - that can be reduced to two by a coordinate transformation - which can be defined in a way that they may follow some theoretical and/or observational requirements. It was first proposed by A. Georges Lemaître (1933), which used a small deviation from Einstein static solution of the field equations to investigate the formation and condensation of the galaxies. In the following year, Richard C. Tolman (1934) obtained a solution for the field equations assuming a inhomogeneous matter distribution. Later, H. Bondi (1947) rederived the Tolman's solution, studied the Doppler shift, and proved that the model could be used to obtain other specific cosmological solutions by making suitable choices of its arbitrary functions.

Since then many others have rediscovered the LTB model (see Krasiński 1997 and references therein). Nevertheless, there is a practical recurring problem in the LTB spacetime, the difficulty to solve analytically the null geodesic equations, which complicates the definition of the relevant observational quantities in this cosmology. Many approaches were developed to solve this problem, e.g., Ribeiro (1992, 1993); Stoeger *et al.* (1992); Mustapha *et al.* (1997). In this section, we focus on the parametrization advanced by Garcia-Bellido & Haugbølle (2008), which successfully parametrized the LTB model to fit simultaneously many independent observations without the cosmological constant. This model requires a pressure-less (dust) energy-momentum tensor in order to obtain an exact solution of the Einstein's field equations, and for this reason it can be called LTB dust model. At early ages, when the radiation dominated the Universe's energy budget, the pressure term was relevant, however, at these scales, the parametrization by Garcia-Bellido & Haugbølle (2008) makes the LTB solution converges to a flat, spatially homogeneous universe. This last remark is important because it makes the model reconciled with the observed degree of isotropy found in the cosmic microwave background radiation maps. Therefore the non-homogeneity is a localized property of the model. Specifically, it has an effective under-dense region of Gpc scale around the Milky Way, rendering the name 'void models' to this parametrization. This under-dense region contradicts the cosmological principle, and it implies that the Milky Way is located at a 'special' place, inside the underdensity not necessarily at the center, but close. In other words, when we exchange the standard model for the LTB model, we change the time coincidence problem for the spatial coincidence problem. An interesting consequence from the LTB geometry is that the extra dimming of distant SNIa can be explained as an extra blueshift of the incoming light caused by a non-homogeneous distribution of matter in the line of sight. Hence, the explanation of the SNIa data is a natural consequence of the spacetime itself, and this makes the LTB model a very appealing alternative to the standard model.

1.2.1 Void-LTB metric

The LTB line element, following Bonnor's (1972) notation, can be written as

$$\mathrm{d}s^2_{_{LTB}} = -c^2\mathrm{d}t^2 + \frac{A'(r,t)^2}{f^2(r)}\mathrm{d}r^2 + A(r,t)^2\mathrm{d}\Omega^2, \tag{1.29}$$

where $\mathrm{d}\Omega = \mathrm{d}\theta^2 + \sin^2\theta\mathrm{d}\phi^2$ and $f(r)$ and $A(r,t)$ are arbitrary functions. Throughout this section dotted quantities refer to time coordinate derivatives and primed ones refer to radial coordinate derivatives, therefore $A'(r,t) = \partial A/\partial r$. Note that the following choice of the arbitrary functions,

$$A(r,t) = a(t)r, \qquad f(r) = \sqrt{1-kr^2}, \tag{1.30}$$

reduces the previous expression to the FLRW line element, Eq. (1.2). Considering a pressure-less (dust) matter content with proper density $\rho_{_M}$, it can be shown that the Einstein's field equations for the line element (1.29) can be combined to yield (e.g., Ribeiro 1992),

$$8\pi G\rho_{_M} = \frac{F'(r)}{2A'A^2}, \tag{1.31}$$

where $F(r)$ is another arbitrary function, and G is the gravitational constant. Next, we will specialize the arbitrary functions above to the Garcia-Bellido & Haugbølle (2008) parametrization.

Assuming a spherically symmetric matter source, i.e., isotropy, it is straightforward to relate $f(r)$ to the spatial curvature parameter $\kappa(r)$ in Garcia-Bellido & Haugbølle (2008) by writing,

$$f(r) = \sqrt{1-\kappa(r)}. \tag{1.32}$$

Moreover, the boundary condition functions $F(r)$ and $\kappa(r)$ are defined by the nature of the inhomogeneities through the local Hubble rate, the local matter density and the local spatial curvature, resulting in

$$F(r) = H_0^2(r)\Omega_M(r)A_0^3, \tag{1.33}$$

$$\kappa(r) = -[1 - \Omega_M(r)]H_0^2(r)A_0^2, \tag{1.34}$$

with the transverse Hubble rate

$$H_T(r,t) = \frac{\dot{A}(r,t)}{A(r,t)}, \tag{1.35}$$

the longitudinal Hubble rate

$$H_L(r,t) = \frac{\dot{A}'(r,t)}{A'(r,t)}, \tag{1.36}$$

and through the choice of a synchronous comoving gauge choice, $A(r,0) = A_0(r) = r$ and $H_0 = H_T(r,0) = H_L(r,0)$, where $\Omega_M(r)$ is the dimensionless matter density parameter related to the integrated critical density in the comoving volume at radial coordinate r, given by,

$$\bar{\rho}_c = \frac{3H_0^2(r)}{8\pi G} \tag{1.37}$$

as

$$\Omega_M(r) = \frac{\rho_M(r)}{\bar{\rho}_c}. \tag{1.38}$$

Considering the time elapsed since the Big Bang as simultaneous, i.e., it is the same value for all observers, this additional assumption yields the class known as constrained García-Bellido & Haugbølle (2008), hereafter CGBH. In this class of models, the hyperbolic solution (Ω_k ¿ 0) of the present-time transverse Hubble parameter $H_0(r)$ is written as (Zumalacárregui *et al.* 2012),

$$H_0(r) = H_{in}\left[\frac{1}{\Omega_k(r)} - \frac{\Omega_M(r)}{\Omega_k(r)^{3/2}}\sinh^{-1}\sqrt{\frac{\Omega_k(r)}{\Omega_M(r)}}\right], \tag{1.39}$$

where $\Omega_k(r) = 1 - \Omega_M(r)$ is the curvature parameter inside the under-dense region and H_{in} is the transverse Hubble constant at the center of the void.

Equations (1.32), (1.34) and (1.39) can be combined to yield,

$$f(r) = \sqrt{1 + H_{in}^2\, r^2\left[\frac{1}{\sqrt{\Omega_k(r)}} - \frac{\Omega_M(r)}{\Omega_k(r)}\sinh^{-1}\sqrt{\frac{\Omega_k(r)}{\Omega_M(r)}}\right]^2}, \tag{1.40}$$

and the other arbitrary function $F(r)$ can be obtained by the combination of Eqs. (1.33) and (1.39)

$$F(r) = H_{in}\left[\frac{1}{\Omega_k(r)} - \frac{\Omega_M(r)}{\Omega_k(r)^{3/2}}\sinh^{-1}\sqrt{\frac{\Omega_k(r)}{\Omega_M(r)}}\right]\Omega_M(r)r^3, \tag{1.41}$$

where the matter density profile Ω_M in the CGBH model becomes

$$\Omega_M(r) = \Omega_{out} + (\Omega_{in} - \Omega_{out}) \left\{ \frac{1 - \tanh[(r - R)/2\Delta R]}{1 + \tanh[R/2\Delta R]} \right\}. \tag{1.42}$$

Here Ω_{in} is the underdensity value at the center of the void, Ω_{out} the asymptotic density parameter at large scales, R the size of the underdense region and ΔR the width of the transition between the central void and the exterior homogeneous region. Together with H_{in}, these are the free parameters which completely determinate the model. Fig. 1.3 shows the evolution of the matter density parameter in the standard and void cosmologies.

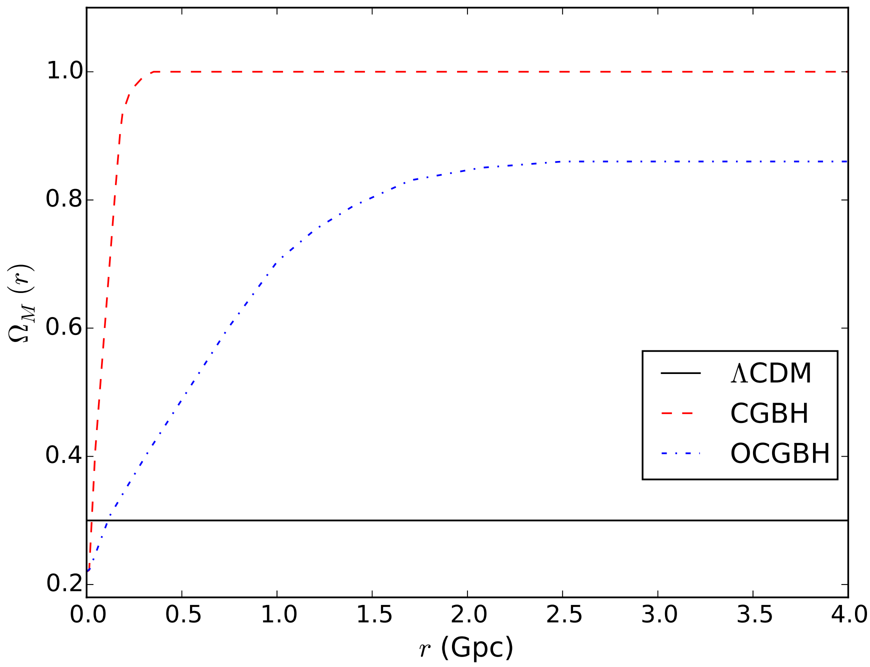

Figure 1.3: Present-time matter density parameter in the standard (ΛCDM, black solid line) and void-LTB (CGBH, OCGBH) cosmological models (red dashed and blue dash-dot lines). CGBH and OCGBH are LTB models for a flat and open universe, respectively. See Table 1.1 for values of the parameters.

1.2.2 Time, distances and volumes in the ΛCDM and the void-LTB

We follow Zumalacárregui *et al.* (2012) and besides the flat CGBH model, we also consider the case of an open universe ($\Omega_{out} \leq 1$; hereafter OCGBH), which allows a better fit to the cosmic microwave background radiation. Throughout this thesis, we use the parameters presented in Table 1.1 for the LTB and ΛCDM models.

Table 1.1: Best fit values for the void-LTB models from Zumalacárregui *et al.* (2012) and the ones assumed for the ΛCDM models.

Parameter	CGBH	OCGBH
H_{in} (km s^{-1}Mpc^{-1})	66.0 ± 1.4	71.1 ± 2.8
Ω_{in}	0.22 ± 0.4	0.22 ± 0.4
R (Gpc)	$0.18^{+0.64}_{-0.18}$	$0.20^{+0.87}_{-0.19}$
ΔR (Gpc)	$2.56^{+0.28}_{-0.24}$	$1.33^{+0.36}_{-0.32}$
Ω_{out}	1	0.86 ± 0.33
Parameter	ΛCDM	
H_0 (km s^{-1}Mpc^{-1})	70	
$\Omega_{M,0}$	0.3	
$\Omega_{\Lambda,0}$	0.7	

With the previous definitions we can calculate the angular diameter distance $A(r,t)$ in a parametric form. The result is given by,

$$A(r,t) = \frac{\Omega_M(r)}{2[1-\Omega_M(r)]^{3/2}}[\cosh\eta - 1]A_0(r), \tag{1.43}$$

where A_0 is the angular diameter distance at the present time and, for given r and t, the parameter η advances the solution as,

$$\sinh\eta - \eta = 2\frac{[1-\Omega_M]^{3/2}}{\Omega_M}H_0(r)t. \tag{1.44}$$

From the angular diameter distance $d_A = A[r(z), t(z)]$, we compute the luminosity distance d_L by means of the reciprocity theorem (Etherington 1933),

$$d_L = (1+z)^2 d_A, \tag{1.45}$$

resulting in

$$d_L^{LTB} = (1+z)^2 A[r(z), t(z)]. \tag{1.46}$$

The next step is to obtain $t(z)$ and $r(z)$ for both models. We begin with the radial null geodesic equation, $\mathrm{d}s^2 = 0$, which means making Eq. (1.29) equal to zero, yielding

$$\left.\frac{\mathrm{d}t}{\mathrm{d}r}\right|_{LTB} = -\frac{A'(r,t)}{\sqrt{1-\kappa(r)}}. \tag{1.47}$$

The relation between the time and redshift can be obtained from the redshift definition, e.g., Bondi (1947),

$$\left.\frac{\mathrm{d}t}{\mathrm{d}z}\right|_{LTB} = -\frac{1}{1+z}\frac{A'}{\dot{A}'}. \tag{1.48}$$

Combining Eq. (1.47) with Eq (1.48) we are able write the radial coordinate r in terms of the redshift z, for the LTB metric as follows,

$$\left.\frac{\mathrm{d}r}{\mathrm{d}z}\right|_{LTB} = \frac{1}{1+z}\frac{\sqrt{1-\kappa(r)}}{\dot{A}'}, \tag{1.49}$$

with $\kappa(r)$ following Eq. (1.34).

By solving Eq. (1.48), we obtain the time in the void-LTB metric and by using the results from Subsection 1.1.1, we can compare the behavior of the time in terms of the redshift in both cosmologies, as shown in Fig. 1.4. The

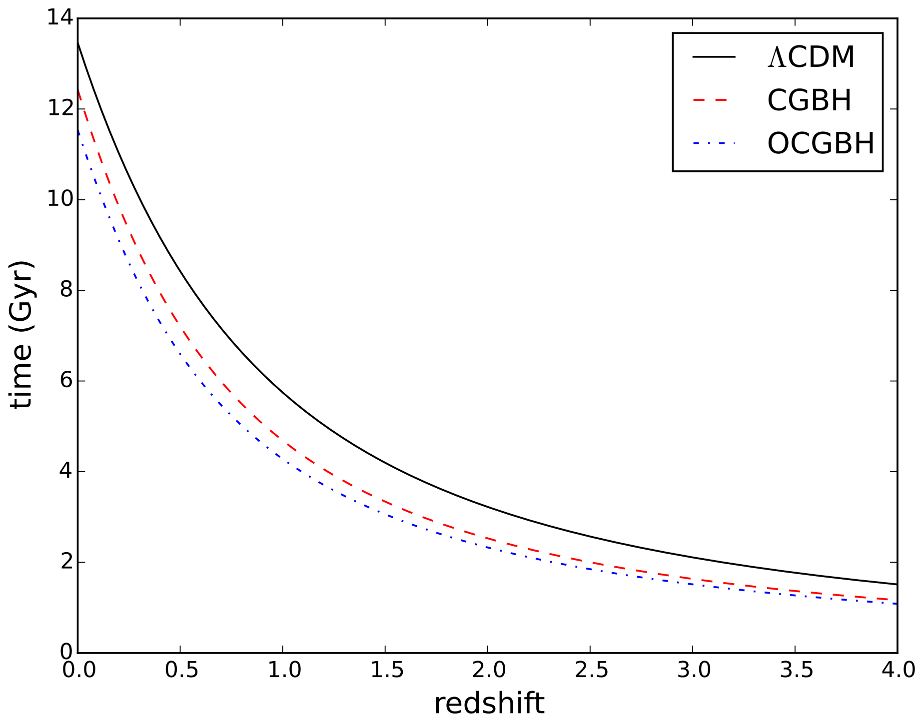

Figure 1.4: Redshift evolution of the time for the standard and void-LTB models. The age of the Universe evolves similarly in all cosmologies, however the ages in LTB are systematically smaller than the ones in ΛCDM.

time, also known as age of the Universe and cosmological time, in both LTB parametrizations and up to $z = 4$, is always smaller than the one in ΛCDM. At $z = 0$, the time for the CGBH is $\sim 7.7\%$ smaller than in ΛCDM, while in OCGBH is $\sim 14\%$ smaller. This difference increases quickly with redshift up to $z \approx 1.5$, in which the reduction in time for CGBH is $\sim 20\%$ and for OCGBH is $\sim 27\%$. For $z > 1.5$, these discrepancies show a small increase in the variation, such that at $z = 4$, they are $\sim 23\%$ for CGBH and $\sim 28\%$ for OCGBH. Moreover, the solution for Eq. (1.49) advances the luminosity distance redshift evolution for the LTB spacetime expressed in Eq. (1.46), and together with the d_L derived in subsection 1.1.1 for the standard model, we compare these quantities in Fig. 1.5. The luminosity distance was plotted as 2 times the logarithm of the ratio between its values in the different cosmologies because of the stellar mass results presented in Chapter 4, which are obtained by comparison between observational and theoretical fluxes, are related to the d_L as described in Eq. (1.22). Hence, the comparison between fluxes in different cosmologies are given by

$$\frac{F_{LTB}}{F_{\Lambda CDM}} = \left[\frac{L}{4\pi(d_L^{LTB})^2}\right]\left[\frac{L}{4\pi(d_L^{\Lambda CDM})^2}\right]^{-1} \tag{1.50}$$

$$\frac{F_{LTB}}{F_{\Lambda CDM}} = \left(\frac{d_L^{\Lambda CDM}}{d_L^{LTB}}\right)^2, \tag{1.51}$$

resulting in

$$\log\left(\frac{F_{LTB}}{F_{\Lambda CDM}}\right) = 2\log\left(\frac{d_L^{\Lambda CDM}}{d_L^{LTB}}\right). \tag{1.52}$$

It is interesting to note that the same metric, LTB, with different parameters, CGBH and OCGBH, renders a different luminosity distance evolution. This difference is such that in CGBH for $z < 1$, this quantity exhibits values larger than the ΛCDM, while in OCGBH, the luminosity distance is always lower than in ΛCDM. Another feature that can be seen in Fig. 1.5 is the rate at which the distinction between the values of d_L in the standard and the void models evolves with redshift. Up to $z = 2$ this rate is proeminent, in both CGBH and OCGBH models, but after this the difference becomes very stable, almost constant. In numbers, the discrepancies of d_L with respect to the standard model, for OCGBH range from 0.45% at $z = 0.2$ to 14.60% at $z = 4.0$, while for CGBH vary from −5.51% at $z = 0.2$ to 7.96% at $z = 4.0$.

The comoving volume element $\mathrm{d}V_C$ is given by,

$$\frac{\mathrm{d}V_c}{\mathrm{d}z} = r(z)^2\frac{dr}{dz}. \tag{1.53}$$

It can be computed by solving Eqs. (1.19) and (1.49) for the ΛCDM and void-LTB models, respectively. Its redshift evolution is shown in Fig. 1.6. In the range $0.2 < z < 4$, the difference in these volumes regarding the ΛCDM model vary from 1.36% to 38.94% and −13.45% to 24.83% for OCGBH and CGBH, respectively.

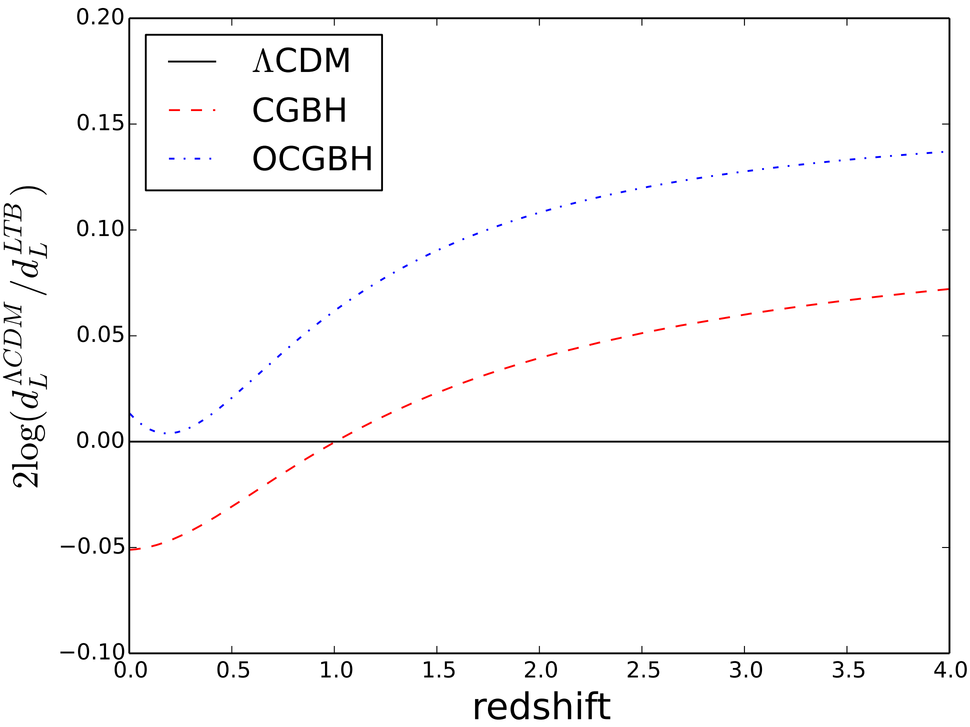

Figure 1.5: Ratio between the luminosity distance in the standard (ΛCDM) and the LTB-void models as function of redshift. By definition, if this ratio is positive it means that $d_L^{\Lambda CDM} > d_L^{LTB}$, while a negative ratio is $d_L^{\Lambda CDM} < d_L^{LTB}$. The LTB index stands for either CGBH or OCGBH and the black solid line is to assist the comparison with latter results.

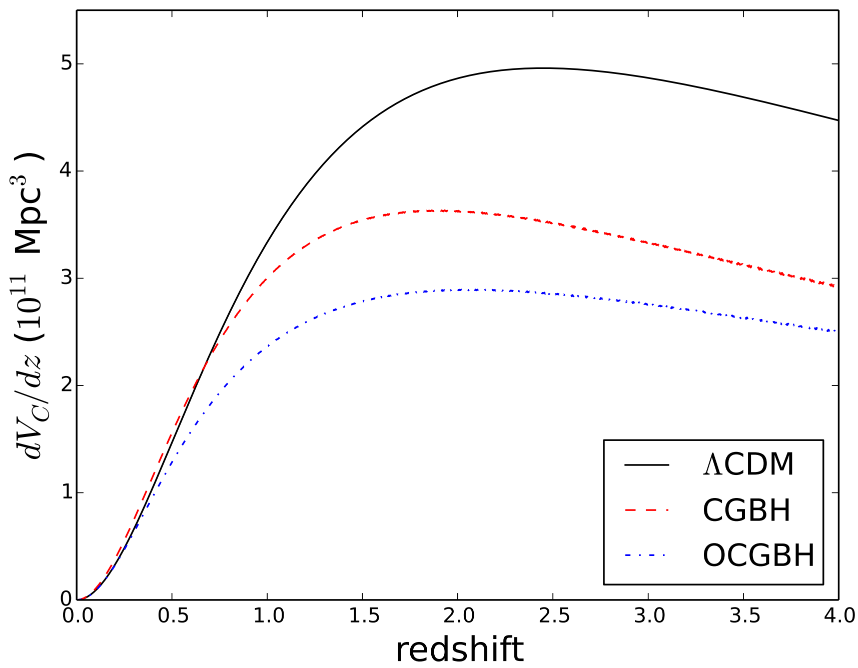

Figure 1.6: Comoving volume element for the standard (ΛCDM) and void models. This quantity evolves in a similar way in all models up to $z \approx 0.6$, then the ones based on the void models become lower than in ΛCDM.

Chapter 2

Galaxy formation and evolution

"The Universe is full of magical things, patiently waiting for out wits to grow sharper."
Eden Phillpotts

A great effort has been made to advance the knowledge of how various structures, such as galaxies and galaxy clusters, form within the framework of the Big Bang cosmology. The current theory of structure formation, called the Cold Dark Matter (CDM) scenario, follows the theoretical concepts presented in Chapter 1 together with different cosmological observations and computer simulations. This chapter presents a qualitative description of the history of the Universe according to ΛCDM model. Followed by a discussion of the two main theories of galaxy formation: monolithic collapse and hierarchical merging.

It is import to note that the structure formation theory based on the standard cosmological model is the only one presented here, because there is not a similar theory using LTB cosmology. However, if the galaxy mass results based on the LTB cosmology are proven to be similar to the ones from the standard cosmology, it could be inferred that the physical processes involved to form galaxies assuming both cosmologies are similar.

2.1 History of the Universe

In the stardard cosmological model, our Universe has expanded from a very dense and hot phase referred as the "the Big Bang" (hereafter, BB). From this point on, the Universe continued its long process of expansion and cooling, until eventually reached the state we see today. Fig. 2.1 shows the timeline and most important epochs of the evolution of the Universe.

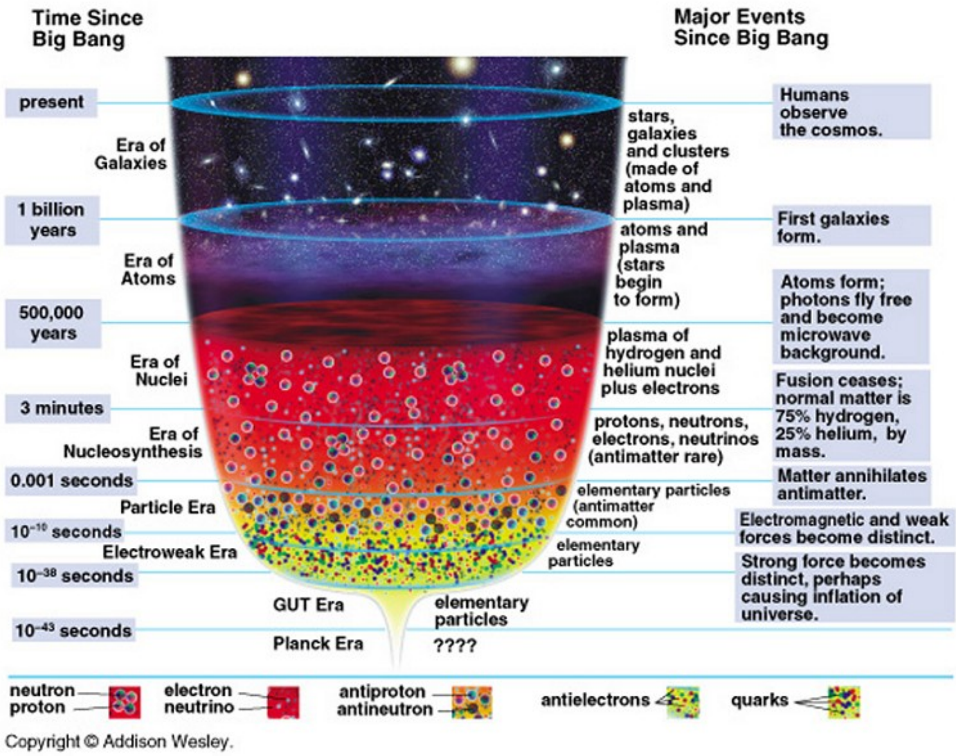

Figure 2.1: Timeline and major events since the Big Bang. Figure from Bennett *et al.* (2008).

Immediately after BB until 10^{-43}s is the Planck era, in which quantum effects of gravity were significant. It is believed that during this time the four fundamental forces - electromagnetism, weak force, strong force and gravity - were unified into one fundamental force. By the end of the Planck era, the temperature was around 10^{32}K and the Universe was filled with a vast range of subatomic particles created by the mechanism of pair production. At this time gravity separates from the other forces. Subsequently,the Universe entered at the grand unification theory epoch. During this time three of the four interactions unified as the electronuclear force. This situation lasted up until $\sim 10^{-35}$s when the strong nuclear force became distinguishable from electroweak force (unified weak and electromagnetic forces) and the grand unification theory epoch ended.

However, the understanding of these initial times are still tenuous to say the least. As a consequence of this separation, the Universe undergoes a brief period of exponentially accelerated expansion of the spacetime, known as cosmic inflation (for a review, see Linde 2014). Fig. 2.2 illustrates how inflation took regions of the universe that had already had time to communicate with one another, and so had established similar physical properties, and then dragged them far apart, well out of communications range of one another. In theory, in this

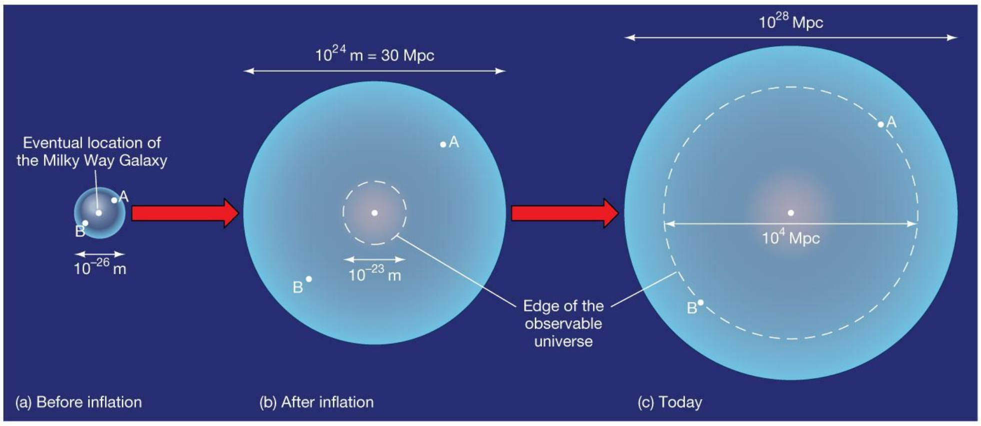

Figure 2.2: Representation of inflation effect in the Universe. In (a), points A and B are well within the (shaded) homogeneous region of the universe centered on the eventual site of the Milky Way Galaxy. In (b), after inflation, A and B are far outside the horizon (indicated by the dashed line), so they are no longer visible from our location. Subsequently, the horizon expands faster than the universe, so that today (c) A and B are just reentering our field of view. They have similar properties now because they had similar properties before the inflationary epoch. (Chaisson & McMillan 2011)

period, the Universe's original lumpiness was smoothed out, resulting the supposed homogeneity and isotropy seen in the present. Moreover, it was during this process that the quantum mechanical fluctuations become density fluctuations, which later seeded the formation of structures. Inflation should have lasted from $\sim 10^{-35}$s to $\sim 10^{-32}$s, however there is one order of magnitude uncertainty about these numbers.

After the expansion, it began the electroweak era in which the only electromagnetism and weak forces were still unified. Intense radiation filled all of space, as it had since the Planck era, spontaneously producing matter and antimatter particles that almost immediately annihilated each other and turned back into photons. As the Universe expanded and cooled, the interactions became less energetic and when the Universe was about 10^{-10}s old, the weak force is separed from the electromagnetism, ending the electroweak era.

While the Universe was hot enough to spontaneously create and annihilate particles, the total number of particles and photons were roughly in balance.

Once the temperature became too low for this spontaneous exchange of matter and energy to continue, photons became the dominant form of energy in the Universe. The period of time between the end of the electroweak era and the moment when spontaneous particles production ceased is known as particles era. In the first part of this era, photons continued, as they had in the Planck era, to turn into all sorts of exotic particles, including the building blocks of protons and neutrons - the quarks. By the end of particle epoch, all quarks had combined into protons and neutrons, and they shared the Universe with other particles such as electrons and neutrinos. This epoch ended when the Universe was about 1 millisecond (0.001 second) old and with temperature of 10^{12}K, and it was no longer hot enough to produce protons (or neutrons) and antiprotons (or antineutrons) spontaneously from pure energy. If the Universe had equal numbers of particles (protons and neutrons) and antiparticles (antiprotons and antineurtrons), at the end of this era all of the pairs would have annihilated each other, creating photons and leaving essentially no matter in the Universe. Therefore, it is easy to conclude that protons must have slightly outnumbered antiprotons at the end of the particle era. The size of this imbalance between matter and antimatter can be estimated by comparing the number of photons and protons existing today. At the very early Universe, the two numbers should have been similar, but today the photons outnumber protons by about a billion to one. We conclude that for every billion antiprotons in the early universe, there were about a billion and one protons. As a result, for each 1 billion protons and antiprotons that annihilated each other at the end of the particle era, a single proton was left over. This slight excess of matter over antimatter makes up all the ordinary matter in the present-day universe.

At 0.001s after the BB, protons and neutrons left over after the annihilation of antimatter began to fuse into heavier nuclei. However, the temperature of the universe remained so high that most nuclei broke apart as fast as they formed. Light elements such as deuterium, helium and lithium were created by the combination of free protons and neutrons in process called "primordial nucleosynthesis" (Steigman 2002). Because of this process, this epoch is known as era of nucleosynthesis, and it ended when the Universe was about 5 minutes old. At this stage, the temperature of the Universe was about a billion Kelvin and its ordinary matter was made of about 75% of hydrogen, 25% of helium with trace amounts of deuterium and lithium.

After the era of nucleosynthesis, the Universe became a very hot plasma of hydrogen nuclei, helium nuclei and electrons. A picture held for the next 380,000 years as the Universe continued to expand and cool. Throughout this period known as era of nuclei, photons bounced rapidly from one electron to the next, never managing to travel far between collisions. When a nucleus captured an electron to form a complete atom, one of the photons quickly ionized it. The era of nuclei ended when the Universe was about 380,000 years and the temperature had fallen to about 3000 K. Hydrogen and helium nuclei captured electrons forming stable, neutral atoms for the first time in a process named "recombination". Once electrons were bound into atoms, the Universe became transparent, and photons, formerly trapped among electrons began to stream freely across the Universe. The first photons released at this time are perceived today as the "cosmic microwave background" seen in Fig. 2.3.

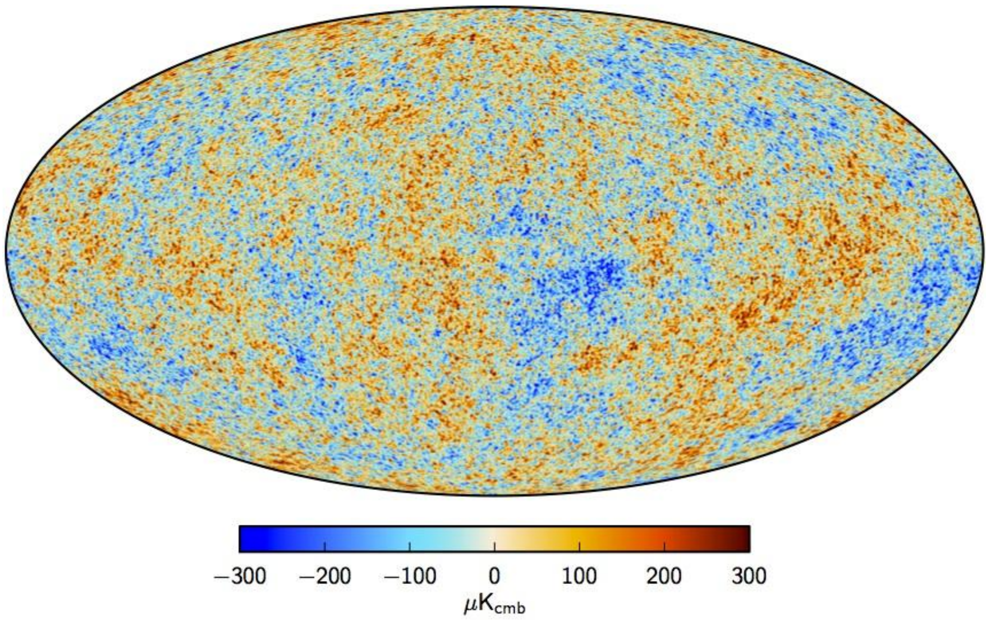

Figure 2.3: Comic microwave background intensity map at 5' resolution derived from the joint analysis of Planck, Wilkinson Microwave Anisotropy Probe and Haslam 408 MHz observations. Figure from Planck Collaboration I (2015).

After recombination, the intergalactic medium becomes neutral until the collapse of the first structures. Then, the era of atoms begins, with the universe consisting of a mixture of neutral atoms and plasma (ions and electrons), along with a large number of photons. Over the next few hundred million years the universe entered a crucial turning point in its evolution, known as the Epoch of Reionization. During this period, the predominant dark matter began to collapse into halo-like structures through its own gravitational attraction. Ordinary matter was also pulled into these halos, eventually forming the first stars and galaxies, which, in turn, released large amounts of ultraviolet light. That light was energetic enough to strip the electrons out of the surrounding neutral matter, a process known as cosmic reionization. A period between the cosmic microwave background and reionization is called 'dark ages', because the luminous stars and galaxies we see today had yet to form. The first galaxies had formed by the time the universe was about 1 billion years old, beginning what we call the era of galaxies. The era of galaxies continues to this day and it will be better explained in the next section.

2.2 Galaxy formation theories

The original environment of star formation is always a gas cloud. A giant molecular cloud can range from large clouds with masses of $10^5 - 10^6\mathcal{M}_\odot$ and sizes of a few tens of parsecs, to small 'cores' with masses of $0.1 - 10\mathcal{M}_\odot$ Giant molecular clouds present very homogeneous temperatures of about 10 K, large line widths of $\sim$ 10 km/s and short lifetimes of about $\sim 10^7$ years. However, the star formation efficiency in these clouds is very low, and stars seem to form only in the most massive clumps, resulting in a star cluster, or in the cores of giant molecular clouds, forming single stars. Star formation begins when a giant molecular cloud collapses under its own gravity, thus producing high densities and temperatures in the center, leading to the creation of a protostar that will start nuclear reactions and will become a star at later times.

There are two main theories trying to explain how galaxies form through time. In the next subsections, I will discuss both.

2.2.1 Monolithic collapse theory

It was proposed by Eggen, Lynden-Bell and Sandage (1962) to explain the formation of the Galaxy based on the kinematic study of solar neighbourhood stars. These authors verified that old stars from the Milky Way halo tend to have very elliptical orbits, characteristic of a free fall collapse formation, while young stars have a circular orbits, typical feature of the disk (see Fig. 2.4 for an illustration of the Galaxy components). This observation led to the proposal of the so-called *monolithic collapse model*, also known as *classical* and *top-down*.

In this scenario, a large spherical cloud of gas and dust collapses under its gravity, forming its first stars when the cloud was still round in shape. These first

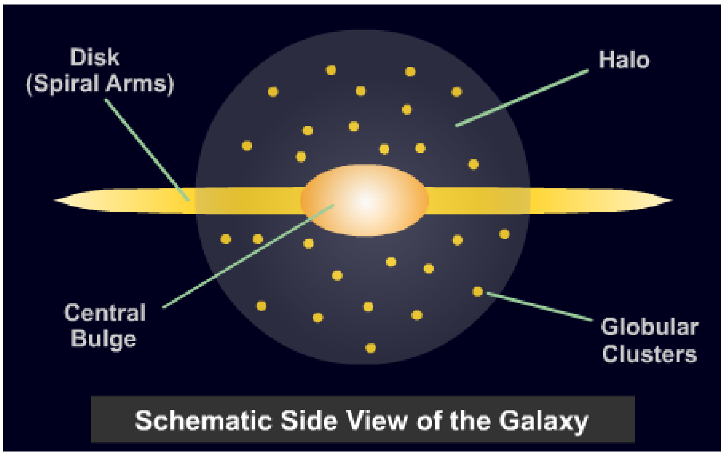

Figure 2.4: The Milky Way is a spiral galaxy, and it can be described by 3 basic components to its visible matter: the disk (containing the spiral arms), the halo, and the central bulge. The halo is an almost spherical shape galactic component which contains globular clusters, old stars and little gas, dust and star formation, besides it extends to large distances from the center of the galaxy. The disk is a flat shape galactic component mostly made of gas and dust, and young stars. The bulge is central component which has the highest density of stars in the galaxy. (Jones & Lambourne 2003)

stars are known as Population II and would eventually be part of the halo and the bulge of the Galaxy. Moreover, the orbits of these stars around the center of the Galaxy could have any orientation, accounting for the randomly oriented orbits of spheroidal population stars that we see today. Later, the conservation of angular momentum caused the remaining gas to flatten into a spinning disk as it contracted under the force of gravity. Stars that formed within the spinning gas disk are born on orbits moving at the same speed and in the same direction as their neighbours. These objects are known as Population I. Fig. 2.5 shows the Milky Way formation following this theory.

The name "monolithic collapse" comes from the idea of galaxy formation in a single event, i.e., the transformation of an initial population of giant gas clouds into stars, with elliptical galaxies and Population II portions of spirals being formed in a very fast initial event during the initial collapse towards a flat shape. Applying this picture to all types of galaxies suggests that,

- spirals may have experienced slow star formation in their early history, leaving enough gas to form a disk for later star formation or the galaxy rotates so rapidly that gas and dust stretched out into a disklike structure before the gas could be used in star formation;

- ellipticals form in a single intense starburst at high redshift at the same time as they collapse to equilibrium, then following a passive evolution;

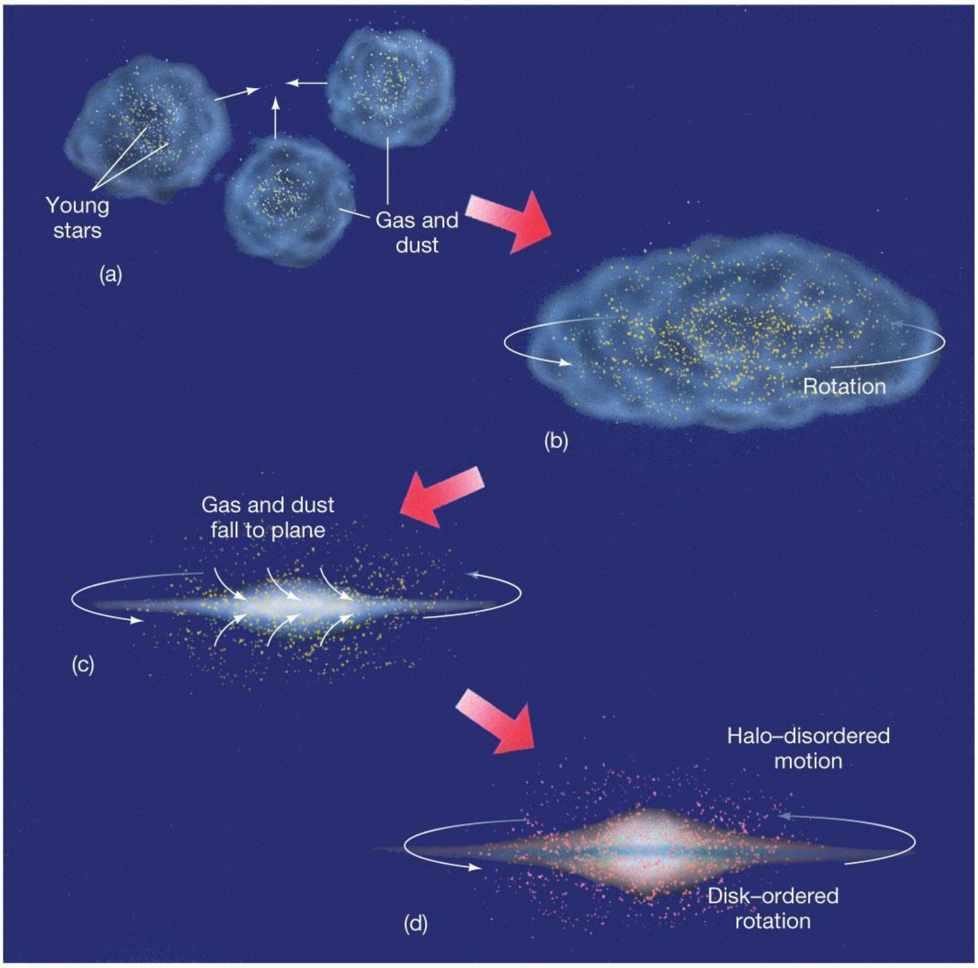

Figure 2.5: General picture of the Milky Way formation from a monolithic collapse perspective. Panel a) the protogalactic clouds begin to collapse under their own gravity, forming young stars. Panel b) more stars are created and together with the gas start to rotate. Panel c) the remaining gas settles into a spinning disk due to conservation of angular momentum. Panel d) a galaxy with random-motion old stars in the halo and forming stars in the disk (Chaisson & McMillan 2011).

- irregular galaxies probably arise from a variety of different and unusual circumstances, but they probably are affected by many of the processes that affect spirals and ellipticals.

This scenario has issues in explaining many properties of elliptical galaxies. For example, this model predicts that in an extreme dissipationless case all gas is transformed into stars prior to, or during, the collapse. The problem is that following this theory, and given the sizes and masses of observed ellipticals, these galaxies must have been formed at $z \sim 20$ in contrast with observations, which suggest that only a very small fraction of stars was formed before $z \approx 6$. Besides, under these assumptions violent relaxation cannot separate between stars and dark matter, thus producing the collapse of the total mass. This, again, is not in agreement with the observed matter distribution of elliptical galaxies, where most of the stars occupy a small central region surrounded by large dark matter halos. If the star-formation timescale is comparable or longer than the collapse, then dissipation can occur during the collapse, so the gas can separate from dark matter at the center of the potential well before turning into stars. Another point of conflict is that observational evidences (e.g., galaxy stellar mass function) show that at least 70% of the present day ellipticals were still forming stars or not yet assembled at $z = 1$ (e.g., Fontana *et al.* 2009), an opposite result if compared to theoretical predictions which imply that formation events should have happened before $z > 2$ and that galaxies should have evolved passively thereafter.

2.2.2 Hierarchical merging model

The merger scenario was first introduced by Toomre (1977) and it can be summarized by two assumptions, star-formation is supposed to happen only in disk systems and all ellipticals are the result of a major merger of two or more galaxies. The first assumption is reasonable because star formation in the local Universe seems to be restricted to the disk of spirals. The second one is more complex and the remnant of a merger between two galaxies has to resemble present-day ellipticals and the merger rate has to be consistent with the $z = 0$ population.

The general idea is that smaller objects build up to form bigger ones, and that is why this model is known as *hierarchical mergering* or *bottom-up*. There are different observational evidences that support this picture, such as, the very different morphologies, the greater fraction of spirals in galaxy clusters at high redshifts, beyond 1, and the predicted scatter in the color-magnitude relation is small as observed.

In this theory, the first structures to be formed are more or less relaxed and virialized objects called 'halos', which at this point have low masses of dark matter and baryons. At large scales, the distribution of dark matter and baryons are assumed to be uniform. While at small scales they are not. To begin, the clumps collapse forming halos, first at small then at large scales. The baryonic matter collapses in these halos, increasing its temperature then cooling again, and finally settling in the form of a disk where eventually stars form. As most of the mass is made of cold (non-relativistic particles) dark matter (it does not absorb or emit radiation), the galaxy formation is driven by dark matter and the baryons are only supporting characters.

The effect of a merger in a galaxy depends on a range of parameters, such as the mass of the galaxies involved, the amount of gas and angular momentum in each object, etc. In general, two types of mergers can be considered: "minor mergers" and "major mergers". If a small galaxy with mass $\mathcal{M}_1$ merges with a more massive one (e.g., $\mathcal{M}_2 \approx 10\mathcal{M}_1$), the effect of the first over the second is small. Then, when the process ends, the stars of the first object will become part of the second but will keep their original kinematic properties, and no significant change will be seen in the massive galaxy. This case is a minor merger. If the interaction involves two galaxies with comparable mass (e.g., $\mathcal{M}_2 \approx 2\mathcal{M}_1$), then the disk will be destroyed and its stars will increase their velocity dispersion and create a spheroidal component. Gas clouds collide causing big starbursts. If the remaining gas is ejected through a violent interaction, the resulting system will be a galaxy dominated by the spheroidal component. Nevertheless, if a significant amount of gas resists the merger, the gas might settle into a new disk. Therefore, in this scenario the morphological type of a galaxy may change.

One can also distinguish mergers analyzing its components, if the system has gas and, therefore, it can produce starbursts the merger is wet; on the other hand if the system has no gas and no star formation, the merger is dry.

In the hierarchical model of galaxy formation, the gas in merging dark matter halos collapses inwards in a smooth fashion and it builds disks and stars form slowly. The merger of these disks would lead to spherical systems and if there is sufficient gas a slow accretion would again form a disk. One of the strengths of this model is that it explains the large variation in different types of galaxies that we observe throughout the history of the universe. This is because there is not one specific time when certain types of galaxies had to form and galaxies can evolve through many forms throughout their history.

Note that in the classic model, galaxies evolve in a pre-determined fashion depending on the initial conditions, such as rotational velocity, and with relatively little impact from the surrounding environment. In contrast, the hierarchical model proposes that galaxies form and evolve through successive mergers of smaller bodies and their fate is more dependent on the environment which they inhabit. As an example, for each elliptical galaxy, in the classic model, there is a well-defined star formation time after which the galaxy remained more or less constant in mass, size and shape, and it is formed by the collapse of a gaseous cloud at an early epoch over a short timescale. While in the hierarchical model the stars might form at different times over an extended period involving a diversity of progenitors (stellar disks, bulges, gaseous disks and clouds) and the galaxy may grow continuously by accretion and merger.

It is important to emphasize that despite its success as a model of universal evolution over long periods, the predictions made by the CDM cosmological model diverge from observational data in several ways, especially at small scales. These contradictions include the cusp-core problem in which simulations predict a density peak of dark matter at the centers of halos,"cuspy", while the majority of galaxy rotation curves indicate a constant density core (Dubinski & Carlberg 1991; Walker & Peñarrubia 2011)*, the Too-Big-To-Fail problem in which the predicted masses of satellites galaxies are significantly higher than observationally inferred values (Boylan-Kolchin *et al.* 2011, 2012; Local Group: Kirby *et al.* 2014, Garrison-Kimmel *et al.* 2014; field galaxies: Papastergis *et al.* 2015).

2.3 Evolution of galaxies

In order to understand how the galaxies evolve through cosmic time, it is necessary to know the effects or processes that may play a role in the evolution of galaxies and its timescale of action. Next I will discuss the importance of the environment, and define the feedback and the downsizing.

2.3.1 Feedback

The evolution of baryons inside the dark matter halos is an important and complicated subject. The way to take into account the baryonic physics is adding the so-called *feedback* that refers to the collection of complex processes through which star formation and accretion onto black holes deposit energy and momentum back into their surroundings. There are two main sources of feedback: stars and active galactic nuclei (AGN). In the literature, it can be found a more comprehensive discussion about feedback, here we give a more general approach to the subject, leaving out specific details about the influence of magnetic fields and winds from Asymptotic Giant Branch stars.

*In the literature, there are at least two approaches that could potentially solve this issue, one using cosmological solutions (change the spectrum at small scales, e.g. Zentner & Bullock 2003; different nature of dark matter particles, e.g. Peebles 2000; or modified gravity theories, e.g. Milgrom 1983), and the other through astrophysical solutions, which are based on the concept that the dark matter content in a galaxy expands due to a "heating" mechanism resulting in a inner density reduction (e.g. Navarro *et al.* 1996, Cole *et al.* 2011).

At the beginning, the baryons are in the form of a hot gas. The gas cools down and starts to gather in a disk, and if it gets dense enough this gas is partially transformed into stars. The massive stars explode as supernova, causing a good amount of energy to be transferred into the interstellar medium. If the outflow is accelerated to a velocity that is higher than the escape velocity of the galaxy, it is ejected into the intergalactic medium, suppressing the star formation rate. This phenomenon is known as *stellar feedback* and it is very efficient in removing gas from galaxies towards lower mass dark matter halos (e.g., Larson *et al.* 1980). At the same time, this type of feedback mainly driven by supernova explosions has little impact on the formation of massive galaxies. But, an energy budget analysis suggests that in such massive galaxies the supermassive black holes in AGN release an amount of energy up to a factor 20-50 higher than from supernovae, this energy it would be enough to suppress the star formation. This process is named *AGN feedback*. Fig. 2.6 shows the simulation predictions and the observed luminosity function, and how the input of baryonic physics can help both functions to agree. At low luminosities, the stellar feedback, given by supernovae (indicated as SN in the figure), can be responsible for the deviation of observed LF from the theory, while at high luminosities, the mechanism that leads to the mismatch between observations and theory is the AGN feedback.

Another plausible effect is the star formation, induced, enhanced and quenched by the supermassive back hole outflows. Netzer (2010) demonstrates the close connection of AGN luminosity and star formation rate over a wide dynamical range. If the star formation is triggered by the AGN-driven outflows, then the outflow momentum is amplified by supernovae. Therefore, the momentum supplied to the gas is boosted by a combination of AGN and star formation. However the phenomena could be mutually self-regulating. A more refined analysis should consider the nature of the black hole growth.

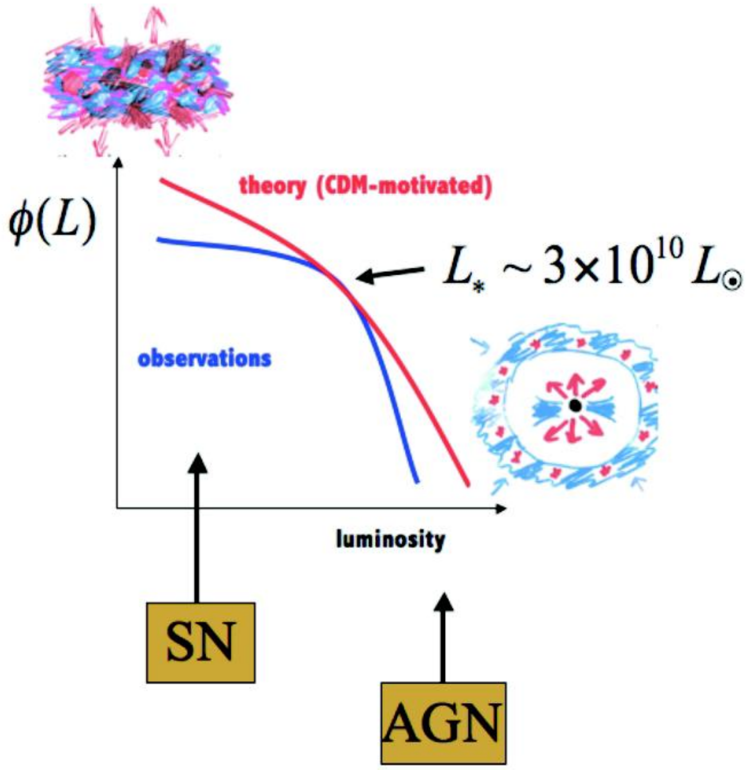

Figure 2.6: The theoretical mass function of galaxies compared to the observed luminosity function. Figure from Silk (2011).

2.3.2 Downsizing of galaxies

As already mentioned, the hierarchical theory favours a build up scenario, where the first haloes to form are the smallest ones, while there is observational evidence in favour of most massive galaxies with old stellar population already being in place at high redshifts. This effect is called *downsizing* of galaxies (Cowie *et al.* 1996). One can find different types of downsizing, for example, in stellar mass (e.g., Pérez-González *et al.* 2008), in star formation (e.g., Bundy *et al.* 2006).

At first sight, the downsizing effect seems anti-hierarchical because it allows massive galaxies at early epochs, however this is not necessarily true. While the main progenitor of a galaxy shows the usual hierarchical behavior, the integrated mass over all the progenitors down to a given minimum mass shows downsizing that is similar to what has been observed. In this sense, downsizing of galaxies can be partly environmental, a natural outcome of the bottom-up clustering process of dark matter haloes. Besides, even if the more massive halos assemble later, their progenitors form earlier, so the stellar population of a massive halo can be old.

2.3.3 Environment

The environment can play a decisive role in the life of a galaxy. In galaxy clusters, for example, a big number of galaxies are fairly close to each other and moving with high velocities ($\sim 700 - 1000$km/s), within a intergalactic medium of a really hot gas (millions of K). So, most of the baryonic matter in clusters is in form of hot gas, not in galaxies. A spiral galaxy that falls into the cluster may lose its gas due to ram-pressure and tidal forces of other close galaxies. Moreover, part of the stars of this galaxy may also lose stars due to tidal forces, creating a diffuse halo around the center of the cluster. At the same time, the dynamic friction, makes the galaxy migrate to center regions of the cluster. In the end of this process, the original spiral galaxies becomes a S0 elliptical.

Chapter 3

From photometric surveys to galaxy stellar mass

> "Science is more than a body of knowledge. It's a way of thinking; a way of skeptically interrogating the Universe with a fine understanding of human fallibility."
>
> *Carl Sagan*

The main source of information about properties of distant, unresolved galaxies are the integrated SEDs. Indeed, the different physical processes occurring in galaxies leave their imprint on the global and detailed shape of the spectrum, each dominating at different wavelengths. Therefore, a detailed study of a SED of a galaxy should allow a better understanding of its physical properties. The SED fitting is an attempt to derive one or several properties simultaneously from fitting models or empirical galaxy templates to an observed SED. This technique is widely used and it takes advantage of the vastly increased volume and quality of available photometric data in the different regimes of the electromagnetic spectrum.

A earlier application of the SED fitting was to estimate the photometric redshift (photo-z), as a manner to extrapolate the early spectroscopy data (Baum 1957). The photo-z estimation is complex and it has distinct aspects from all the other estimates of physical properties due to independent and more precise measurements of the same property for large samples in the form of spectroscopic redshifts. The method can thus be tested extensively and even calibrated empirically. As the aim of this chapter is to present an overview of the SED fitting process to obtain physical properties, particularly the stellar masses, we leave out the special case of the photo-z and assume its values as known. In addition, this chapter focuses on the general description of the astrophysical assumptions applied on the SED fitting, excluding the cosmology. A comprehensive discussion of the effects of the cosmology in the stellar mass estimation is presented in a following chapter.

3.1 SED fitting procedure

The SED fitting procedure is based on the fit of the overall shape of the photometric data and on the detection of the strong spectral properties. The observed photometric data points are compared to synthetic SEDs obtained from a set of models or empirical templates. The best-fit SED of an object corresponds to the one synthetic SED that better reproduces the shape of the observed data, which can be quantified through the standard χ^2 minimization procedure,

$$\chi^2 = \sum_{i=1}^{N_{filters}} \left[\frac{F_{obs,i} - A \times F_{tem,i}}{\sigma_i} \right]^2 \tag{3.1}$$

where $F_{obs,i}$ and σ_i are the monochromatic observed flux and its error in the band i, $F_{temp,i}$ is the monochromatic flux from the synthetic SED and A is the normalization constant. The adopted models are generated with well-known properties (ages, metallicities, etc) so the resulting best-fitting SED contains all the important information about the stellar population of that particular galaxy. A different series of assumptions results in a different library of available synthetic SED resulting in a distinct best-fit SED. Therefore, the choice of the set of input parameters to construct the synthetic SEDs is crucial.

The synthetic SED library is generated by assuming a stellar population synthesis models, a grid of metallicities, an extinction law with a range of reddening color excess $E(B-V)$ values, an IMF and a star formation history (SFH). A discussion about the creation of this library and its assumptions are presented in the next section.

3.2 Synthetic SED library

In a simple generic picture, a galaxy is a population of stars ranging from numerous, low-luminosity, low-mass stars, to the bright, short-lived, massive stars, with different metallicities and ages ranging from when the galaxy first formed to those recently born. Then, the emitted light from the whole population is just the integrated spectra of each single star. The method of creating a galaxy spectrum through the sum of the spectra of its stars is called *stellar population synthesis* (SPS). A comparison between spectra from different galaxies and stellar types is shown in Fig. 3.1, in which one can directly note similarities in the spectra from the galaxies and the underlying stellar types. By eye, it can be seen that most of the emitted light from the starburst galaxies can be matched by the spectra from OB-type stars, while in the spiral and elliptical galaxies there is an obviously strong G-star component. However, the strong, broad titanium monoxide (TiO) features characteristic of M-type stars appear in the spiral and elliptical spectra, so these M-type stars must also be present. This example shows how complex can be the analysis of a galaxy spectrum.

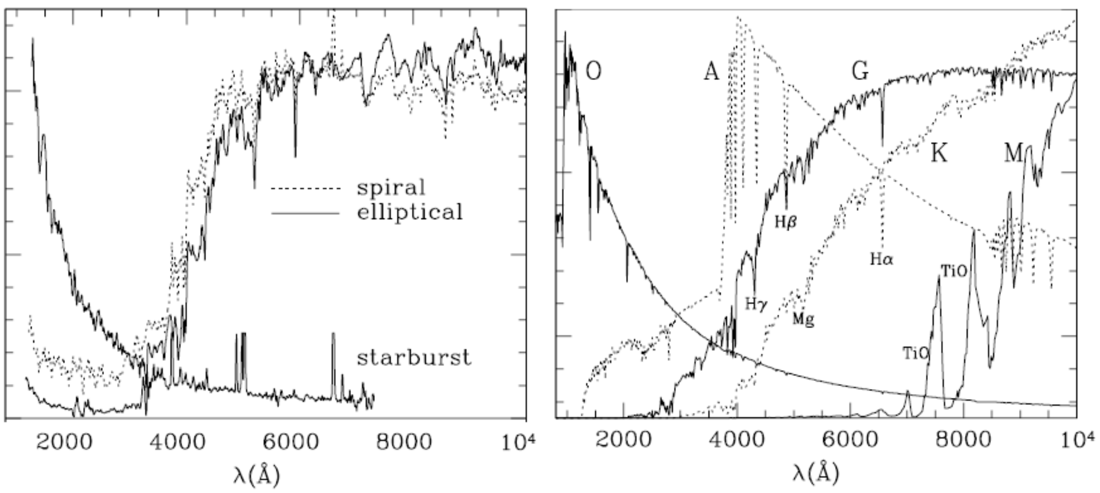

Figure 3.1: Example of galaxy (left) and star (right) spectra in arbitrarily scaled flux f_λ versus wavelength. The strongest emission lines in the starburst spectrum were truncated for clarity, and a few important spectral features are marked on the stellar spectra. This is the basic idea behind the SPS analysis: adding the star spectra together in different combinations and with different multiplicative weights. (Encyclopedia of Astronomy and Astrophysics 2001, pp.4791).

The SPS modelling relies on an accurate description of the evolution of stars, which can be guided by observed nearby stars and star clusters where stars can be studied one by one, and theoretical models of stellar evolution and stellar atmospheres. Besides the detail prescription of how the stars evolve, the SPS models also depend on others ingredients, such as the IMF, the metallicities, the dust extinction. In the next sections, the assumptions involved in the SPS modelling will be introduced.

3.2.1 Stellar population synthesis models

The first attempts to reproduce the observed spectra in terms of their stellar content was based on a trial and error analyses (e.g., Spinrad & Taylor 1971; Faber 1972; O'Connell 1976; Turnrose 1976; Pritchet 1977; Pickles 1985), where a model is constructed using the relative proportions of the stars that best matched the galaxy spectrum. This form of population modelling is often termed empirical population synthesis. This technique was later abandoned due to the large number of free parameters to constrain a typical galaxy spectra. Later, other models based on stellar evolution theory were developed, in which the simplest class of models are the single simple stellar populations. In these, all the stars are formed at the same time, with distribution in mass given by a chosen IMF, and with identical chemical composition. Single simple stellar populations can be calibrated with globular clusters data, since these are the simplest stellar populations in nature with ages and element abundances independently known (Renzini & Fusi Pecci 1988).

There are different approaches adopted to compute single stellar population models, including the evolutionary population synthesis or isochrone synthesis (e.g., Chiosi *et al.* 1988; Charlot & Bruzual 1991; Bruzual & Charlot 1993) and the fuel consumption based algorithms (e.g., Renzini & Buzzoni 1986; Maraston 1998, 2005), which differ according to the integration variable adopted in the post-main sequence phase*. Until the end of the main sequence, both techniques apply the same concept the theoretical stellar evolutionary isochrones, which are made from a collection of evolutionary tracks for different masses of stars. A track describes the luminosity and effective temperature of a star of a given mass with time. An isochrone shows the locus of luminosities and temperatures at one instant in time for stars of all masses, and thus is built to mimic a star cluster or a single-age stellar population. The SED derived from this methodology is obtained by summing the spectra of individual stars along the isochrone. For the first method, the isochrones usually are computed up to the end of the early asymptotic giant branch phase and later stellar phases are often neglected

*The stars spend most of their lifetime in the main sequence, where they burn the hydrogen contained in their nucleus.

or added following individual recipes. For the second method, the integration variable in post-main sequence phase is the fuel, i.e., the amount of hydrogen and/or helium that is consumed via nuclear burning during a given post main sequence phase. A typical way to express the single stellar population spectrum f_{SSP} is through a time and metallicity-dependent that can be written as

$$f_{SSP}(t, Z) = \int_{m_{lo}}^{m_{up}(t)} f_{star}[T_{eff}(\mathcal{M}), \log g(\mathcal{M})|t, Z]\Phi(\mathcal{M})\mathrm{d}\mathcal{M}, \qquad (3.2)$$

where $\mathcal{M}$ is the initial (zero-age main sequence) stellar mass, $\Phi(\mathcal{M})$ is the IMF, f_{star} is a stellar spectrum, T_{eff} is the effective temperature of a star of given mass, $\log g$ is the surface gravity, m_{lo} is typically given by the hydrogen burning limit, ~ 0.08 or $0.1\mathcal{M}_{\odot}$, and the upper limit $m_{up}(t)$ is given by stellar evolution. Fig. 3.2 shows a schematic picture with the entire process of constructing a single stellar populations.

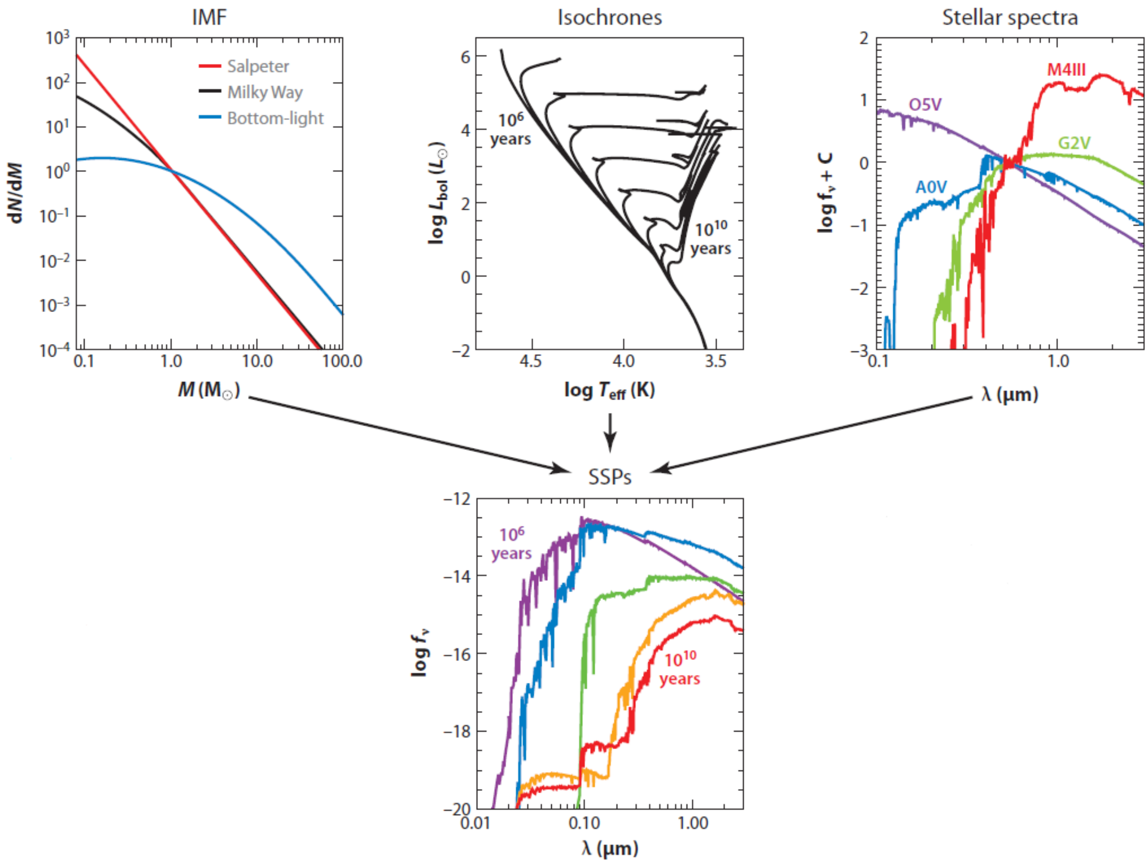

Figure 3.2: Overview of SPS to create a single stellar population. In the first line are the ingredients to construct a single stellar population: an IMF, isochrones for different ages and metallicities, and stellar spectra (flux f_ν versus wavelength λ) from a range of effective temperatures, luminosities and metallicities. Figure adapted from Conroy (2013).

More complex stellar systems known as the composite stellar population models are made up by various stellar generations modelled by convolving single stellar populations with the adopted SFH (e.g., Barbaro & Poggianti 1997; Bruzual & Charlot 2003). Besides the stars with a range of ages given by their SFH, the composite stellar population flux f_{CSP} contains also stars with a range in metallicities as given by their time-dependent metallicity distribution function $P(Z,t)$ and dust. These ingredients can be combined as,

$$f_{CSP}(t) = \int_{t'=0}^{t'=t} \int_{Z=0}^{Z_{max}} (SFR(t-t')P(Z,t-t')f_{SSP}(t',Z)\exp(-\tau_d(t'))+Af_{dust}(t',Z))\mathrm{d}t'\mathrm{d}Z, \tag{3.3}$$

where the stellar population age t' and metallicity Z are the integration variables, $\tau_d(t')$ is the dust optical depth used to model the dust attenuation, f_{dust} is a function applied to incorporate the dust emission, and A is a normalization constant obtained by balancing the luminosity absorbed by dust with the total luminosity reradited by dust. The SFR is set arbitrarily, and its most popular form is the exponential decay, $SFR \propto \exp(-t/\tau)$, where τ is the time scale related to when the star formation began. $P(Z,t-t')$ is usually assumed to be a δ-function, which means a single metallicy is adopted for the entire composite population. Fig. 3.3 shows an overview of the process of constructing composite stellar populations, with the single populations previously derived, following the procedure in Fig. 3.2.

A good example of how the simple and composite stellar population affect the resulting spectra is seen in Fig. 3.4, in which a set of synthetic SED according to the Bruzual & Charlot (1993) model, with a Salpeter IMF and a solar metallicity, has two SFH: one where the stars form instantaneously at $t = 0$, and the other where the star formation decays exponentially. More advanced models take evolutionary processes into account, i.e., enrichment of the interstellar medium, differential loss of various element by galactic winds, time-dependent IMF, etc.

In a practical note, throughout this thesis, I use the composite stellar population models from Bruzual & Charlot (2003) to compute a synthetic SED library applied in the SED fitting procedure. This model adopts the previously discussed isochrone synthesis technique with an additional observationally motivated prescription for the thermally-pulsing stars on the asymptotic giant branch†. These stars are very bright and have a strong influence on the integrated properties.

†Asymptotic giant branch is an advanced phase in the stellar evolution of low-to-intermediate-mass stars.

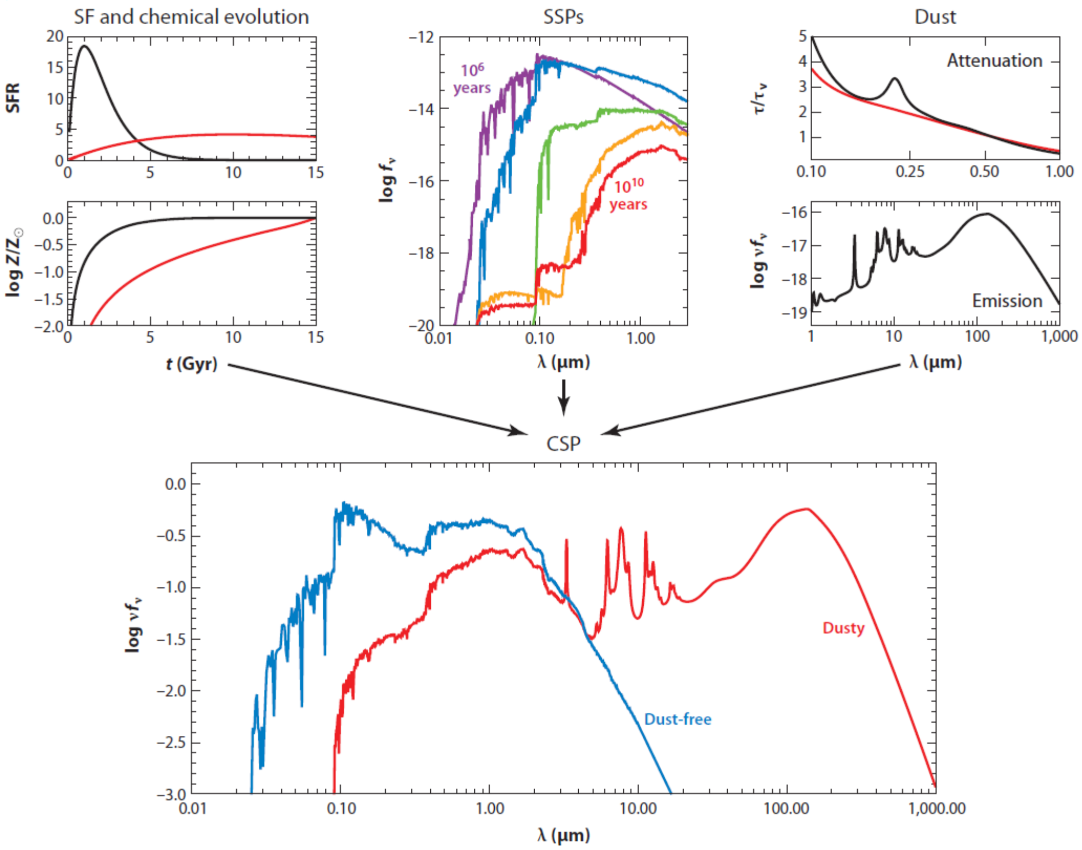

Figure 3.3: Overview of stellar population synthesis to create a composite stellar population. In the first line are the ingredients to build a composite stellar population: SFH and chemical evolution, single stellar populations, and a model for dust attenuation and emission. The black and red solid lines from the first panel in the left are related to two scenarios, a single burst of star formation and a continuous SFH, respectively. Figure adapted from Conroy (2013).

The characterization of the thermally-pulsing asymptotic giant branch stars is supported by observations of surface brightness fluctuation in nearby stellar populations.

3.2.2 Initial mass function

The number of stars born at a given mass is described by the IMF $\Phi(\mathcal{M})$. It is usually limited between a minimum and maximum stellar mass, generally $\mathcal{M}_{min} \sim 0.05 - 1.0\mathcal{M}_{\odot}$, $\mathcal{M}_{max} \sim 100 - 150\mathcal{M}_{\odot}$, and is supposed to be a continuous function that is usually normalized as,

$$\int_{\mathcal{M}_{min}}^{\mathcal{M}_{max}} \varphi(\mathcal{M})\, \mathrm{d}\mathcal{M} = 1\mathcal{M}_{\odot}. \tag{3.4}$$

In 1955, the first IMF in the solar neighbourhood was determined by Salpeter,

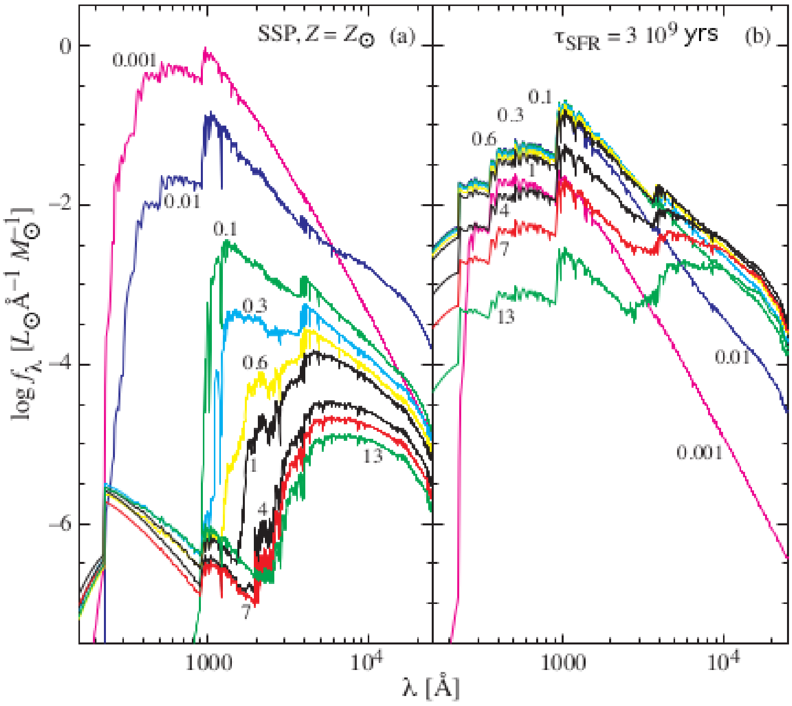

Figure 3.4: Evolving spectral energy distributions. (a) Evolution in time of the SED of a single stellar population computed for the Salpeter IMF. The age in Gyr is indicated next to each spectrum. (b) Same as (a) but for a composite population in which stars form according to an exponential SFH $\Psi(t) = \exp(-t/\tau)$ for $\tau = 3$ Gyr. F_λ in frame (b) has been multiplied by 100 to use a common vertical scale. Adapted from Bruzual (2001).

who found

$$\varphi(\mathcal{M})\,\mathrm{d}\mathcal{M} \propto \mathcal{M}^{-b}\,\mathrm{d}\mathcal{M}, \tag{3.5}$$

with $b = 2.35$. More recently, Kroupa (2002) obtained for stars near the Sun a broken power-law, with similar shape as the Salpeter IMF but flattens at lower masses,

$$\varphi(\mathcal{M}) \propto \begin{cases} \mathcal{M}^{-2.3}\ , & 1.0\mathcal{M}_\odot < \mathcal{M} \\ \mathcal{M}^{-2.7}\ , & 0.5\mathcal{M}_\odot < \mathcal{M} < 1.0\mathcal{M}_\odot \\ \mathcal{M}^{-1.8}\ , & 0.08\mathcal{M}_\odot < \mathcal{M} < 0.5\mathcal{M}_\odot \\ \mathcal{M}^{-0.3}\ , & 0.01\mathcal{M}_\odot < \mathcal{M} < 0.08\mathcal{M}_\odot . \end{cases} \tag{3.6}$$

A study of the IMF in diverse components of the galaxy, such as stars located on the disk, bulge or in globular clusters was done by Chabrier (2003), who found that all the IMFs have similar forms. For the stars in the disk, the IMF is given by a combination of a power-law for higher masses and a lognormal for lower masses,

$$\varphi(\mathcal{M}) \propto \begin{cases} \mathcal{M}^{-1.35}\ , & \mathcal{M} > 1.0\mathcal{M}_\odot \\ \exp\{-[\log(\mathcal{M}/0.2\mathcal{M}_\odot)]^2/0.6\}\ , & \mathcal{M} < 1.0\mathcal{M}_\odot . \end{cases} \tag{3.7}$$

These three empirical forms are the most commonly used, although many others IMFs can be found in literature (e.g., Tinsley 1980; Scalo 1986 or Scalo 1998). An illustration of the behavior of the different IMFs is shown in Fig. 3.5.

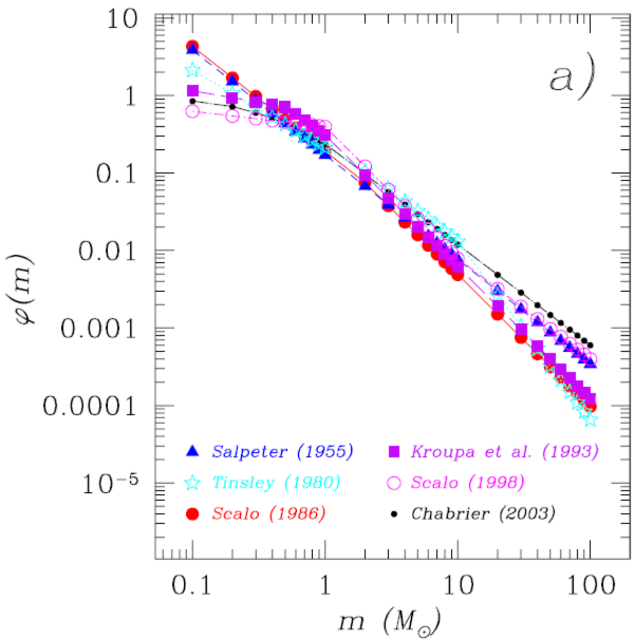

Figure 3.5: Stellar IMF according to Salpeter (1955), Tinsley (1980), Scalo (1986), Kroupa *et al.* (1993), Scalo (1998) and Chabrier (2003). (Reproduced from Romano *et al.* 2004).

In principle, the IMF could vary not only from galaxy to galaxy but within the galaxy itself. Observations of the Milky Way seem to suggest that the IMF is independent of the galaxy location. However whether this holds in all conditions and for all redshifts is still an open question (Corbelli, Palla & Zinnecker 2005). Nevertheless, a review by Bastian, Covey & Meyer (2010) emphasizes that there is no compelling evidence for variation on the IMF from direct probes, i.e., star counts. Generally the IMF is considered to be universal.

The IMF affects the SPS results regarding the overall normalization of the stellar mass-to-light ratio, the rate of luminosity evolution for a passively evolving population, the SED of composite stellar population, and it has an small effect on the shape of the SED of simple stellar population.

3.2.3 Metallicity

The metallicity is defined as the amount of heavy elements, like iron (Fe), in a galaxy. Thus, high metallicity means the presence of many heavy, metal elements. There are two ways to express the metallicity, the first uses the iron and hydrogen, $[Fe/H]$, and the second uses a set of heavy elements represented by Z. Stars with higher metallicities evolve faster, and increase the amount of metals producing redder colors in their spectra. The SED from this population of stars with very high metallicity has a very similar shape to that of an older population with less metallic content. This causes the effect known as the age-metallicity degeneracy. A practical example can be seen in Fig. 3.6. This degeneracy can be broken by the use of additional information from emission lines and/or metal lines.

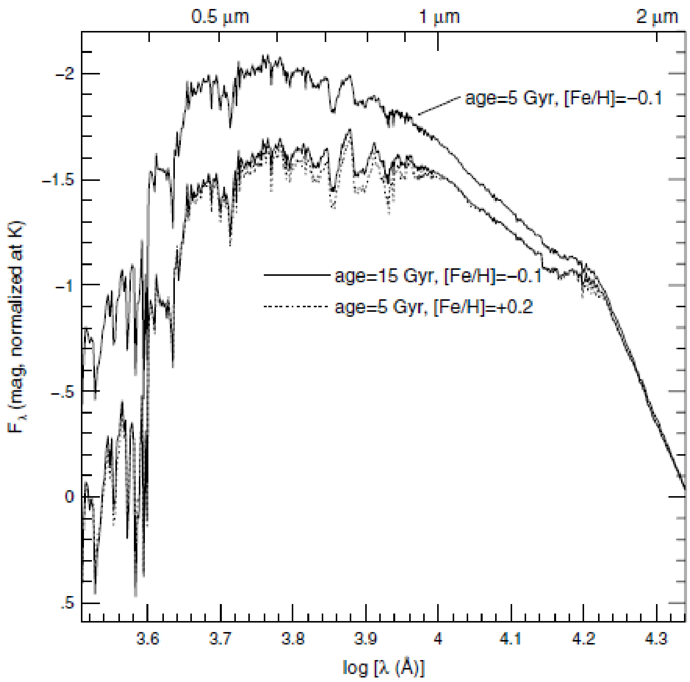

Figure 3.6: Model spectra that illustrates the age−metallicity degeneracy. The base population is age 5 billion years, with slightly less than solar metallicity. There are two variations of this population, one has age tripled, and the other has metallicity doubled (Encyclopedia of Astronomy and Astrophysics 2001, pp.4795).

From the perspective of the SPS using photometric data, it is important to take advantage of optical-NIR data to break the age−metallicity degeneracy. Nevertheless, it is essential to emphasize that the age and metallicity can be separated in the context of a particular SPS model, but this estimation will vary from model to model (Lee *et al.* 2007; Eminian *et al.* 2008).

3.2.4 Extinction law

Part of the light emitted by the stars is absorbed by the dust in the interstellar medium. At shorter wavelengths (i.e., ultraviolet, optical), this effect, known as dust extinction, is more relevant, causing the resulting spectra to be redder. Therefore, to take into account this effect when reproducing or analyzing a spectrum, the *extinction law*, i.e., the variation of extinction with wavelength, must be known.

The dust extinction in at given wavelength λ can be described in terms of the optical depth τ_λ, which is the measure of how opaque a medium is to the radiation in a certain λ. The extinction at λ (in magnitudes) is defined as

$$A_\lambda = \tau_\lambda \, 2.5 \log \mathrm{e} = 1.086 \, \tau_\lambda, \tag{3.8}$$

and the difference of the extinction in two bands λ_1 and λ_2 can be expressed by the color excess, defined as

$$E(\lambda_1 - \lambda_2) = A_{\lambda_1} - A_{\lambda_2}. \tag{3.9}$$

It is standard to adopt the color excess between the B and V bands. Based on these definitions, the dust extinction can be expressed in the form of an empirical extinction law $k(\lambda)$ given as,

$$k(\lambda) = \frac{A_\lambda}{E(B-V)} = R_V \frac{A_\lambda}{A_V}, \tag{3.10}$$

where $R_V = A_V / E(B-V)$.

The extinction law is related to the optical depth, which can be identified with the dust attenuation cross-section σ_λ and the dust density column N,

$$\tau_\lambda = \sigma_\lambda N. \tag{3.11}$$

Therefore, the extinction law depends on the physical properties and composition of the dust grains, as well as on the geometry of the dust cloud. Nevertheless, in practice, generally, it is used empirical extinction laws based on different local galaxies, such as the Milky Way (Allen 1976), the Large Magellanic Clouds (Fitzpatrick 1985), the Small Magellanic Clouds (Prevot *et al.* 1984). For high redshift objects, a curve based on a sample of galaxies undergoing intense star formation, the starburst galaxies, was derived from Calzetti *et al.* (2000), and has been widely used.

Fig. 3.7 shows the shape of the different extinction curves. For Milky Way and Large Magellanic Clouds, the strong feature seen at 2175Å, which can be understand as a product of graphite dust grains. This bump at 2175Å is not observed in the curve from Small Magellanic Cloud or starburst galaxies.

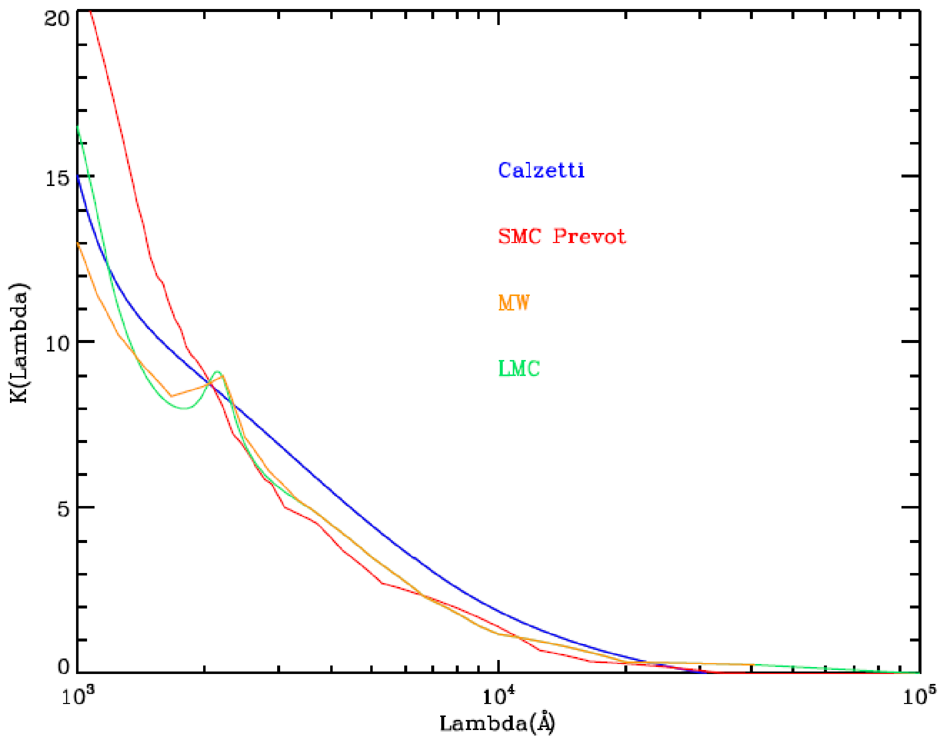

Figure 3.7: Extinction curves for different extinction laws derived for the starburst galaxies (Calzetti, blue solid line), the Small Magellanic Clouds (SMC, red solid line), the Milky Way (MW, orange solid line), the Large Magellanic Clouds (LMC, green solid line).

3.3 Stellar mass

The stellar mass is one of the resulting physical properties obtained by the SED fitting procedure.In simple terms, the stellar mass of a galaxy is estimated by multiplying the mass-to-light ratio $\mathcal{M}_{stellar}/L$ by a luminosity L. L is directly related to the observed flux, and therefore it depends on the quality of the data and of the redshift measurements. Meanwhile the estimate over $\mathcal{M}_{stellar}/L$ is mostly associated to the assumptions taken on the SED fitting (e.g., Conroy, Gunn & White 2009). Additionally, the broad-band SPS fitting technique has an inherent bias related to a preferentially matching of the flux from the bright, young stars, what could potentially under-estimate the $\mathcal{M}_{stellar}/L$ ratio by missing the relatively low flux from the older stars. This bias arises from the lack of knowledge of the SFH of any particular galaxy. Hence, in the synthetic models a form for the SFH is assumed and parametrized to account for many possible histories. A deeper analysis of it can be found in Gallazzi & Bell (2009), Maraston *et al.* (2010), Pforr, Maraston & Tonini (2012), Sorba & Sawicki (2015).

There are many different studies in the literature about uncertainties in the stellar masses, either focusing on the techniques (e.g., Guidi, Scannapieco & Walcher 2015), or analyzing the combination of different input parameters to the simulated catalogs (e.g., Wuyts *et al.* 2009; Lee *et al.* 2012; Pforr *et al.* 2012). This thesis does not aims at investigating these issues, however for completeness reasons in the next subsection a brief overview of recent results concerning the uncertainties related to the input parameters to generate the synthetic SED is presented. Moreover, this discussion can be used as reference and later be qualitatively compared with the results for different cosmologies in chapter 4. In this sense, a part of this thesis complements these studies, analyzing the dependence of the estimated stellar masses on cosmology, which was not explored so far.

3.3.1 Errors and uncertainty in stellar mass measurements

A recent paper from Mobasher *et al.* (2015) made a comprehensive investigation of the main sources of errors in the stellar mass estimates for galaxies. Given different parameters affecting stellar mass measurement (photometric signal-to-noise ratios S/N, SED fitting errors and systematic effects), the inherent degeneracies and correlated errors, the authors formulated different simulated galaxy catalogues to quantify these effects individually. For comparison, they generated catalogues based on observed photometric data of real galaxies in the GOODS-South field, spanning 13 filter from U-band to mid-infrared wavelengths. The analysis was done by the Cosmic Assembly Near-infrared Deep Extragalactic Legacy Survey collaboration, with different combinations of stellar mass measurement codes/methods, population synthesis models, star formation histories, extinction and age. For each simulated galaxy, the differences between the input stellar masses, $\mathcal{M}_{input}$, and those estimated by each team, $\mathcal{M}_{est}$, is defined as $\Delta\log(\mathcal{M}) \equiv \log(\mathcal{M}_{est}) - \log(\mathcal{M}_{input})$, and is used to identify the most fundamental parameters affecting stellar mass estimate in galaxies. A total of 10 teams participated in this study. The stellar masses were estimated from different catalogues: an empirical mock catalogue (TEST-1), a Semi-Analytic Mock catalog (TEST-2) and a "real" observational catalogue (TEST-3 and TEST-4).

TEST-1 was related to the methodology in which 10 approaches were tested to obtain the stellar mass: `GalMC` (Acquaviva *et al.* 2011), `EAZY` (Brammer *et al.* 2008), `SATMC` (Johnson 2013), `HyperZ` (Bolzonella *et al.* (2000), `Le Phare` (Arnouts & Ilbert 2011), `FAST` (Kriek *et al.* 2009) and four more codes developed by the teams based on χ^2 fitting method. TEST-1 is based on a set of 13 filters consisting of U-band (VIMOS), optical- $F435W$, $F606W$, $F775W$, $F850LP$ (ACS), near-infrared- $F105W$, $F125W$, $F160W$ (WFC3), HawkI K-band (VLT) and *Spitzer*/IRAC- $3.6, 4.5, 5.8$ and 8μm, for galaxies with $S/N > 5$ selected in the H-band, detected with $S/N > 1$ in at least six passbands in a redshift range $0 < z < 4$. TEST-2 investigated the sensitivity of the stellar mass estimates to the free parameters, fitting simulated data for galaxies with more complex SFHs drawn from semi-analytic models. The catalogs based on these models contained 10,000 galaxies with known multi-waveband photometry, input mass, age, extinction and metallicity, and the SFHs were diverse, consisting of exponentially declining, constant and rising. Redshift distribution for galaxies in TEST-2 catalogue closely follow the photometric redshift distribution in the GOODS-S field. TEST-3 compared masses when the same fitting parameters and techniques, used in TEST-2, are applied to real galaxies. A total of 598 galaxies with photometric data from U-band (VIMOS), optical- $F435W, F606W, F775W, F850LP$ (ACS), near-infrared- $F098M, F105W, F125W, F160W$ (WFC3), K_s (VLT/ISAAC) and mid-infrared *Spitzer*/IRAC $3.6, 4.5, 5.8$ and 8μm selected in GOODS-S field (Guo *et al.* 2013) were used for this test. This test differs from the previous ones because the catalogue analyzed is based on observations only and not on simulated photometric catalogues. TEST-4 repeated TEST-3 using a shallower NIR data, in order to verify the effect of selection wavelength and near-infrared photometric depth on the stellar mass measurements.

As result no significant bias in $\Delta\log(\mathcal{M})$ was found among different codes, with all having comparable scatter, $\sigma(\Delta\log(\mathcal{M})) = 0.136$dex, and fainter galaxies with lower photometric S/N ratios ($H > 26$ mag) are responsible for most of this scatter. The median of stellar masses among different methods provides a stable measure of the mass associated with any given galaxy, $\sigma(\Delta\log(\mathcal{M})) = 0.142$dex. Furthermore, the $\Delta\log(\mathcal{M})$ values were found to be strongly correlated with deviations in age (defined as the difference between the estimated and expected values), with a weaker correlation with extinction. For any given method and extinction, there is an increase in the estimated stellar mass for ages $> 10^{8.5}$ years. The scatter in the estimated stellar masses due to free parameters (after fixing redshifts and IMF) are quantified as $\sigma(\Delta\log(\mathcal{M})) = 0.110$ dex, and the effects of population synthesis models and correction for nebular emission were found to change the stellar mass by 0.2 dex and 0.3 dex, respectively.

It is interesting to note that Mobasher *et al.* (2015) analysis agrees with other independent papers (Wuyts *et al.* 2009, Pforr *et al.* 2012), and finds that by fixing the physical parameters, specifically redshifts, the difference between the predicted and expected stellar masses increased. In other words, the variation of the redshift compensates for the mismatch between SFH, metallicity, age and dust. Therefore, our lack of knowledge of the correct SFH, combined with inherent degeneracy between age, dust and metallicity, are the main reasons for uncertainties in stellar masses.

Chapter 4

Stellar mass analysis in different cosmologies

> "Scientific research consists in seeing what everyone else has seen, but thinking what no one else has thought."
>
> *Albert Szent-Gyorgyi*

Chapter 3 dealt with the introduction of the technique to estimate stellar mass from photometric data, whereas Chapter 1 described two different cosmological models. Here I discuss the estimation of the stellar mass and its evolution in different cosmologies. First, the photometric data and the SED-fitting code used to derive the amount of mass in form of stars in galaxies are presented, followed by the discussion of results in different cosmologies. Then, based on these mass measurements, their cosmic time evolution will be obtained, as well as the galaxy stellar mass function for different cosmological models and galaxy types. The results presented in this Chapter are summarized in Lopes *et al.* (2016a)

4.1 Data description

In this section I shall describe the UVISTA survey, from which the galaxy sample was selected. Then further information about the multi-wavelength catalogue will be added.

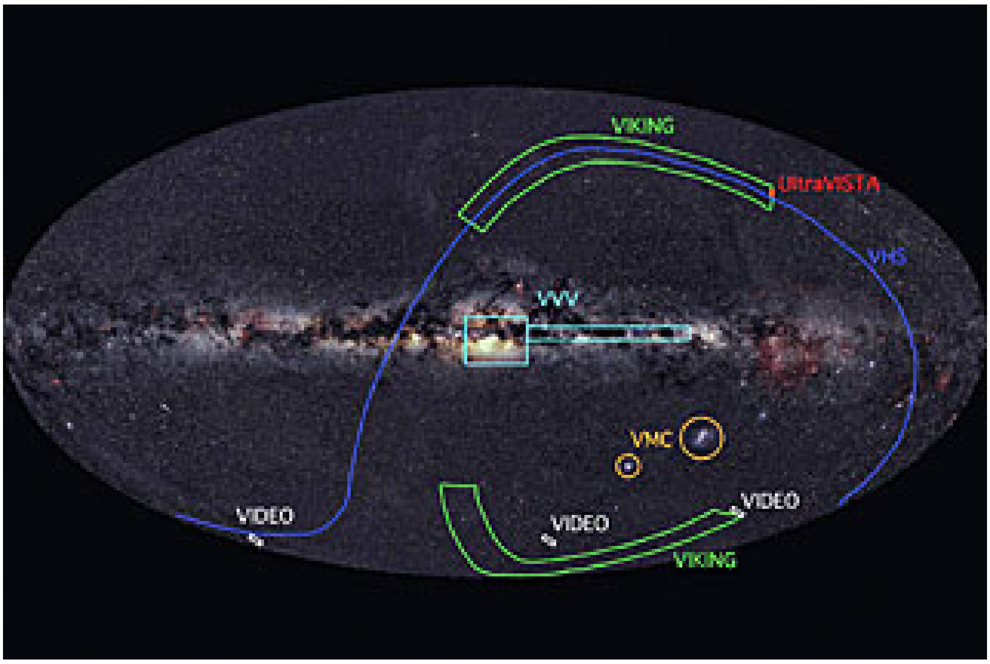

Figure 4.1: A schematic representation of the sky coverage of the various VISTA surveys. The image is a projection of the entire sky with the Milky Way across the centre. (Credit: VISTA/ESO).

4.1.1 UVISTA survey

The Visible and Infrared Survey Telescope for Astronomy, mostly known as VISTA, is a telescope located at ESO's Cerro Paranal Observatory in Chile. It is a 4-meter telescope specifically designed to perform wide-area near infrared surveys and equipped with a large-format array camera, the Vista InfraRed CAMera "VIRCAM". There are six large public surveys conducted by VISTA, among which UVISTA is the deepest and narrowest one. UVISTA images one patch of sky over and over again, with the primary goals of studying the first galaxies, understanding the stellar mass build-up during the peak epoch of star formation activity and dust-obscured star formation. Fig. 4.1 shows a representation of the various VISTA surveys in a projection of the sky with the Milky Way in the center, note that UVISTA, in red, covers a very narrow region of the sky.

The UVISTA survey covers an effective area of 1.5 deg^2 centred on the COSMOS field, the location of the largest optical mosaic obtained with the Hubble Space Telescope (Scoville *et al.* 2007; Koekemoer *et al.* 2007), and also an area of continuous observations by many deep ground-based astronomical facilities. Fig. 4.2 illustrates some regions of the field covered by UVISTA.

Figure 4.2: This view shows some highlights from UVISTA, with a total effective exposure time of 55 hours. It was created by combining more than 6000 individual images of the COSMOS field (Credit: ESO/UltraVISTA team).

The UVISTA survey comprises three separate components: a wide, deep survey with a continuous field covering of about 1.5 deg^2; an ultra-deep survey which consists of deeper strips covering ~ 0.7 deg^2; and an ultra-deep narrow-band survey targeting emission-line galaxies at a given range of redshifts. In this work, it was only used the first (deep) survey summarized in the first UVISTA DR1 data release (McCracken *et al.* 2012). The observations were made between 5th December 2009 and the 19th of April 2010 using four NIR bands, Y, J, H and K_S, seen in Fig. 4.3. Details about the observations and data reduction are described in McCracken *et al.* (2012).

4.1.2 Multi-wavelength catalogue

The multi-wavelength catalogue is fully described in Ilbert *et al.* (2013). It uses observations from 29 bands taken on ground-based facilities, VISTA ($1.02-2.15$ μm), Subaru ($4200-9000$ Å) and Canada-France-Hawaii Telescope "CFHT" ($3900-21500$ Å), and space telescopes, *Spitzer* ($3.6-8$ μm) and GALEX ($1500-2300$ Å). The effective wavelength and the equivalent width, also known as the full width at half maximum (FWHM), of each filter are listed in Table 4.1. Next, it is briefly presented the datasets used in this work.

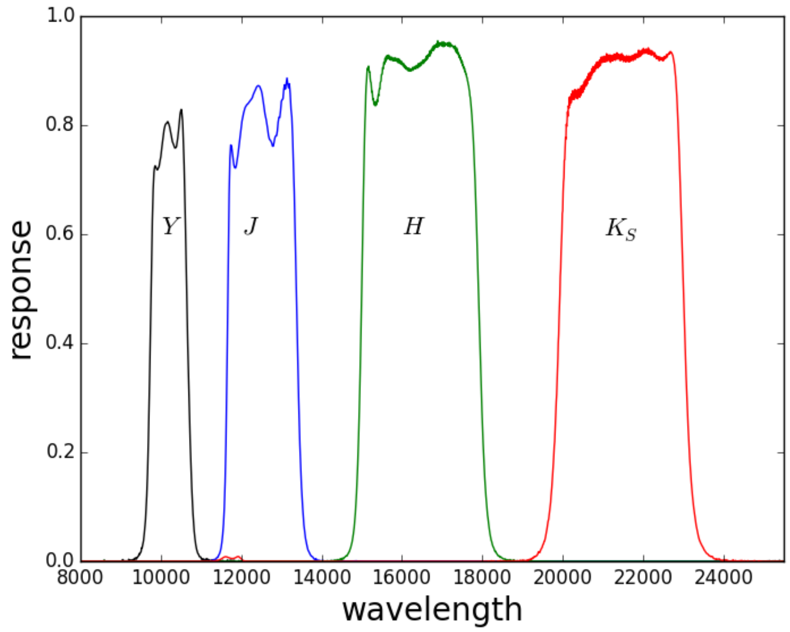

Figure 4.3: Response curves of the four near-infrared bands in UVISTA.

- **Ultraviolet (UV):** The NUV band were based on GALEX data (Zamojski *et al.* 2007), in which the fluxes were calculated using point spread function fitting method and the limiting magnitude ~ 25.7 mag. While u^* band data were obtained at the 3.6m CFHT and reach a depth of ~ 26.5 mag.

- **Optical:** The broad and intermediate-band data were taken by the SUPRIME camera on the 8.2-meter Subaru Telescope located at the summit of Mauna Kea, Hawaii. A complete description of the observations, data reduction and photometry catalogue are discussed in Capak *et al.* (2007). The list of the bands is as follows: B_J, V_J, r^+, i^+, z^+, $IA427$, $IA464$, $IA484$, $IA505$, $IA527$, $IA574$, $IA624$, $IA679$, $IA709$, $IA738$, $IA767$, $IA827$, $NB711$, $NB816$.

- **NIR:** The four UVISTA band data have the following limiting magnitude $Y \sim 24.6$, $J \sim 24.4$, $H \sim 23.9$ and $K_s \sim 23.7$.

- **Mid- IR:** The IRAC camera on the *Spitzer* made measurements of the COSMOS field in four bands, $3.6\mu m, 4.5\mu m, 5.6\mu m$ and $8.0\mu m$, as part of the S-COSMOS survey (Sanders *et al.* 2007). For the present work, it was used the IRAC selected catalogue made by Ilbert *et al.* (2010).

Table 4.1: Effective wavelength and width for the bands in the UVISTA catalogue.

Filter	Telescope	Effective λ (Å)	FWHM (Å)
NUV	GALEX	2306.5	789.1
u^*	CFHT	3911.0	538.0
B_J	Subaru	4439.6	806.7
V_J	Subaru	5448.9	934.8
r^+	Subaru	6231.8	1348.8
i^+	Subaru	7629.1	1489.4
z^+	Subaru	9021.6	955.3
Y	VISTA	10200	1000
J	VISTA	12500	1800
H	VISTA	16500	3000
K_S	VISTA	21500	3000
$IRAC1$	*Spitzer*	35262.5	7412.0
$IRAC2$	*Spitzer*	44606.7	10113.0
$IRAC3$	*Spitzer*	56764.4	13499.0
$IRAC4$	*Spitzer*	77030.1	28397.0
$IA427$	Subaru	4256.3	206.5
$IA464$	Subaru	4633.3	218.0
$IA484$	Subaru	4845.9	228.5
$IA505$	Subaru	5060.7	230.5
$IA527$	Subaru	5258.9	242.0
$IA574$	Subaru	5762.1	271.5
$IA624$	Subaru	6230.0	300.5
$IA679$	Subaru	6778.8	336.0
$IA709$	Subaru	7070.7	315.5
$IA738$	Subaru	7358.7	323.5
$IA767$	Subaru	7681.2	364.0
$IA827$	Subaru	8240.9	343.5
$NB711$	Subaru	7119.6	72.5
$NB816$	Subaru	8149.0	119.5

From these data it was select only sources at $K_S < 24$ with good image quality, in an effective area of 1.5 deg^2.

The photometric redshifts, photo-z, of the detected sources were obtained by Ilbert *et al.* (2013) using the public code "photometric analysis for redshift estimate" (hereafter, `Le Phare`; Arnouts *et al.* 1999; Ilbert *et al.* 2006), which follows the SED-fitting procedure discussed in Chapter 3. They used 31 templates including elliptical and spiral galaxy templates from Polletta *et al.* (2007) library, 12 templates of young and blue star-forming galaxies with Bruzual & Charlot SPS models (2003), and 2 new templates of ellipticals generated with Bruzual & Charlot (2003) to improve the photo-z for quiescent galaxies at $z > 1.5$. The extinction is a free parameter and several extinction laws were considered (Calzetti *et al.* 2000; Prevot *et al.* 1984 and a modified version of Calzetti laws with a bump at 2175 Å). Emission lines were included using an empirical relation between the UV light and the emission line fluxes (Ilbert *et al.* 2009). The photo-z were calculated by using the median of the marginalised probability distribution function. Moreover, the accuracy of these results were tested against several spectroscopic samples, and it was found that at $i^+_{AB} < 22.5(z_{med} \sim 0.5)$, the precision is 1% with less than 1% of catastrophic failures, while at $z > 1.5$ the precision of the photo-z is 3% for $i^+_{med} \sim 24$.

The final dataset consists of about 220,000 galaxies with $K_s < 24$ in $0.2 < z < 4.0$ range, and photometric information in 29 bands, which includes NUV, optical and infrared regimes, and redshift. Details can be found in Ilbert *et al.* (2013).

4.1.3 Galaxy classification

Following Ilbert *et al.* (2013) the sample was divided in "red", also called "quiescent", and "blue", also referred as "star-forming" galaxies. For this separation, it was considered the rest-frame colour selection based on NUV$-r^+$ versus $r^+ - J$. The galaxies classified as quiescent have $M_{NUV} - M_r > 3(M_r - M_J) + 1$ and $M_{NUV} - M_r > 3.1$, these relations are related to the fact that the extinction moves star-forming galaxies along the diagonal axes from bottom left to top right. This classification avoids a mix between dusty blue galaxies and red galaxies.Note that this criterion is applied to the analysis of both standard and void-LTB cosmologies. As an example, Fig. 4.4 shows the classification in the OCGBH model. However the classification is the same in all cosmologies.

4.2 Stellar mass estimation

The stellar mass was estimated using the `Le Phare` code. Next, I shall describe how this code works to estimate the galaxy physical properties and which changes had to be made to allow estimates in different cosmologies. Then, I will outline the input parameters used to derive the masses and present the results as well as their respective discussions.

4.2.1 Le Phare

To convert the observational data from light to stellar mass I rely on `Le Phare` code. This package computes physical properties from galaxies applying a SED-fitting method. First, the procedure generates a synthetic spectral library based on a set of assumptions, such as stellar population synthesis models, filters, extinction law and cosmology. Then a template fitting analysis is made between this library and a multi-wavelength catalogue. In other words, for each galaxy

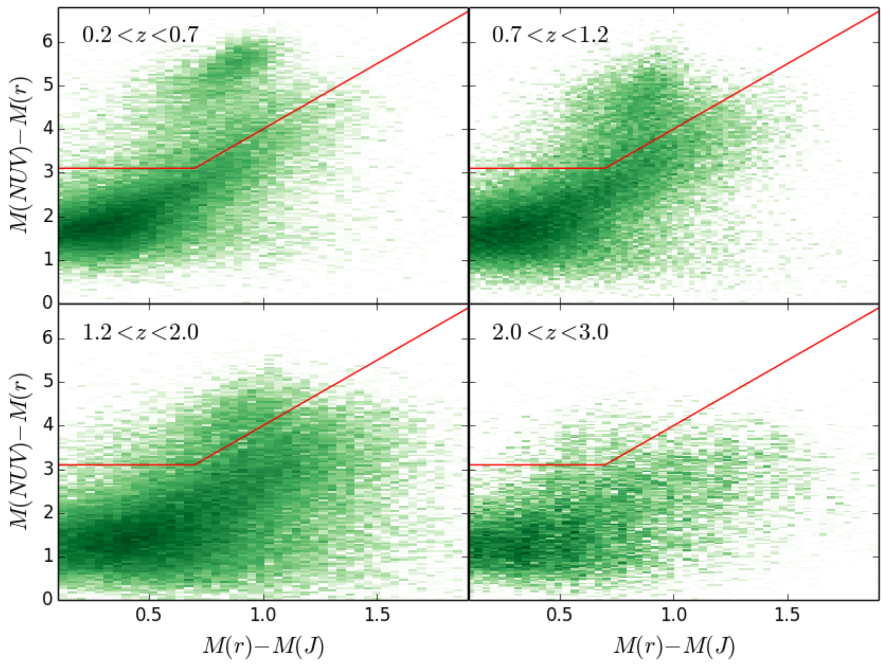

Figure 4.4: Two-colour classification of red and blue populations in the OCGBH model. The galaxies above the red line in the top left are selected as quiescent and the ones below the red line are the star-forming.

in the dataset with a known redshift it is fitted the synthetic library to its photometric measurements. The result is a best-fitting SED for each source with the information about its physical properties.

As already mentioned, one of the priors to estimate the stellar mass is the cosmological model. In `Le Phare` the established cosmology is the standard model and only the values of its parameters are allowed to change. However, if one wants to obtain the galaxy properties adopting an alternative cosmology, e.g., non-homogeneous models, modified gravity, etc, it is necessary to modify the code.

For an analysis of the luminosity (or luminosity function) in a different cosmological model, a change on the SED-fitting code would be unnecessary, and a simple relation between the luminosity in the standard model and the square of the ratio between the distances in the standard and alternative model is enough, as introduced by Iribarrem *et al.* (2013). However, when dealing with stellar masses an additional effect related to the $\mathcal{M}/L$ must be considered. The stellar mass-to-light ratio is a function of the star formation history, thus related to the time, a cosmology dependent quantity. Another way of understanding how the time affects the SED-fitting results is through the age of the galaxies. At a given z, the SED fitting puts a prior to the age of the galaxies being necessarily less than the age of the Universe. Nevertheless as shown in Fig. 1.4, the age of the Universe in the LTB model, for both CGBH and OCGBH parametrizations, is always smaller than the one in the ΛCDM, resulting in galaxies, analyzed by the latter model, with ages bigger than the age of the Universe in the alternative models. An example of this effect can be seen in Fig. 4.5, where the ages of the galaxies calculated using the "unchanged" version of `Le Phare` are compare with the age of Universe in the OCGBH model. In order to guarantee the consistency on the output of the SED-fitting analysis, I modified the function related to the cosmological time, replacing the standard model equations for time with commands that read a table with z and t, and associate the t-values and a to the galaxy input z. Because of the prior on the age of the Universe, this modification causes a change in the number of available synthetic SEDs. I also made a similar change for luminosity distance commands.

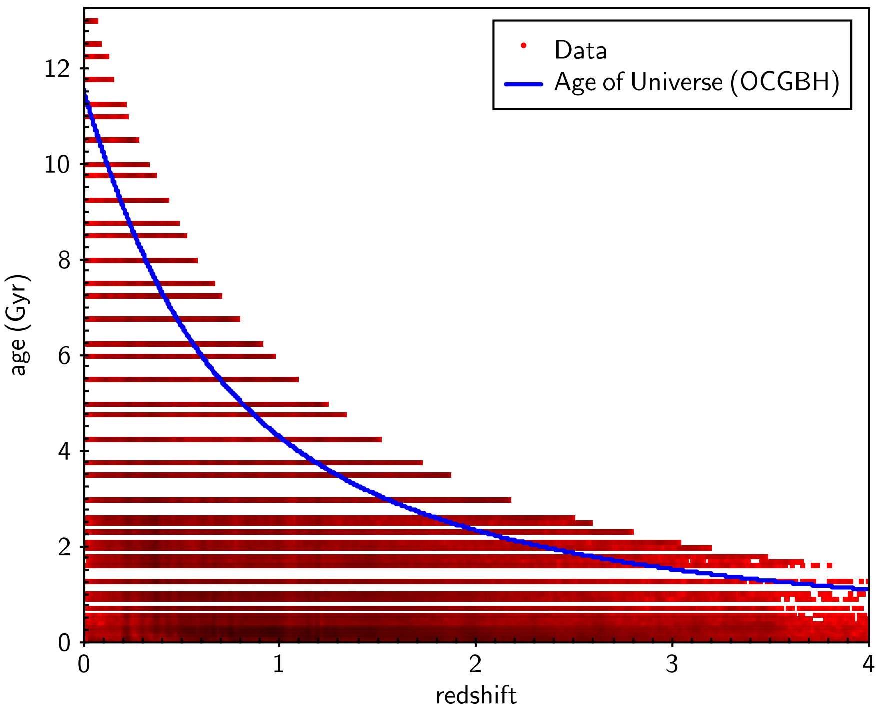

Figure 4.5: Age of the galaxies in standard model vs. redshift. This test was done using the ages derived by Ilbert *et al.* (2013). In this plot the darker regions corresponds to a higher number of galaxies. It can be seen, most of the galaxies are below the age of the Universe on OCGBH (blue solid line) and would not be affected by a change of the cosmological time. On the other hand, the ones above the blue line would no exist in the OCGBH model.

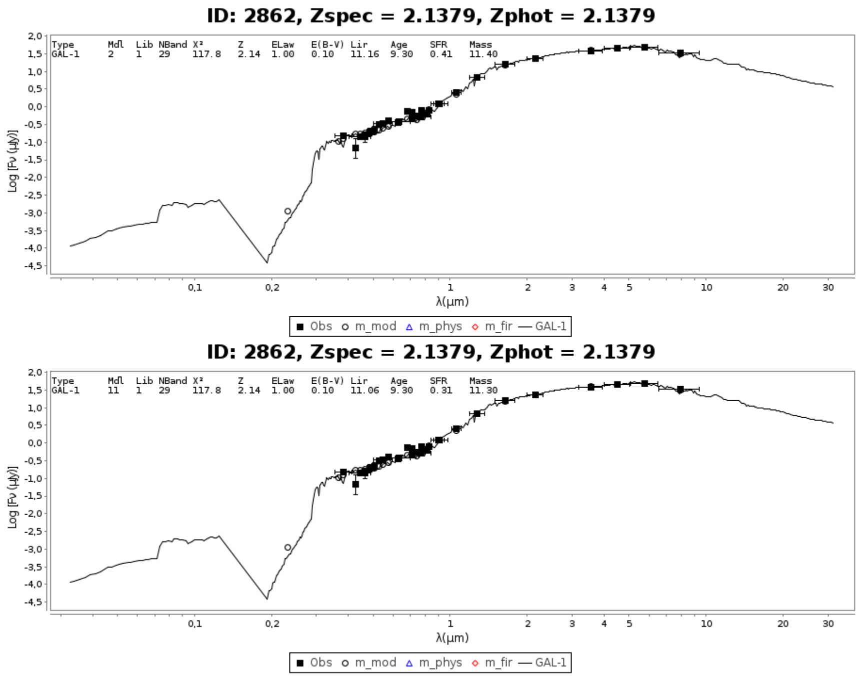

Figure 4.6: Best-fit SED for galaxy ID 2862 from UVISTA catalog assuming standard (*top panel*) and OCGBH (*bottom panel*) models.

Fig. 4.6 shows an example of the best-fit SED from modified version `Le Phare` assuming ΛCDM and OCGBH models. This galaxy is one of many sources in the sample that has the same age and only varies the mass (and the luminosity), once the cosmology changes. It can be noted that the mass varies 0.1 dex from one cosmology to the other, which agrees with a variation only on d_L (see Fig. 1.5).

4.2.2 Stellar mass results

Once the modified version of `Le Phare` is ready, the stellar mass for all the cosmological models can be derived. The library of synthetic spectra is generated using the following set of assumptions: the SPS model of Bruzual & Charlot (2003); the Calzetti *et al.* (2000) extinction law; three metallicities ($Z = 0.004, 0.008, 0.02 Z_\odot$, i.e., in units of solar metallicity); a star formation history that falls exponentially, $SFR \propto \tau^{-1}\exp(-t/\tau)$, with nine possible values for τ from 0.1 Gyr to 30 Gyr; the extinction $E(B-V)$ ranges from 0 to 0.5, with an imposed prior of $E(B-V) < 0.15$ if $age/\tau > 4$ (Fontana *et al.* 2006; Pozzetti *et al.* 2007; Ilbert *et al.* 2010, 2013). These parameters remain the same for all cosmologies. The differences among the stellar masses in different cosmological models is defined by,

$$\Delta \log \mathcal{M}_{stellar} = \log \mathcal{M}_{stellar}^{\Lambda CDM} - \log \mathcal{M}_{stellar}^{LTB}, \tag{4.1}$$

where the LTB index stands for both CGBH or OCGBH, as shown in Fig. 4.7.

As expected, the variation on the stellar mass for the LTB models compared with the ones for the standard model evolves with redshift: this variation reflecting the dependency of the luminosity distance and time with redshift. A quick correspondence between Figs. 1.5 and 4.7 allows us to identify the contribution of the luminosity distance in the stellar mass result. The region where most of the galaxies are located can be directly linked to the effect caused by the change on the luminosity distance. Then, this distance is the main responsible for the deviations on the stellar mass values in a cosmological perspective. Moreover, the spread in the stellar mass difference can be interpreted as a consequence of the cosmological time variation. These conclusions seem consistent with the fact that most of the objects in the UVISTA sample are not affected by a change of time scale, as can be seen in Fig. 4.5. In the end, the masses of these galaxies reflect the combination of the effects due to the two quantities resulting in the spread observed in Fig. 4.7. In percentages, the reduction on the stellar mass due to the luminosity distance varies from $\sim 1.15\%$ to $\sim 27.16\%$ for the OCGBH, while for CGBH varies from $\sim -11.12\%$ to 15.20% in the studied redshift range $0.2 < z < 4$. The negative values is related to $\mathcal{M}_{stellar}^{OCGBH} > \mathcal{M}_{stellar}^{\Lambda CDM}$ at $z < 1$. However, for a smaller number of galaxies the time variation can render mass values up to about $40-50\%$ shorter in the LTB models than the ones in ΛCDM ones.

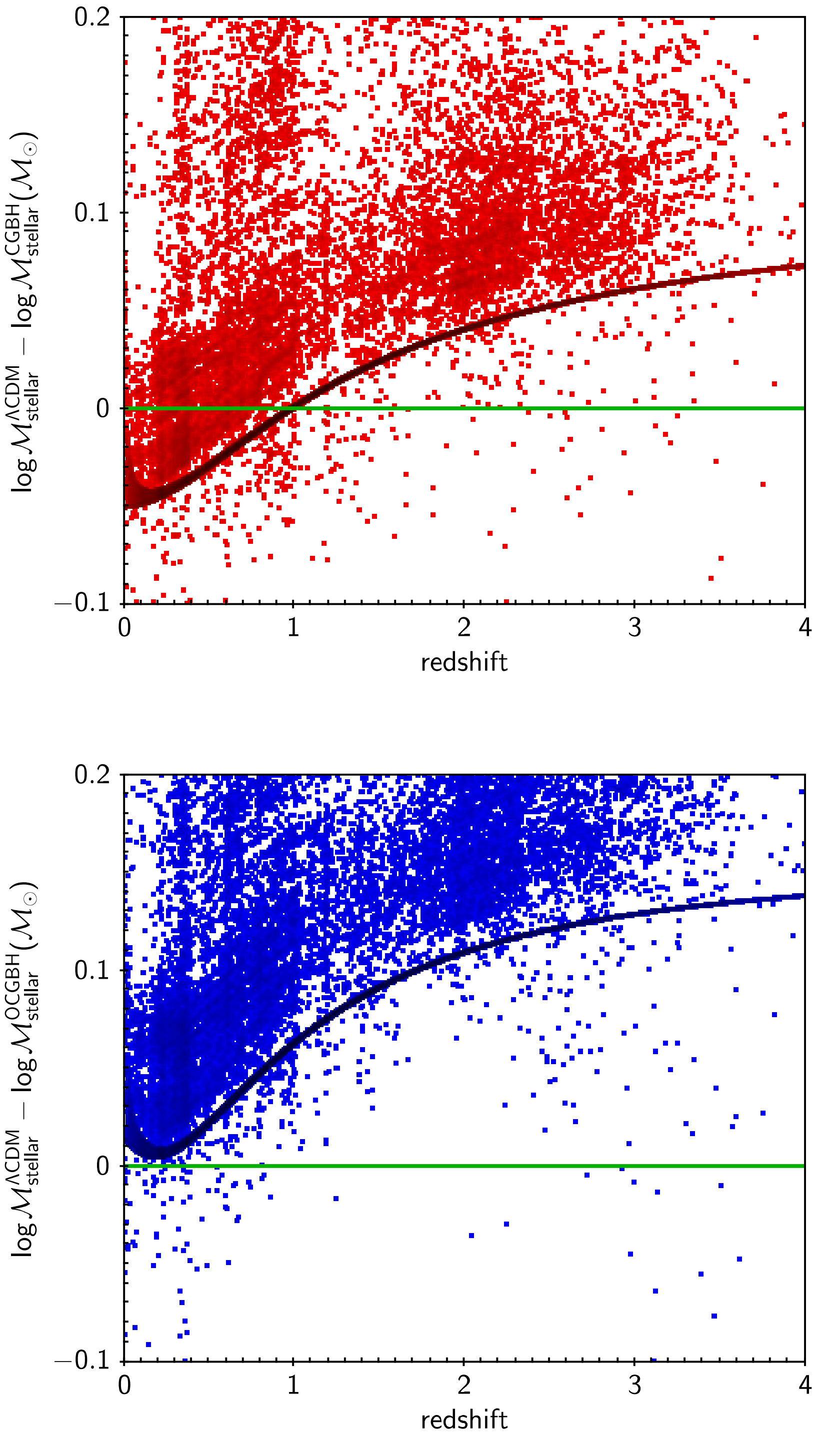

Figure 4.7: Comparison between the stellar masses from the CGBH (*top panel*) and the OCGBH (*bottom panel*) against the ΛCDM results vs. redshift. The green solid line simplifies the correlation with the Fig. 1.5, however no physical meaning must be assigned to this line. The darker region almost simulating a thick line is where most of the galaxies are located. Note that this plot is a product of the output from *Le Phare*, so no completeness cut was applied.

4.3 Galaxy stellar mass function

4.3.1 $1/V_{max}$ method

I choose to calculate the GSMF using the classical $1/V_{max}$ formalism (Schmidt 1968), which is a non-parametric estimator, i.e., it does not assume the shape of the GSMF. In a given redshift interval (z_1, z_2), each object i has a maximum redshift $z_{max,i}$ and a minimum redshift $z_{min,i}$ at which a source would still be included in the survey, assuming the $K < 24$ selection. In this work the $z_{min,i}$ is considered as the lower limit of redshift bin, therefore $z_{min,i} = z_1$. Then, the mass function for each mass bin centered in $\mathcal{M}_j$ is computed as,

$$\phi(\mathcal{M}_j)\,\Delta\mathcal{M}_j = \sum_i^N \frac{1}{V_{max,i}}, \tag{4.2}$$

with

$$V_{max} = \int_{z_1}^{z_{max}=min(z_2, z_{max,i})} \Omega \frac{\mathrm{d}V(z)}{\mathrm{d}z} \mathrm{d}z, \tag{4.3}$$

where z_{max} is the minimum between the maximum redshift of the bin (z_2) and the maximum redshift at which the source will still be visible in a survey limited to $K = 24$ $(z_{max,i})$, N is the number of sources inside the mass bin and the redshift interval, Ω the area covered by the survey.

To calculate $z_{max,i}$, for each source with absolute magnitude M the following equation has to be solved,

$$M = 24 - 5\log d_L(z_{max,i}) - 25 - KC(z_{max}), \tag{4.4}$$

where KC is the k-correction. From this expression, it is clear that $z_{max,i}$ is related to the luminosity distance, which depends on the cosmology. Consequently, the $z_{max,i}$ might change with the cosmological model.

An essential factor to account for when deriving the GSMF is the mass limit $\mathcal{M}_{lim}$, i.e., the minimum mass at which all galaxies would be observed given the survey limit, $K_S \approx 24$. In other words, above this mass value the GSMF is considered to be complete. Following Pozzetti *et al.* (2010), for each source with mass $\mathcal{M}$ and apparent magnitude K the limiting mass is calculated as,

$$\log(\mathcal{M}_{lim}) = \log(\mathcal{M}) + 0.4(K - 24). \tag{4.5}$$

The distribution of this $\mathcal{M}_{lim}$ reflects the distribution of the mass-to-light ratio at each redshift. From this result, it is used the 20% faintest galaxies at each redshift, in order to avoid the influence of the brightest and reddest sources, to compute the stellar mass completeness limit $\mathcal{M}_{com}$ defined as the mass value at which 90% of the $\mathcal{M}_{lim}$ distribution lies below. It is important to note that this method differs slightly from the one adopted in Ilbert *et al.* (2013), in which the authors based their estimates of $\mathcal{M}_{lim}$ on the 90% most fitted templates from the SED-fitting analysis instead of the 20% faintest objects. This different procedure causes some discrepancies on the values of $\mathcal{M}_{com}$ from the standard model between the present work and Ilbert *et al.* (2013), principally in the first bin, $0.2 < z < 0.5$, where it is found a difference of 0.52 dex, in the other bins the differences drops to < 0.2 dex.

The steps to obtain $\mathcal{M}_{com}$ in ΛCDM and LTB models were the same. Fig. 4.8 shows an example of how the stellar mass completeness is computed for the ΛCDM. For comparison reasons, we also plot the $\mathcal{M}_{com}$ in the OCGBH model. From this plot, it is clear that the completeness mass in OCGBH becomes increasingly lower than in ΛCDM with the redshift. For CGBH, the same pattern is seen but the values of $\mathcal{M}_{com}$ are closer to the ones in the standard model.

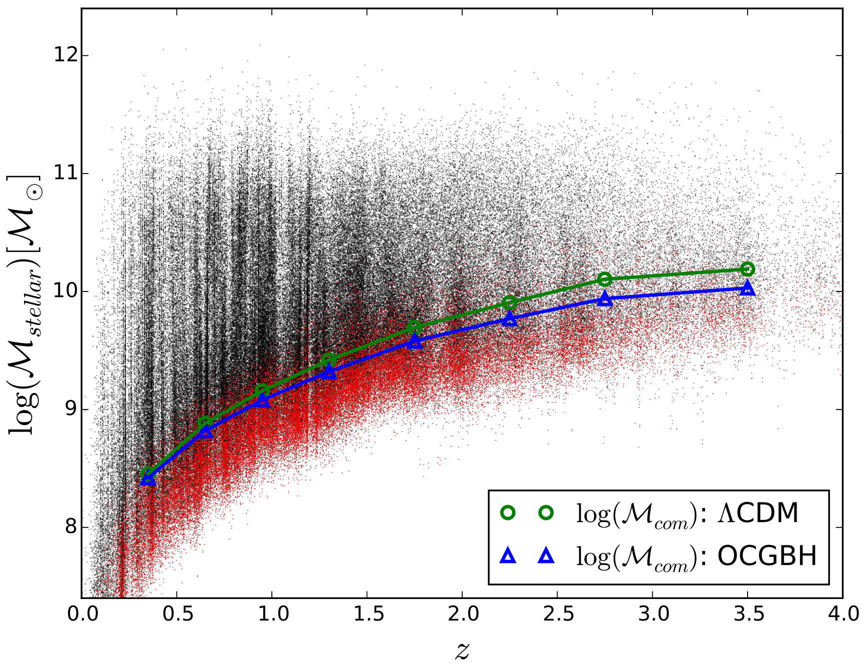

Figure 4.8: Stellar mass as function of the redshift for the K_S-band select galaxies based on UVISTA. The black points are the masses for the full sample while the red ones are the $\mathcal{M}_{lim}$ from the 20% faintest objects, both derived using the standard cosmology. The green circles and solid line represent the completeness mass limit $\mathcal{M}_{com}$ calculated for the standard model. It is also plotted the $\mathcal{M}_{com}$ from the OCGBH model, blue triangles and solid line.

The total uncertainties associated to the GSMF are calculated using a combination of errors due to the template-fitting procedure σ_{fit}, the galaxy cosmic variance σ_{cosm_var}, and Poissonian errors σ_{poiss}, given by

$$\sigma_{tot} = \sqrt{\sigma^2_{poiss} + \sigma^2_{fit} + \sigma^2_{cosm\_var}}. \tag{4.6}$$

The σ_{poiss} it is derived from Poissonian statistics based on the $1/V_{max}$ method,

$$\sigma^2_{poiss} = \left[\sum_i^N \frac{1}{V^2_{max,i}}\right]. \tag{4.7}$$

The cosmic variance accounts for the different properties observed when studying different regions of the sky, like the large scale structure. In the standard mode, it can be estimated using the public code `getcv` provided by Moster *et al.* (2011) which obtains the σ_{cosm_var} as

$$\sigma_{cosm\_var} = b\,\sigma_{DM}, \tag{4.8}$$

where b is the galaxy bias and σ_{DM} the dark matter variance related to the size of the observed field, 1.5 deg^2. The σ_{cosm_var} is compute as function of redshift and stellar mass bins, therefore it is directly related to the GSMF data points. For the LTB models the cosmic variance is assumed the same as in the standard model, which in practice is not exactly valid. However, since the difference in the GSMF between the different cosmologies is small, if the σ_{cosm_var} in LTB is bigger than the values used, the significance of the difference in the GSMF it would only be smaller, not causing a great impact in the conclusions found in this work.

For the σ_{fit} in the ΛCDM cosmology, I use the results presented in Ilbert et al. (2013). These values were based on a set of 30 mock catalogues which were created by perturbing each flux point according to its formal error measurements. Then, for each realization, the stellar masses and the GSMF are recomputed, and a 1σ dispersion of these results are obtained as function of mass and redshift, as shown in Fig. 4.9. It is straightforward to associate the curves in this plot to the GSMF data points. I choose to adopt the previously calculated σ_{fit} because I work with the same galaxy dataset and the same code to perform the SED-fitting as Ilber *et al.* (2013). For the LTB models, I assume that the relationship between the σ_{fit}, mass and redshift remains the same found in ΛCDM. As mentioned before the difference in the mass is small, so there is no reason to expect a major alteration in the σ_{fit}.

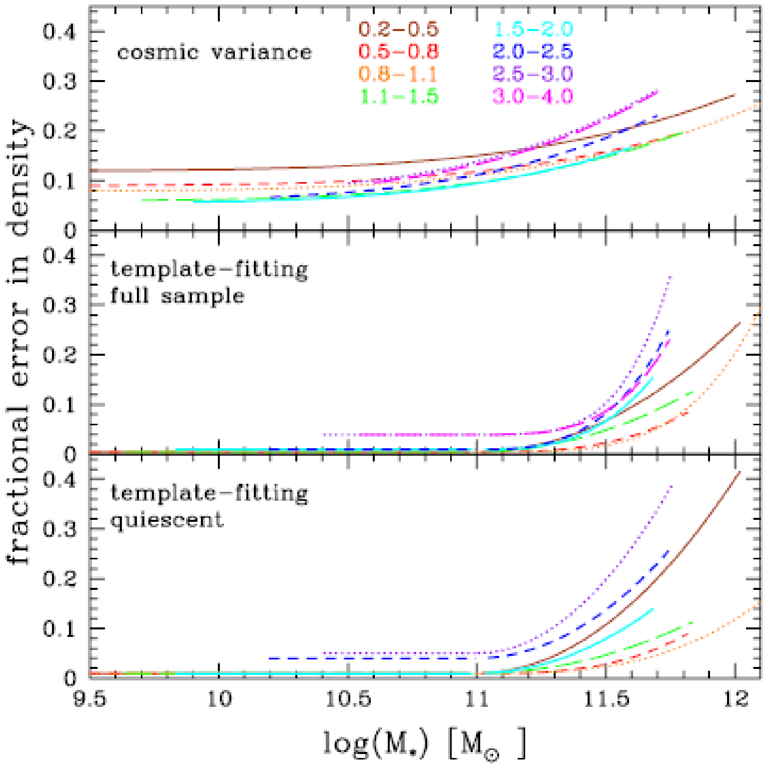

Figure 4.9: Fractional error as a function of the stellar mass and redshift. The top panel shows the errors due to the cosmic variance, while the middle and bottom panels are the errors associated to the template fitting procedure for the full sample and the quiescent population, respectively. Results are shown only in the mass range covered by our dataset. (Ilbert *et al.* 2013)

4.4 Discussion of results

In order to obtain a parametric form based on the $1/V_{max}$ results, the data points are fitted by a double Schechter form described as,

$$\phi(\mathcal{M})\mathrm{d}\mathcal{M} = e^{-\frac{\mathcal{M}}{\mathcal{M}^*}}\left[\phi_1^*\left(\frac{\mathcal{M}}{\mathcal{M}^*}\right)^{\alpha_1} + \phi_2^*\left(\frac{\mathcal{M}}{\mathcal{M}^*}\right)^{\alpha_2}\right]\frac{\mathrm{d}\mathcal{M}}{\mathcal{M}^*}, \tag{4.9}$$

where $\mathcal{M}^*$ is the characteristic mass, α_1 an α_2 are the slopes in which $\alpha_2 < \alpha_1$, and ϕ_1^* and ϕ_2^* are the GSMF normalization parameters. Following Ilbert *et al.* (2013), for the full sample and blue population it is arbitrarily adopted $\alpha = -1.6$ at $z > 1.5$ in all cosmologies since this parameter is no longer well constrained at this regime. This value is derived in the lower redshift bin, where the data is enough to constrain it. For the red galaxies, a simple Schechter form given by

$$\phi(\mathcal{M})\mathrm{d}\mathcal{M} = \exp\left(-\frac{\mathcal{M}}{\mathcal{M}^*}\right)\phi_1^*\left(\frac{\mathcal{M}}{\mathcal{M}^*}\right)^{\alpha_1}\frac{\mathrm{d}\mathcal{M}}{\mathcal{M}^*} \tag{4.10}$$

is fitted to the data at $z > 0.5$, since there is not a upturn at low-mass. A double Schechter is only used in the first bin, $0.2 < z < 0.5$.

4.4.1 Full sample

The best-fit parameters for the full sample in the standard and LTB models are given in Table 4.2, along with the stellar mass completeness $\mathcal{M}_{com}$ for the eight z-bins. Note that all best-fit results described in this section are obtained using a procedure different from that considered by Ilbert *et al.* (2013), in which the authors also account for Eddington bias. For this reason our results in ΛCDM compared with those of Ilbert et al. (2013) present a few discrepancies.

Table 4.2: Best-fit parameters for double-Schechter function for the full galaxy sample adopting three different cosmologies.

ΛCDM model						
z-bin	$\log(\mathcal{M}_{com})$ ($\mathcal{M}_\odot$)	$\log(\mathcal{M}^*)$ ($\mathcal{M}_\odot$)	ϕ_1^* (10^{-3} Mpc^{-3})	α_1	ϕ_2^* (10^{-3} Mpc^{-3})	α_2
0.2-0.5	8.45	10.91 ± 0.07	1.55 ± 0.57	-1.08 ± 0.24	0.53 ± 0.35	-1.43 ± 0.08
0.5-0.8	8.88	11.00 ± 0.06	1.18 ± 0.38	-1.11 ± 0.20	0.13 ± 0.24	-1.63 ± 0.26
0.8-1.1	9.16	10.87 ± 0.08	1.87 ± 0.46	-0.76 ± 0.40	0.24 ± 0.48	-1.62 ± 0.33
1.1-1.5	9.42	10.68 ± 0.09	1.39 ± 0.36	-0.28 ± 0.45	0.60 ± 0.45	-1.47 ± 0.18
1.5-2.0	9.69	10.70 ± 0.11	0.86 ± 0.19	-0.36 ± 0.52	0.34 ± 0.14	-1.6
2.0-2.5	9.91	10.71 ± 0.08	0.63 ± 0.11	-0.23 ± 0.49	0.15 ± 0.08	-1.6
2.5-3.0	10.10	10.81 ± 0.09	0.18 ± 0.08	-0.15 ± 0.34	0.13 ± 0.03	-1.6
3.0-4.0	10.19	10.78 ± 0.45	0.02 ± 0.03	0.48 ± 1.05	0.08 ± 0.09	-1.6
CGBH model						
z-bin	$\log(\mathcal{M}_{com})$ ($\mathcal{M}_\odot$)	$\log(\mathcal{M}^*)$ ($\mathcal{M}_\odot$)	ϕ_1^* (10^{-3} Mpc^{-3})	α_1	ϕ_2^* (10^{-3} Mpc^{-3})	α_2
0.2-0.5	8.47	10.85 ± 0.08	1.89 ± 0.66	-0.84 ± 0.25	0.63 ± 0.38	-1.42 ± 0.09
0.5-0.8	8.88	10.90 ± 0.07	1.64 ± 0.49	-0.90 ± 0.24	0.21 ± 0.24	-1.64 ± 0.20
0.8-1.1	9.15	10.86 ± 0.05	1.89 ± 0.35	-0.84 ± 0.15	0.25 ± 0.17	-1.61 ± 0.14
1.1-1.5	9.39	10.62 ± 0.10	1.67 ± 0.38	-0.43 ± 0.53	0.75 ± 0.37	-1.46 ± 0.21
1.5-2.0	9.65	10.62 ± 0.09	1.22 ± 0.22	-0.26 ± 0.47	0.49 ± 0.17	-1.6
2.0-2.5	9.84	10.65 ± 0.07	0.89 ± 0.15	-0.31 ± 0.47	0.19 ± 0.12	-1.6
2.5-3.0	10.02	10.72 ± 0.12	0.28 ± 0.13	-0.25 ± 0.89	0.18 ± 0.14	-1.6
3.0-4.0	10.10	10.68 ± 0.30	0.04 ± 0.03	0.40 ± 2.41	0.12 ± 0.11	-1.6
OCGBH model						
z-bin	$\log(\mathcal{M}_{com})$ ($\mathcal{M}_\odot$)	$\log(\mathcal{M}^*)$ ($\mathcal{M}_\odot$)	ϕ_1^* (10^{-3} Mpc^{-3})	α_1	ϕ_2^* (10^{-3} Mpc^{-3})	α_2
0.2-0.5	8.42	10.77 ± 0.10	2.88 ± 0.50	-0.74 ± 0.18	0.78 ± 0.37	-1.44 ± 0.10
0.5-0.8	8.82	10.84 ± 0.07	2.04 ± 0.61	-0.90 ± 0.24	0.25 ± 0.31	-1.64 ± 0.20
0.8-1.1	9.08	10.77 ± 0.05	2.53 ± 0.45	-0.80 ± 0.16	0.34 ± 0.23	-1.61 ± 0.14
1.1-1.5	9.32	10.52 ± 0.07	2.26 ± 0.34	-0.34 ± 0.31	0.98 ± 0.21	-1.47 ± 0.27
1.5-2.0	9.58	10.54 ± 0.06	1.56 ± 0.17	-0.24 ± 0.28	0.64 ± 0.23	-1.6
2.0-2.5	9.77	10.55 ± 0.06	1.14 ± 0.18	-0.19 ± 0.43	0.27 ± 0.14	-1.6
2.5-3.0	9.94	10.60 ± 0.15	0.34 ± 0.13	-0.06 ± 0.82	0.28 ± 0.20	-1.6
3.0-4.0	10.03	10.63 ± 0.21	0.04 ± 0.02	0.37 ± 1.24	0.14 ± 0.09	-1.6

For the full sample in the three cosmological models, it is found that the GSMF evolution is strongly mass-dependent, with the low-mass sources evolving more rapidly than the high mass ones, as can be seen in Fig. 4.10. Therefore, the global conclusions obtained in the standard model remain valid in the void-LTB models.

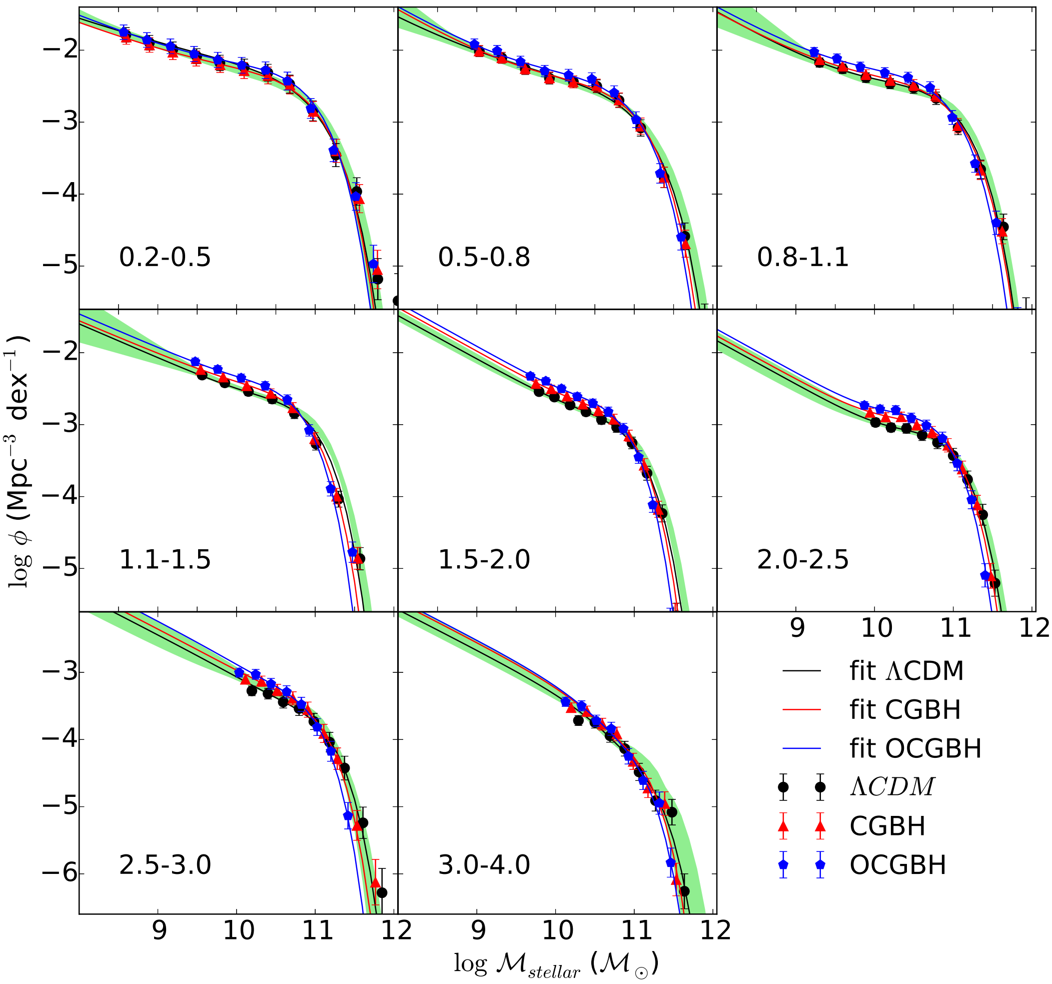

Figure 4.10: Galaxy stellar mass function for the full galaxy sample in the standard (ΛCDM) and LTB-void (CGBH, OCGBH) models. Each panel corresponds to a redshift bin. The green area represents the best-fit from Ilbert *et al.* (2013) based on the same 220,000 K-select galaxies from UVISTA and assuming the standard model. The solid lines are the best-fit for each model, and the symbols are as in the legend. (Lopes *et al.* 2016a)

The differences between the best-fit parameters from the double-Schechter function of the standard and LTB models can be evaluated using $\Delta X/\delta(\Delta X)$, where

$$\Delta X = X^{\Lambda CDM} - X^{LTB}, \tag{4.11}$$

$$\delta(\Delta X) = \sqrt{(\delta X^{\Lambda CDM})^2 + (\delta X^{LTB})^2}, \tag{4.12}$$

and X can be replaced by any of the double Schechter parameters (values reported in Table 4.2). Here it follows the description of the results of this analysis for each parameter: for $\mathcal{M}^*$, it is found that with the exception of the last z-bin, the significance level of the $\Delta\mathcal{M}^*$ varies from 1σ to 1.73σ for OCGBH, while for CGBH it is always less than 1σ. For ϕ_1^*, the variation is from 1σ to 2.52σ

if we consider OCGBH, while for CGBH it gets up to $1.22 - 1.42\sigma$ only between $1.5 < z < 2.5$ (for all the other bins it is $< 1\sigma$). For ϕ_2^*, the difference is $< 1\sigma$ for both CGBH and OCGBH in all z-bins, with the only exception of $\sim 1\sigma$ variations in the ranges $1.5 < z < 2.0$ and $2.5 < z < 3.0$ for the latter model. $\Delta\alpha_1$ never reaches 1σ in all both models and z-bins, with the exception of the first z-bin in OCGBH where it reaches 1.13σ. $\Delta\alpha_2$ is really small with an average of 0.03σ in both models. To summarize, α_1, α_2 and ϕ_2^*, on average, do not exhibit significant variations, while $\mathcal{M}^*$ and ϕ_1^* are more affected by different cosmologies.

An interpretation of the differences found in the GSMF is given by the distinct redshift relationships of the luminosity distance and the time from the different cosmologies that causes a $\Delta \log \mathcal{M}_{stellar}$, which can result in different sources in each mass bin. Besides, the comoving volume combined with the z_{max} values in different cosmologies can lead to different $1/V_{max}$, even for galaxies remaining within the same mass bin even after the change of cosmology. In Fig. 4.11, we show the redshift evolution of the double-Schechter parameters.

Assuming that these parameters evolve with z as,

$$\phi_1^*(z) = A_1(1+z)^{B_1}, \tag{4.13}$$

$$\phi_2^*(z) = A_2(1+z)^{B_2}, \tag{4.14}$$

$$\log[\mathcal{M}^*(z)] = A_3 + B_3 \ln(1+z), \tag{4.15}$$

$$\alpha_1(z) = A_4 + A_4 \ln(1+z), \tag{4.16}$$

$$\alpha_2(z) = A_5 + B_5 \ln(1+z), \tag{4.17}$$

where A_i and B_i are the evolution parameters with their values definied at $z = 0$, where each number is related to one of the double-Schechter parameters ($i = 1, 2, 3, 4, 5$). To derive the best-fitting parameters from Eqs. (4.13)-(4.17), it is applied the least square criterium. The uncertainties for each evolutionary parameter are obtained from the square root of the diagonal element of the covariance matrix of the fit. The best-fitting values of the evolution parameters in each cosmology are listed in Table 4.3, and no significant differences are found in the void-LTB models with respect to the standard one.

4.4.2 Blue and red populations

As additional test for different cosmologies effects, we have considered the galaxy population divided in two different classes: the red and the blue ones, defined

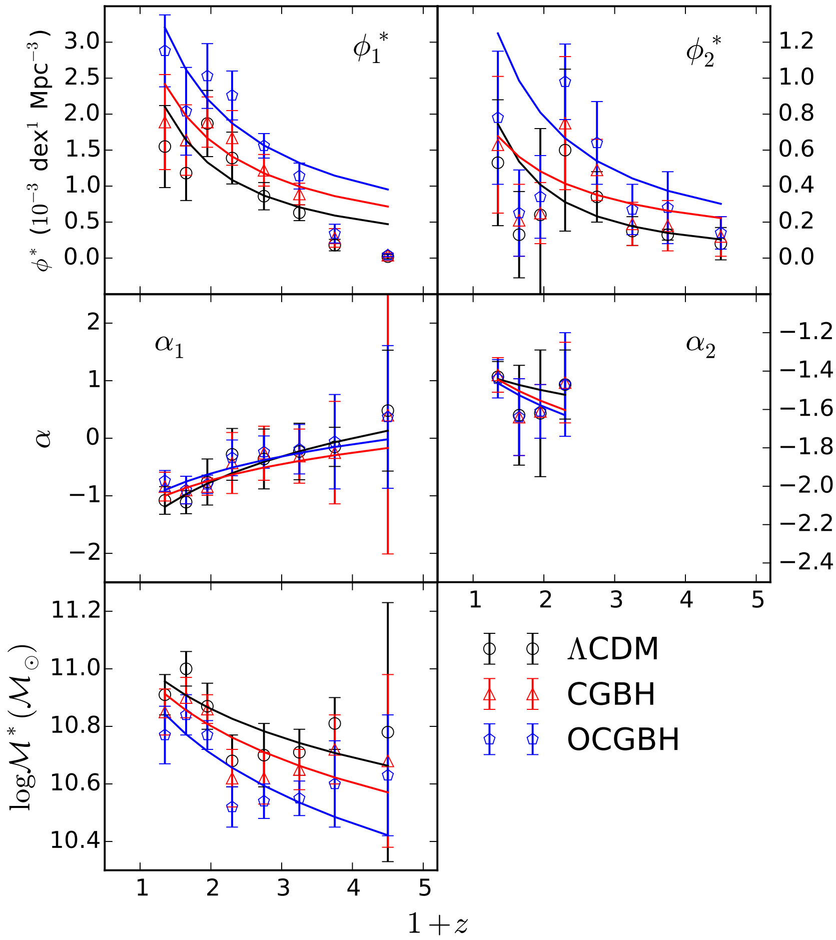

Figure 4.11: Redshift evolution of 5 parameters from the double-Schechter function: $\phi{*}_1, \phi_2^*, \alpha_1, \alpha_2$ and $\log \mathcal{M}^*$ according to Eq. 4.9. Note that α_2 only has four points, because after $z = 2$ this parameter is no longer well-constrained and its value is fixed to -1.6.

as described in Section 4.1.3. The evolution of the GSMF for the red an blue galaxies in both standard and void-LTB model are shown in Fig. 4.12.

In agreement with Ilbert *et al.* (2013), for the blue population in the standard model we found two regimes of GSMF: above and below $< 10^{10.7-10.9}\mathcal{M}_\odot$. At low-masses, we find a strong evolution in density with the faint-end slope remaining steep over the full redshift range, whereas for the most massive galaxies $10^{11.6-11.8}$ no evolution in density is detected. For the red population, the GSMF evolution is mass-dependent at $z < 1$, as we find no significant evolution of the high-mass end and a flattening of the faint-end slope. Until $z \sim 1.1$, the density of galaxies with $\mathcal{M}_{stellar} > 10^{11}\mathcal{M}_\odot$ does not increase, while galaxies are "quenched" at the low-mass end. At $1 < z < 3$, the evolution is no longer mass dependent and all red galaxies show an increase in density. Therefore, at $z > 1$

Table 4.3: Double-Schechter evolution parameter in the ΛCDM and LTB models.

Parameter	Model	A	B
	ΛCDM	0.003 ± 0.002	-1.2 ± 0.3
ϕ_1^*	CGBH	0.003 ± 0.002	-1.0 ± 0.3
	OCGBH	0.004 ± 0.002	-1.0 ± 0.2
	ΛCDM	0.001 ± 0.002	-1.6 ± 0.7
ϕ_2^*	CGBH	0.0009 ± 0.0013	-0.9 ± 0.6
	OCGBH	0.002 ± 0.002	-1.1 ± 0.4
	ΛCDM	11.03 ± 0.08	-0.24 ± 0.07
$\log(\mathcal{M}^*)$	CGBH	11.00 ± 0.09	-0.28 ± 0.07
	OCGBH	10.95 ± 0.09	-0.35 ± 0.08
	ΛCDM	1.1 ± 0.3	-1.5 ± 0.3
α_1	CGBH	0.6 ± 0.3	-1.2 ± 0.4
	OCGBH	0.7 ± 0.2	-1.1 ± 0.3
	ΛCDM	-1.4 ± 0.4	-0.2 ± 0.2
α_2	CGBH	-1.4 ± 0.3	-0.3 ± 0.2
	OCGBH	-1.4 ± 0.4	-0.3 ± 0.2

a pure density evolution seems to be more reasonable, with the most massive galaxies evolving at the same rate as the intermediate mass galaxies and the normalization parameter increasing continuously from $z = 3$ to $z = 1$.

From the two populations analysis, we concluded that the blue galaxies are forming new stars, therefore the massive blue galaxies are necessarily quenched along the cosmic time, and the red galaxies are building faster at $1 < z < 3$. The differences between the GSMF in the standard and the LTB models are small enough to allow the same physical interpretation in the LTB cosmology.

The best-fitting parameters from the double and simple Schechter forms for the blue and red populations in the standard and LTB models are listed in Table 4.4. Following the same analysis considered for the full sample to derive the significance level of the difference between the parameters derived in LTB with respect to the ΛCDM, we find that for blue galaxies it is less than 1σ for all the parameters, with an exception at $1.5 < z < 2.0$ for ϕ_2^* and ϕ_1^* reaching $\sim 2\sigma$ and $\mathcal{M}^*$ showing values of $\sim 2.2\sigma$ for OCGBH.

As for the red galaxies, we assumed a simple Schechter function, Eq. 4.10, which has only three free parameters. For OCGBH, α shows no significant

Table 4.4: Best-fit parameters for double-Schechter function for the blue and red galaxy population adopting three different cosmologies.

BLUE GALAXIES						
ΛCDM model						
z-bin	$\log(\mathcal{M}_{com})$ ($\mathcal{M}_{\odot}$)	$\log(\mathcal{M}^{*})$ ($\mathcal{M}_{\odot}$)	ϕ_1^* (10^{-3} Mpc^{-3})	α_1	ϕ_2^* (10^{-3} Mpc^{-3})	α_2
0.2-0.5	8.40	10.73 ± 0.07	0.57 ± 0.33	-0.87 ± 0.40	0.87 ± 0.17	-1.40 ± 0.12
0.5-0.8	8.85	10.77 ± 0.24	0.29 ± 0.38	-0.50 ± 0.29	0.66 ± 0.30	-1.44 ± 0.05
0.8-1.1	9.15	10.83 ± 0.09	0.46 ± 0.33	-0.83 ± 0.58	0.44 ± 0.27	-1.51 ± 0.13
1.1-1.5	9.41	10.70 ± 0.08	0.40 ± 0.43	-0.93 ± 0.75	0.73 ± 0.38	-1.37 ± 0.13
1.5-2.0	9.77	10.66 ± 0.09	0.61 ± 0.13	-0.23 ± 0.55	0.40 ± 0.13	-1.6
2.0-2.5	10.10	10.78 ± 0.05	0.43 ± 0.08	-0.40 ± 0.24	0.16 ± 0.04	-1.6
2.5-3.0	10.34	10.96 ± 0.20	0.10 ± 0.08	-0.48 ± 1.28	0.11 ± 0.08	-1.6
3.0-4.0	10.40	10.89 ± 0.28	0.005 ± 0.003	1.76 ± 0.57	0.08 ± 0.01	-1.6
CGBH model						
z-bin	$\log(\mathcal{M}_{com})$ ($\mathcal{M}_{\odot}$)	$\log(\mathcal{M}^{*})$ ($\mathcal{M}_{\odot}$)	ϕ_1^* (10^{-3} Mpc^{-3})	α_1	ϕ_2^* (10^{-3} Mpc^{-3})	α_2
0.2-0.5	8.44	10.77 ± 0.15	0.53 ± 0.45	-0.90 ± 0.89	0.73 ± 0.47	-1.40 ± 0.12
0.5-0.8	8.86	10.72 ± 0.15	0.48 ± 0.36	-0.51 ± 0.26	0.65 ± 0.19	-1.46 ± 0.13
0.8-1.1	9.15	10.79 ± 0.13	0.59 ± 0.40	-0.81 ± 0.79	0.46 ± 0.39	-1.53 ± 0.44
1.1-1.5	9.43	10.56 ± 0.07	0.89 ± 0.48	-0.34 ± 0.57	0.96 ± 0.49	-1.43 ± 0.17
1.5-2.0	9.73	10.52 ± 0.05	0.87 ± 0.17	0.17 ± 0.43	0.69 ± 0.15	-1.6
2.0-2.5	10.03	10.75 ± 0.14	0.56 ± 0.18	-0.63 ± 0.93	0.18 ± 0.26	-1.6
2.5-3.0	10.25	11.00 ± 0.22	0.14 ± 0.36	-1.25 ± 1.78	0.08 ± 0.44	-1.6
3.0-4.0	10.34	10.84 ± 0.18	0.005 ± 0.006	1.81 ± 1.10	0.10 ± 0.05	-1.6
OCGBH model						
z-bin	$\log(\mathcal{M}_{com})$ ($\mathcal{M}_{\odot}$)	$\log(\mathcal{M}^{*})$ ($\mathcal{M}_{\odot}$)	ϕ_1^* (10^{-3} Mpc^{-3})	α_1	ϕ_2^* (10^{-3} Mpc^{-3})	α_2
0.2-0.5	8.39	10.64 ± 0.12	1.10 ± 0.55	-0.86 ± 0.23	0.88 ± 0.52	-1.41 ± 0.15
0.5-0.8	8.80	10.66 ± 0.13	0.63 ± 0.40	-0.51 ± 0.29	0.81 ± 0.23	-1.46 ± 0.14
0.8-1.1	9.08	10.75 ± 0.11	0.64 ± 0.54	-0.82 ± 0.93	0.64 ± 0.60	-1.51 ± 0.41
1.1-1.5	9.35	10.50 ± 0.09	1.22 ± 0.37	-0.46 ± 0.62	1.08 ± 0.38	-1.47 ± 0.18
1.5-2.0	9.66	10.44 ± 0.05	1.11 ± 0.21	0.18 ± 0.40	0.89 ± 0.18	-1.6
2.0-2.5	9.95	10.62 ± 0.10	0.73 ± 0.21	-0.36 ± 0.75	0.31 ± 0.25	-1.6
2.5-3.0	10.17	10.78 ± 0.34	0.19 ± 0.16	-0.51 ± 2.38	0.22 ± 0.32	-1.6
3.0-4.0	10.27	10.73 ± 0.15	0.01 ± 0.01	1.49 ± 1.18	0.14 ± 0.06	-1.6

RED GALAXIES						
ΛCDM model						
z-bin	$\log(\mathcal{M}_{com})$ ($\mathcal{M}_{\odot}$)	$\log(\mathcal{M}^{*})$ ($\mathcal{M}_{\odot}$)	ϕ_1^* (10^{-3} Mpc^{-3})	α_1	ϕ_2^* (10^{-3} Mpc^{-3})	α_2
0.2-0.5	8.65	10.86 ± 0.05	1.31 ± 0.22	-0.69 ± 0.09	0.03 ± 0.02	-1.51 ± 0.18
0.5-0.8	9.15	10.87 ± 0.05	0.99 ± 0.16	-0.53 ± 0.08		
0.8-1.1	9.36	10.74 ± 0.05	1.41 ± 0.16	-0.13 ± 0.09		
1.1-1.5	9.56	10.66 ± 0.04	0.63 ± 0.05	0.05 ± 0.09		
1.5-2.0	9.94	10.64 ± 0.04	0.21 ± 0.01	0.13 ± 0.13		
2.0-2.5	10.09	10.59 ± 0.06	0.10 ± 0.01	0.90 ± 0.29		
2.5-3.0	10.29	10.29 ± 0.09	0.004 ± 0.005	3.14 ± 0.97		
CGBH model						
z-bin	$\log(\mathcal{M}_{com})$ ($\mathcal{M}_{\odot}$)	$\log(\mathcal{M}^{*})$ ($\mathcal{M}_{\odot}$)	ϕ_1^* (10^{-3} Mpc^{-3})	α_1	ϕ_2^* (10^{-3} Mpc^{-3})	α_2
0.2-0.5	8.69	10.81 ± 0.07	1.40 ± 0.32	-0.57 ± 0.10	0.03 ± 0.02	-1.51 ± 0.24
0.5-0.8	9.14	10.82 ± 0.04	0.99 ± 0.15	-0.51 ± 0.08		
0.8-1.1	9.35	10.68 ± 0.04	1.56 ± 0.17	-0.10 ± 0.09		
1.1-1.5	9.56	10.63 ± 0.03	0.76 ± 0.05	0.07 ± 0.08		
1.5-2.0	9.94	10.54 ± 0.03	0.28 ± 0.01	0.26 ± 0.13		
2.0-2.5	10.09	10.52 ± 0.05	0.12 ± 0.01	0.93 ± 0.21		
2.5-3.0	10.29	10.22 ± 0.12	0.006 ± 0.003	3.13 ± 0.92		
OCGBH model						
z-bin	$\log(\mathcal{M}_{com})$ ($\mathcal{M}_{\odot}$)	$\log(\mathcal{M}^{*})$ ($\mathcal{M}_{\odot}$)	ϕ_1^* (10^{-3} Mpc^{-3})	α_1	ϕ_2^* (10^{-3} Mpc^{-3})	α_2
0.2-0.5	8.63	10.77 ± 0.05	1.62 ± 0.27	-0.61 ± 0.10	0.04 ± 0.02	-1.53 ± 0.14
0.5-0.8	9.05	10.79 ± 0.04	1.21 ± 0.18	-0.52 ± 0.07		
0.8-1.1	9.26	10.65 ± 0.04	1.90 ± 0.20	-0.13 ± 0.08		
1.1-1.5	9.52	10.60 ± 0.03	0.93 ± 0.07	-0.009 ± 0.08		
1.5-2.0	9.87	10.47 ± 0.02	0.35 ± 0.02	0.26 ± 0.12		
2.0-2.5	10.02	10.43 ± 0.05	0.15 ± 0.02	1.01 ± 0.27		
2.5-3.0	10.21	10.13 ± 0.08	0.007 ± 0.007	3.13 ± 0.91		

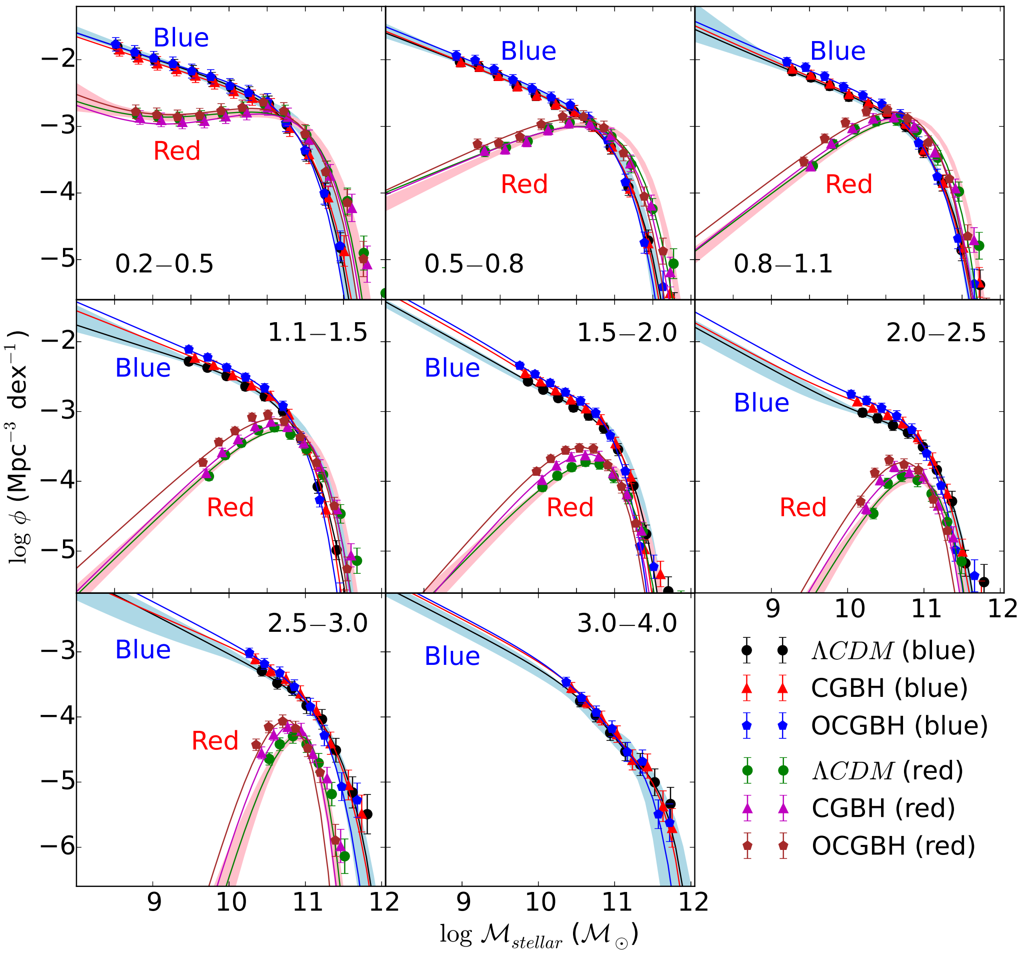

Figure 4.12: Galaxy stellar mass function for the blue galaxy population in the standard (ΛCDM) and void-LTB (CGBH, OCGBH) models. Each panel corresponds to a redshift bin. The blue and pink areas represent the best-fit from Ilbert *et al.* (2013) for the blue and red galaxies, respectively. The solid lines are the best-fit for each cosmological model and galaxy type, and the symbols are as in the legend.

difference ($< 1\sigma$) if compared with the standard results, while $\mathcal{M}^*$ values present a more significant difference ($> 1.2\sigma$) in all redshift bins, especially at $1.5 < z < 2.5$, where it is $\sim 3.8\sigma$. In contrast, ϕ^* presents variations with $1\sigma - 6\sigma$ significance in the same redshift range. For CGBH, the significance level varies from 1σ to 5σ for ϕ^*, for α is always less than 1σ and for $\mathcal{M}^*$ is $< 1\sigma$ for all z-bins except $1.5 < z < 2.0$, where it becomes 2σ. Comparing the results obtained for the two populations we find that the red galaxies are likely to be more affected by the change of cosmology, although the differences found are not large enough to change the global behaviour of the GSMF.

Chapter 5

Galaxy Cosmological Mass Function

"The greatest enemy of knowledge is not ignorance, it is the illusion of knowledge."
Daniel J. Boorstin

This chapter introduces a new function to study the galaxy mass evolution, the GCMF, based on a semi-empirical relativistic approach. The basic quantity for this function is the average galactic mass $\mathcal{M}_g$, which is the average total mass at a given redshift, assuming both baryonic and dark matter content. Although $\mathcal{M}_g$ appears naturally in the equations of relativistic cosmology, its values can only be derived via observational quantities. For such intent, two methods are applied, one combining the observed mass-to-light ratios with the luminosity function data, and an alternative one using the GSMF data. Then, in order to compare both methodologies, we used the FDF galaxy survey dataset. Once $\mathcal{M}_g(z)$ is obtained, the galaxy differential number counts and the GCMF can be calculated.

First, I shall define the galaxy luminosity function and describe the FDF data. Followed by the discussion of the considered approaches to estimate $\mathcal{M}_g(z)$ and the result obtained for this dataset. Then, the galaxy differential number counts in both ΛCDM and LTB cosmological models are presented. Finally, I describe the methodology introduced by Ribeiro & Stoeger (2003), which connects observational quantities such as the galaxy luminosity function to the relativistic theory, and the GCMF derivation. In the last section, I present the results for the GCMF based on FDF data, and a complete analysis of $\mathcal{M}_g$ and GCMF for the UVISTA survey. The results presented in this chapter are summarized in Lopes *et al.* (2014, 2016b).

5.1 Galaxy luminosity and stellar mass functions

From the GSMF, two other quantities can be defined, the stellar mass density given by

$$\rho_*(z) = \int_{\mathcal{M}_{lim}}^{\infty} \mathcal{M}\ \phi(\mathcal{M})\ \mathrm{d}\mathcal{M}, \tag{5.1}$$

and the number density of galaxies

$$n_*(z) = \int_{\mathcal{M}_{lim}}^{\infty} \phi(\mathcal{M})\,\mathrm{d}\mathcal{M}. \tag{5.2}$$

for galaxy stellar masses above a given $\mathcal{M}_{lim}$. If the mass function is fitted by a simple Schechter, Eq. 4.10, the stellar density is reduced to

$$\rho_*(z) = \mathcal{M}^*\ \phi_1^*\ \Gamma\left(\alpha_1 + 2, \frac{\mathcal{M}_{lim}}{\mathcal{M}^*}\right), \tag{5.3}$$

where $\Gamma(a, x)$ is the incomplete gamma integral such that $\lim\limits_{x\to 0}\ \Gamma(a, x) = \Gamma(a)$. The lower mass limit is uncertain and is related to the magnitude limit of the surveyHowever, for the purpose of this thesis, to avoid to be affected by the biases due to selection effects introduced by the limit of the survey, the total number and mass densities were derived by extrapolating the integral to lower masses, independently on redshift. The discussion of the choice of $\mathcal{M}_{lim}$ will be addressed in the next sections.

Similar to the GSMF described in Chapter 4, the galaxy luminosity function $\bar{\phi}(L, z)$ (LF) gives the number density of galaxies with luminosity L at redshift z. In the Schechter's (1976) analytical form it is written as,

$$\bar{\phi}(L)\,\mathrm{d}L = \frac{\bar{\phi}^*}{L^*}\ \left(\frac{L}{L^*}\right)^{\bar{\alpha}}\ \exp\left(-\frac{L}{L^*}\right)\mathrm{d}L = \bar{\phi}(\ell)\,\mathrm{d}\ell, \tag{5.4}$$

or in terms of absolute magnitude,

$$\bar{\phi}(M)\,\mathrm{d}M = 0.4\ln(10)\ \bar{\phi}^*\ 10^{0.4(\bar{M}^*-M)\bar{\alpha}}\ \exp\left[-10^{0.4(\bar{M}^*-M)}\right]\mathrm{d}M, \tag{5.5}$$

where $\ell \equiv L/L^*$, L is the observed luminosity, M is the observed absolute magnitude, L^* is the luminosity scale parameter, $\bar{M}^*$ is the absolute magnitude scale parameter, $\bar{\phi}^*$ is the normalization parameter and $\bar{\alpha}$ is the faint-end slope parameter. These parameters are determined by careful analysis of data from galaxy redshift surveys. The selection function ψ in a given waveband above the lower luminosity threshold ℓ_{lim} is written as,

$$\psi(z) = \int_{\ell_{lim}(z)}^{\infty} \overline{\phi}(\ell)\ \mathrm{d}\ell, \tag{5.6}$$

where

$$\ell_{lim}(z) = \frac{L_{lim}}{\overline{L^*}} = 10^{0.4(\bar{M}^* - M_{lim})}, \tag{5.7}$$

$$M_{lim}(z) = m_{lim} - 5\log[d_L(z)] - 25 + A. \tag{5.8}$$

Here d_L is the luminosity distance, m_{lim} is the limiting apparent magnitude of the survey and A is the reddening correction.

The luminosity density $j(z)$ provides an estimate of the total amount of light emitted by galaxies per unit volume in a given band. It can be obtained from the following integral of the observed LF in a given band,

$$j(z) = \int_{\ell_{lim}(z)}^{\infty} \ell\ \bar{\phi}(\ell)\ \mathrm{d}\ell = L^*\ \bar{\phi}^*\ \Gamma\left(\bar{\alpha} + 2, \frac{L_{lim}}{L^*}\right). \tag{5.9}$$

5.1.1 FORS Deep Field Galaxy Survey dataset

The FDF is a multi-color photometric and spectroscopic survey of a $7' \times 7'$ region near the south galactic pole. The observations were carried out with FOcal Reducer/low dispersion Spectrograph (FORS) on the 8.2-m ESO Very Large Telescope, during 5 observing runs in visitor mode between August and December 1999 for Bessel U, B, R, I and Gunn g bands and 3 photometric nights in October 1999 for NIR filter bands. Other observations of the field using J and K_s filters were also carried out by the ESO NTT telescope. Table 5.1 presents the list of observed filters with its effective wavelength and full width at half maximum. The image quality in the integral image is better than 1" in each filter. A full broad-band photometric catalogue containing about 8700 objects was published by Heidt *et al.* (2003). Fig. 5.1 shows a composite image of the FDF.

The LF was derived by Gabasch *et al.* (2004) using a sample composed of 5558 galaxies selected in the I-band and photometrically measured down to an apparent magnitude limit of $I_{AB} = 26.8$. The photometric redshifts were derived following the technique described in Bender *et al.* (2001), based on the

Table 5.1: Effective wavelength λ_{eff} and full width at half maximum (FWHM) for the bands in the FDF catalogue.

Band	λ_{eff} [nm]	FWHM [nm]
U	366.3	65
B	436.1	89
g	463.9	128
R	640.7	158
I	798.0	154
Band	λ_{eff} [νm]	FWHM [μm]
J	1.25	0.38
K_s	2.16	0.52

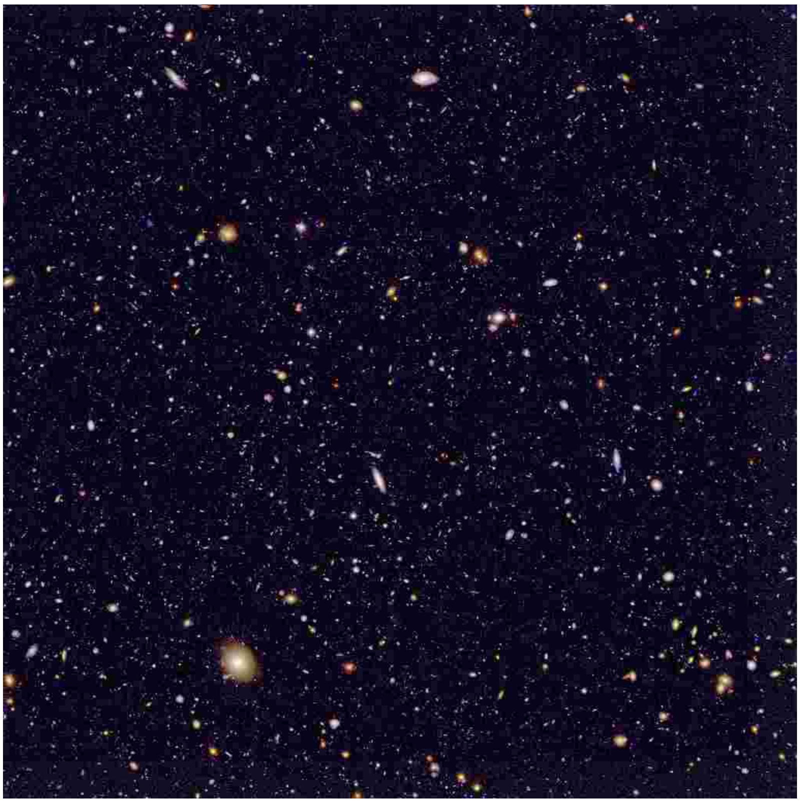

Figure 5.1: BRI composite image of the FDF. This image has been processed to increase the resolution to about 0.4" and to make fainter features visible (Appenzeller *et al.* 2004).

photometry in 9 filters, the 7 bands already mentioned plus z-band from Sloan Deep Sky Survey and a special filter centred at 834 nm, a set of 30 template spectra redshifted between $z = 0$ and $z = 10$, covering a wide range of ages and star formation histories. It was used local galaxy templates from Mannucci *et al.* (2001) and Kinney *et al.* (1996), and semi-empirical templates more appropriate for modest to high redshift galaxies. The semi-empirical templates were constructed by fitting combinations of theoretical spectral energy distributions of different ages from Maraston (1998) and Bruzual & Charlot (1993) with variable reddening (Kinney *et al.* 1994) to the observed broad band colors of about 100 galaxies in the Hubble Deep Field and about 180 galaxies from the FDF with spectroscopic redshifts. A comparison with 362 spectroscopic redshifts z_{spec} shows that the accuracy of the photo-z is $\Delta/(z_{spec}+1) < 0.03$ with only $\sim 1\%$ outliers. The absolute magnitude for a given band of each galaxy in the sample was computed by G04 using the best fitting SED given by the photometric redshift convolved with the appropriate filter function. As the SED fits all 9 observed-frame wavebands simultaneously, possible systematic errors which could be introduced by using K-corrections applied to a single observed magnitude are reduced. The LF is evaluated in the ultraviolet (1500Å and 2800Å), u', B and g' bands within a redshift range $0.5 \leq z \leq 5.0$, and its results fitted by a simple Schechter function. Thus, the evolution of the Schechter parameters M^* and $\bar{\phi}^*$ is investigated by means of the following redshift parameterization equations,

$$\begin{aligned} \bar{M}^*(z) &= \bar{M_0}^* + a\ln(1+z), \\ \bar{\phi}^*(z) &= \bar{\phi_0}^*\,(1+z)^b, \\ \bar{\alpha}(z) &= \bar{\alpha}_0. \end{aligned}$$

For the purpose of this thesis, it is only used the B-band LF given by the $\bar{M_0}^* = -20.92^{+0.32}_{-0.25}$, $a = -1.03^{+0.23}_{-0.28}$, $\bar{\phi_0}^* = 0.0082^{+0.0014}_{-0.0012}$, $b = -1.27^{+0.16}_{-0.19}$, $\bar{\alpha_0} = -1.25 \pm 0.03$.

The GSMF for the same FDF galaxy sample was calculated by Drory *et al.* (2005) and further analyzed by Drory & Alvarez (2008) in the context of the contribution of star formation and merging to galaxy evolution. In these papers the stellar mass-to-light ratios $\mathcal{M}_*/L_B$ and the stellar masses for the galaxies in the catalogue were computed using a log-likelihood-based SED technique, which fits a library of SEDs built with the stellar population evolution model given by Bruzual & Charlot (2003) and Salpeter (1955) IMF to $UBgRIZJK$ multi-color photometry. These $\mathcal{M}_*/L_B$ data were obtained via private communication with Dr. Niv Drory, and they are based in the analysis described in Drory *et al.* (2005). Note that $\mathcal{M}_*/L$ at $z > 2.5$ might be overestimated due to less reliable information on the rest-frame optical colors at young mean ages. The mass function were obtained using the $1/V_{\max}$ method in seven bins from $z = 0.25$ to $z = 5.0$, and then, Drory & Alvarez (2008) fitted a simple Schechter form to the GSMF data and found a set of best fit parameters described in table 5.2. The faint-end slope $\bar{\alpha}$ is constrained to the redshift range $0 < z < 2$ where the authors considered the data to be deep enough and found it to be given by a constant, $\bar{\alpha}(z) = -1.3$. As the data do not allow $\bar{\alpha}$ to constrained at higher redshifts, this value of faint-end slope is extrapolated to $z > 2$.

Table 5.2: Schechter fit parameters to GSMF for the FDF dataset.

z	ϕ^* (h_{70}^3 Mpc^{-3} dex^{-1})	$\log \mathcal{M}^*$ ($h_{70}^{-2}\mathcal{M}_\odot$)	α
0.50	$(2.01 \pm 0.10) \times 10^{-3}$	11.25 ± 0.02	-1.3
1.00	$(1.60 \pm 0.12) \times 10^{-3}$	11.22 ± 0.03	-1.3
1.50	$(1.45 \pm 0.14) \times 10^{-3}$	11.16 ± 0.03	-1.3
2.00	$(9.85 \pm 1.12) \times 10^{-4}$	11.00 ± 0.04	-1.3
2.75	$(9.70 \pm 1.32) \times 10^{-4}$	11.05 ± 0.04	-1.3
3.50	$(6.50 \pm 1.50) \times 10^{-4}$	10.99 ± 0.05	-1.3
4.50	$(2.61 \pm 1.71) \times 10^{-4}$	10.97 ± 0.07	-1.3

5.2 Average galactic mass

The first approach to obtain the average galactic mass $\mathcal{M}_g$ follows the proposal of Ribeiro & Stoeger (2003) for an expression of the mass-to-luminosity ratio at a given redshift value,

$$\frac{\mathcal{M}}{L} = \mathcal{M}_g(z)\frac{\psi(z)}{j(z)}. \tag{5.10}$$

From the observational point of view, LF catalogues only give us information about the stellar mass $\mathcal{M}_*$ and stellar mass-to-light ratio $\mathcal{M}_*/L$ of the galaxies. But, assuming that $\mathcal{M}_*/L$ is proportional to $\mathcal{M}_g/L$, we can write the following expression,

$$\frac{\mathcal{M}_*}{L_B} \propto \frac{\mathcal{M}}{L_B} \propto \mathcal{M}_g(z)\frac{\psi_B(z)}{j_B(z)}. \tag{5.11}$$

Based on the $\mathcal{M}_*/L_B$ for each galaxy in the FDF sample, the average galaxy stellar mass-to-light ratio can be calculated using a subsample of 201 galaxies per redshift bin. Next, one can employ Eq. (5.10) to estimate the average galaxy luminosity in a given passband,

$$L_B \propto \frac{j_B(z)}{\psi_B(z)}, \tag{5.12}$$

and use LF data from the FDF survey to ascertain the general behaviour of the average luminosity in terms of the redshift. Fig. 5.2 shows the results of the average galaxy stellar mass-to-light ratio and the average luminosity in the B-band, which can be described by the following relations (Lopes *et al.* 2014),

$$\mathcal{M}^*/L_B \propto (1+z)^{-1.2\pm0.4}, \tag{5.13}$$

$$L_B \propto (1+z)^{2.40\pm0.03}. \tag{5.14}$$

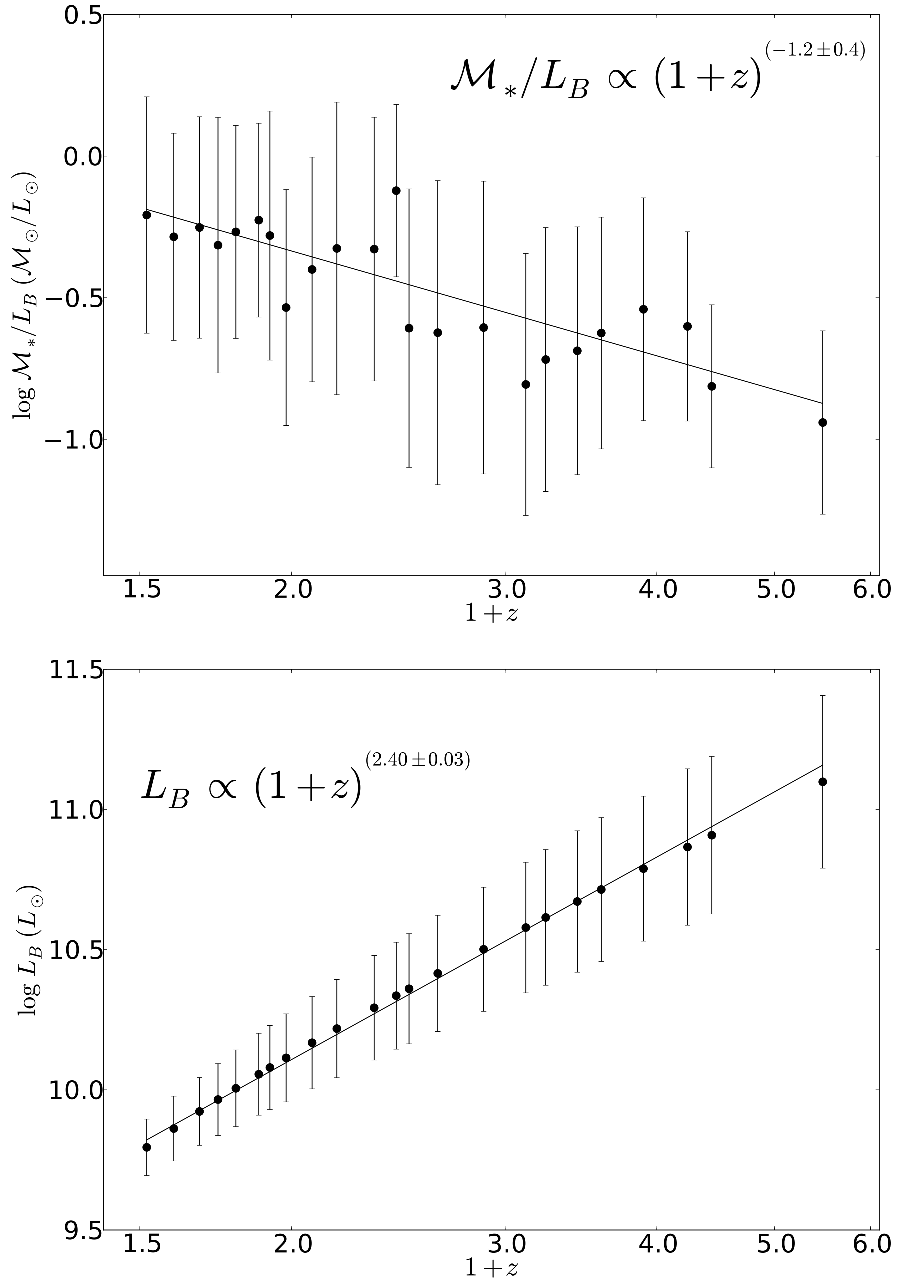

Figure 5.2: *Top panel:* Redshift evolution of the galaxy stellar mass-to-light ratio in the B-band for the FDF data. The graph shows a power-law fit in terms of the redshift. *Bottom panel:* Redshift evolution of the average galaxy luminosity of the FDF dataset in the B-band and its corresponding power law data fit. (Lopes *et al.* 2014)

The error bars for L_B were obtained by Monte Carlo simulations. Hence, Eq. (5.11) allows us to estimate the average galactic mass from the observations,

$$\mathcal{M}_g(z) \propto \frac{\mathcal{M}_*}{L_B}\frac{j_B(z)}{\psi_B(z)}. \tag{5.15}$$

This expression entails that in general the total galactic mass follows its luminous mass evolution, i.e., more dark matter implies more stars when one considers galaxies as a whole and not regions of galaxies, e.g., extended dark matter halos. The previous assumption seems to be reasonable for early-type galaxies, i.e., ellipticals and lenticulars (e.g., Magain & Chantry 2013), however it contrasts with rotation curves from spirals. But, as FDF data do not have any morphological classification, the present approach is suitable to this sample.

The $\mathcal{M}_g$ derived from $\mathcal{M}_*/L_B$ has a dependence on the variation in the spectral type of the galaxy: early-type galaxies have a more tightly constrained masses than late-type ones. So, the resulting $\mathcal{M}_g$ may present a large dispersion due to the lack of morphological classification in the sample. However, at high z the uncertainty in $\mathcal{M}_*/L$ increases as objects drop out in the blue bands and stellar populations become younger. The behaviour of $\mathcal{M}_g$ can be seen in Fig. 5.3, in which the simplest description is as a single power-law, given by

$$\mathcal{M}_g = \mathcal{M}_{g_0}(1+z)^{1.1\pm0.2}, \tag{5.16}$$

where $\mathcal{M}_{g_0} \approx 10^{11}\mathcal{M}_\odot$ is the assumed local value of the average galactic mass (Sparke & Gallagher 2000). Nevertheless, other interpretations than a single power-law are possible because of the large dispersion in $\mathcal{M}_g$.

The average galactic mass can also be derived by following the alternative approach of using quantities derived from GSMF, ρ_* and n_*, which yield the average galactic stellar mass $\mathcal{M}_{stellar}$. Still under the assumption that the total galactic mass evolves as the luminous mass, one may write the following expression,

$$\mathcal{M}_g(z) \propto \mathcal{M}_{stellar}(z) \propto \frac{\rho_*}{n_*}. \tag{5.17}$$

As these quantities depend on the lower mass limit $\mathcal{M}_{lim}$ used in the integration of Eqs. (5.1) and (5.2), in order to check the possible influence of this limit in the results, different values for $\mathcal{M}_{lim}$ are tested. The results are presented in Fig. 5.4 and they clearly show that the various values for $\mathcal{M}_{lim}$ will only affect the amplitude of $\mathcal{M}_{stellar}$, but not its general behaviour.

The goal is to obtain a general form for the average galactic mass, hence assuming that the mass evolves as a power-law one can freely choose a lower mass limit in the calculations. In order to carry out our power-law fitting, it is adopted $\mathcal{M}_{lim} \approx 0$ and $\mathcal{M}_{g_0} \approx 10^{11}\mathcal{M}_\odot$. The results are shown in Fig. 5.5 and the fitted expression is written below,

$$\mathcal{M}_g = \mathcal{M}_{g_0}(1+z)^{-0.58\pm0.22}. \tag{5.18}$$

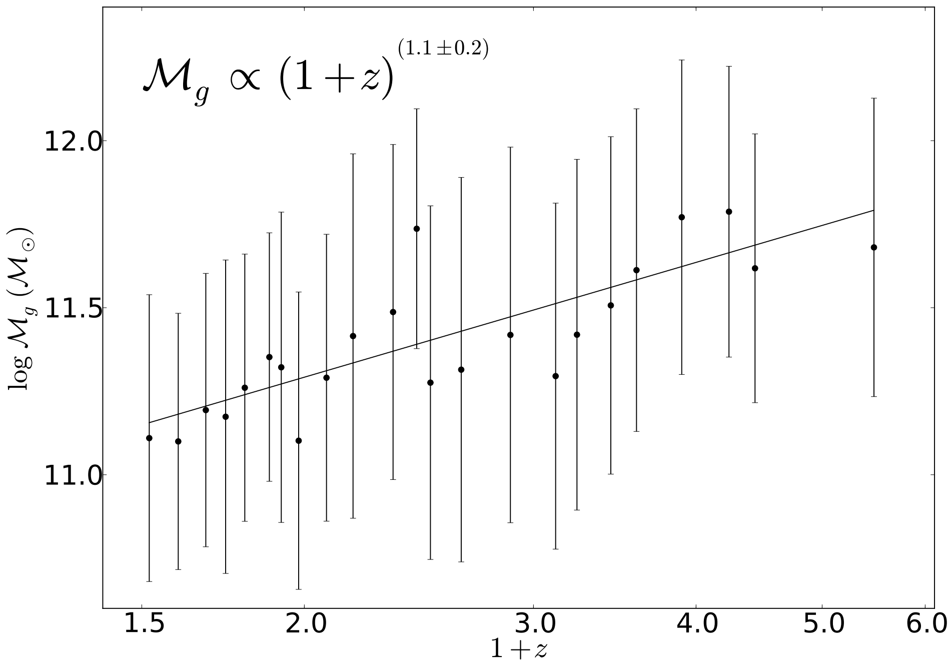

Figure 5.3: Redshift evolution of the average galactic mass for FDF data, using LF and mass-to-light ratio data. As shown in the graph, the data points can be fitted by a mild power law. The coefficient of determination for this fit is $R^2 = 0.64$, where R^2 is a statistical measure of how well the regression line approximates the real data points. It ranges from 0 to 1, and a value of $R^2 = 1$ indicates that the regression line perfectly fits the data. (Lopes *et al.* 2014)

One should note that the negative power index in Eq. (5.18) indicates a growth in mass from high to low redshift values. Indeed, from this equation it can seen that galaxies at $z = 5$ had on average from 25% to 50% of their present ($z = 0$) masses. This growth can be induced by the galaxy mergers within the FDF redshift range, by the star formation history itself, or even by a combination of these two effects. However, one can not disentangle between these two mechanisms using stellar mass data.

Nevertheless, the results using a single survey is uncertain. A more robust estimate would be using more data from different surveys. In the last section, the $\mathcal{M}_g(z)$ is obtained to UVISTA data.

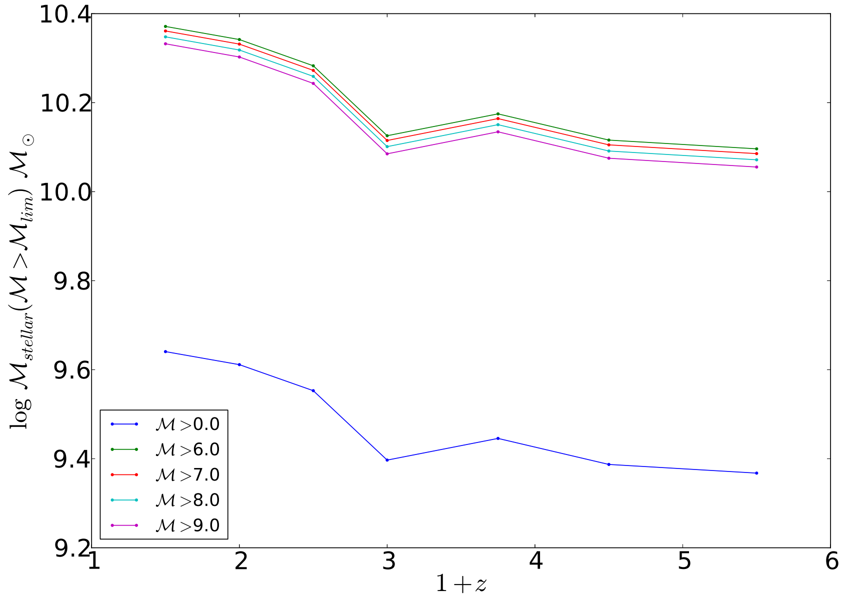

Figure 5.4: Average stellar mass estimated using the GSMF data from FDF sample for different lower mass limits. In this graph the error bars were omitted to emphasize the behaviour of $\log \mathcal{M}_{stellar}$ along the redshift range with different mass limits. (Lopes *et al.* 2014)

5.2.1 Bias related to the method

A comparison between Eq. (5.16) and Eq. (5.18) shows that the two methodologies previously discussed produce very different average galactic mass results. This is may be caused by a combination of effects. The first method depends explicitly on the survey limits, as can be seen in the definition of the selection function and the luminosity density, respectively given by Eqs. (5.6) and (5.9). Moreover, the average mass-to-light ratio can also introduce a bias because one is not able to disentangle the changes in $\mathcal{M}_*/L$ as being due to either real changes of the stellar population with redshift or due to the fact that brighter objects are selected having different $\mathcal{M}_*/L$ values. Regarding the second method, it depends on the limiting mass of the survey, similarly to the first approach, however on this case it only affects the amplitude of $\mathcal{M}_{stellar} \propto \mathcal{M}_g$, as shown in Fig. 5.4. As a last remark, it should be noted that the second approach has less data manipulation, because it only uses the SED fitting results applied to a large range of wavelength observations, while the first one combines LF data and the average galaxy stellar mass-to-light. Therefore, the second method is believed to produce less biased results, and then Eq. (5.18) will be used from this point on.

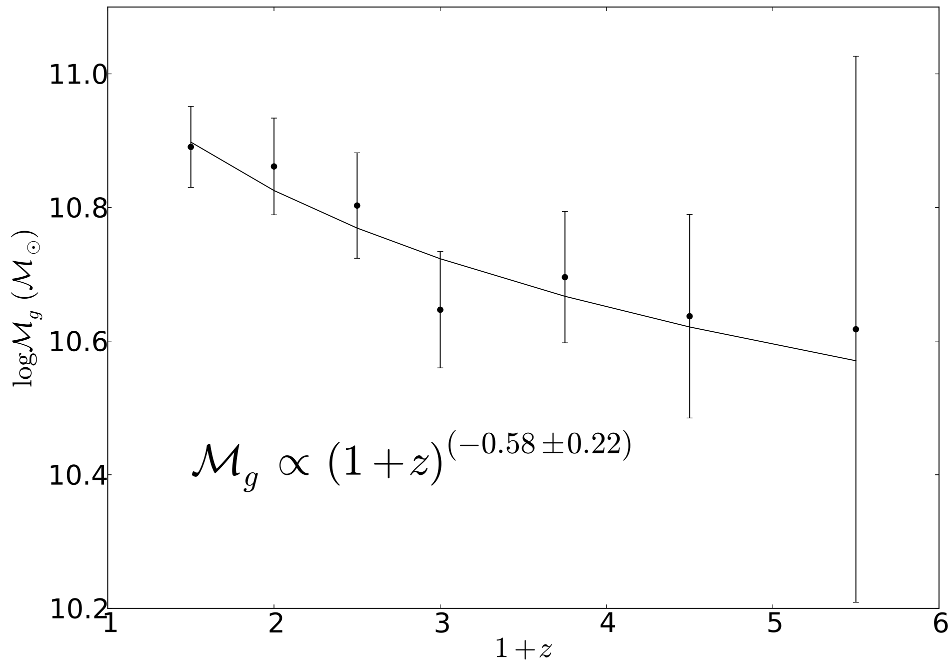

Figure 5.5: Redshift evolution of the average galactic mass for the FDF survey using GSMF data. The plot shows that the data points can be fitted by a mild power law decrease. The coefficient of determination for this fit is $R^2 = 0.84$. (Lopes *et al.* 2014)

5.3 Differential number counts

Ellis (1971) derived a general, cosmological, model-independent relativistic expression for the number count of cosmological sources dN in a volume section at a point P down the null cone given by,

$$dN = (d_A)^2 \mathrm{d}\Omega [n(-k^a u_a)]_P \mathrm{d}y, \tag{5.19}$$

where n is the number density of sources per unit of proper volume in a section of a bundle of light rays converging towards the observer and subtending a solid angle $\mathrm{d}\Omega$ at the observer's position, d_A is the area distance, also known as angular diameter distance, of this section from the observer's viewpoint (also known as angular diameter distance, observer area distance and corrected luminosity distance), u^a is the observer's 4-velocity, k^a is the tangent vector along the light rays, y is the affine parameter distance down the light cone constituting the bundle and dy corresponds to a local distance variation of $(-k^a u_a)dy$ in the rest frame of the galaxy at a point P down the null cone (see Fig. 5.6).

The general definition for the redshift can be written as (Ellis 1971)

$$1 + z = \frac{[u^a k_a]_{source}}{[u^a k_a]_{observer}} = \frac{[u^a k_a]_P}{[u^a k_a]_{C(q)}}. \tag{5.20}$$

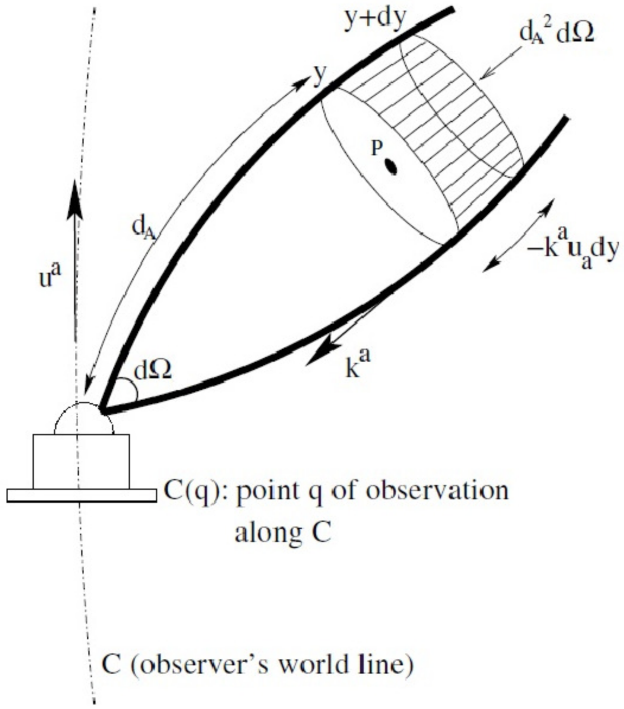

Figure 5.6: Illustration of the relativistic quantities down the light cone (Ribeiro & Stoeger 2003).

Substituting Eq. (5.20) into Eq. (5.19) yields

$$dN = (d_A)^2 d\Omega [n]_P (1+z)[(-k^a u_a)]_{C(q)} dy, \tag{5.21}$$

in which n is related to the matter density ρ_m and the average galactic mass $\mathcal{M}_g$ by means of,

$$n = \frac{\rho_m}{\mathcal{M}_g}. \tag{5.22}$$

5.3.1 Standard cosmology

The general expression 5.21 was specialized to the FLRW cosmology by Iribarrem *et al.* (2012), yielding the following expression,

$$\mathrm{d}N = (d_A)^2 \mathrm{d}\Omega \, n \frac{S}{\sqrt{1-kr^2}} \, \mathrm{d}r. \tag{5.23}$$

Using Eq. (1.11), Eq. (5.22) becomes,

$$n = \left(\frac{3\Omega_{m_0} H_0^2 S_0^3}{8\pi G \mathcal{M}_g} \right) \frac{1}{S^3}. \tag{5.24}$$

Considering $\mathrm{d}\Omega = 4\pi$, Eqs. (1.8), (1.21) and (5.24), Eq. (5.23) can be rewritten as,

$$\frac{\mathrm{d}N}{\mathrm{d}r} = \left(\frac{3 \, c\Omega_{m_0} H_0^2 S_0^3}{2G\mathcal{M}_g} \right) \left[\frac{r^2}{\sqrt{c^2 - H_0^2 S_0^2 (\Omega_0 - 1) r^2}} \right]. \tag{5.25}$$

Following the same approach presented in Chapter 1, where a numerical solution of the scale factor immediately gives a numerical solution for $z(r)$, the differential number counts dN/dz can be obtained by means of the expression,

$$\frac{\mathrm{d}N}{\mathrm{d}z} = \frac{\mathrm{d}N}{\mathrm{d}r}\frac{\mathrm{d}r}{\mathrm{d}S}\frac{\mathrm{d}S}{\mathrm{d}z}. \tag{5.26}$$

These derivatives are taken from Eqs. (1.16), (1.17) and (5.25), which enables Eq. (5.26) to be written as,

$$\frac{dN}{dz} = \left(\frac{3\,c\,\Omega_{m_0} H_0 {S_0}^2}{2G\mathcal{M}_g}\right)\left[\frac{r^2 S^2}{\sqrt{(\Omega_{\Lambda_0})S^4 - {S_0}^2(\Omega_0 - 1)S^2 + (\Omega_{m_0}{S_0}^3)S}}\right]. \tag{5.27}$$

5.3.2 LTB cosmology

Starting from the general expression for the number count of sources derived by Ellis (1971), Ribeiro (1992) obtained

$$dN = 4\pi\, n\, \frac{A' A^2}{f}\, dr, \tag{5.28}$$

where

$$n = \frac{F'}{16\pi G\,\mathcal{M}_g\, A' A^2}. \tag{5.29}$$

The combination of the last two equations yields,

$$\frac{dN}{dr} = \frac{1}{4G\,\mathcal{M}_g}\,\frac{F'}{f}. \tag{5.30}$$

The last equation is essentially a version of the expression derived by Ellis (1971), specialized to the LTB metric. Moreover, this equation can be further specialized to use the Garcia-Bellido & Haugbølle (2008) parametrisation with the best fit values obtained by Zumalacárregui *et al.* (2012), and presented in Chapter 1. For such, Eqs. (1.49) and (5.30) are combined as,

$$\frac{dN}{dz} = \frac{1}{4G\,\mathcal{M}_g}\,\frac{F'[r(z)]}{(1+z)\,\dot{A}'[r(z),t(z)]}, \tag{5.31}$$

and the differential number counts dN/dz is computed for each value of z in the $r(z)$, and $t(z)$ tables, following Chapter 1. A comparison between the estimates for this quantity in the ΛCDM and both CGBH parametrisations in Zumalacárregui *et al.* (2012) can be found in Fig. 5.7.

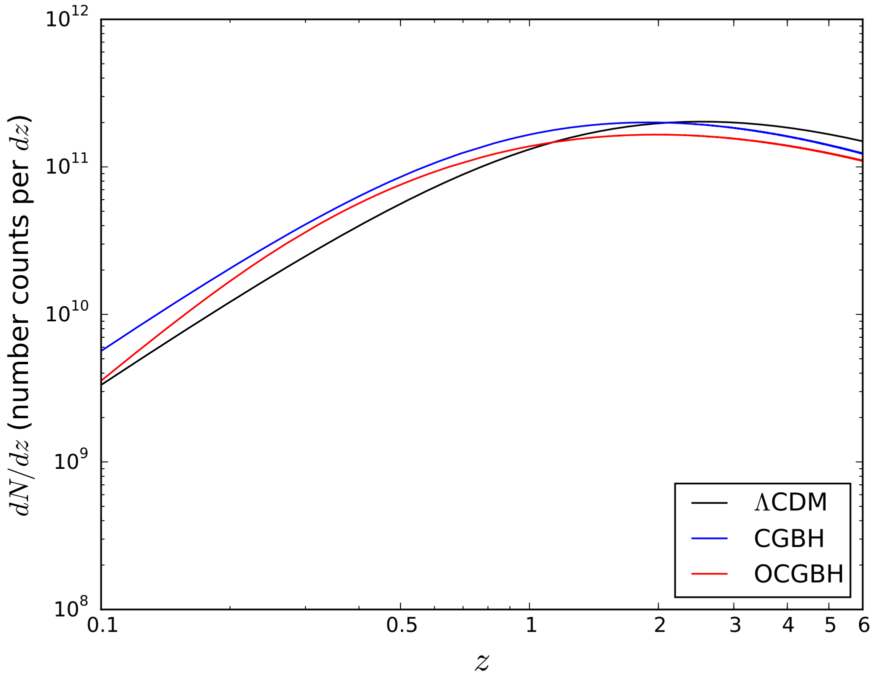

Figure 5.7: Differential number counts estimates using the standard (ΛCDM) and LTB (CGBH, OCGBH) models.

5.3.3 Connecting theory and observations

The differential number counts in the expression (5.27) is directly linked to the underlying cosmological model, since this is a theoretical quantity given by relativistic cosmology. Therefore, in order to write $\mathrm{d}N/\mathrm{d}z$ in terms of observational quantities one uses the methodology developed by Ribeiro & Stoeger (2003), and further extended in Albani *et al.* (2007) and Iribarrem *et al.* (2012), which connects this theoretical quantity to the LF. The link between relativistic cosmology theory and observationally determined LF is achieved by using the *consistency function* $J(z)$ representing the undetected fraction of galaxy counts in relation to the one predicted by theory, as follows,

$$[\mathrm{d}N]_{\mathrm{obs}} = J(z)\,\mathrm{d}N. \tag{5.32}$$

Here the observed differential number counts $[\mathrm{d}N]_{\mathrm{obs}}$ is the key quantity to the analysis, because other quantities require its previous knowledge.

From expressions (1.28) and (5.23), for the ΛCDM model, it can be obtained,

$$dN = (d_A)^2 \mathrm{d}\Omega \left(\frac{n_C}{S^3}\right) \frac{S}{\sqrt{1-kr^2}} \mathrm{d}r. \tag{5.33}$$

Then, to derive $[\mathrm{d}N]_{\mathrm{obs}}$, the observational counterpart of n_C is needed, which is, according to its definition, the selection function ψ. Therefore,

$$[\mathrm{d}N]_{\mathrm{obs}} = (d_A)^2 \mathrm{d}\Omega \left(\frac{\psi}{S^3}\right) \frac{S}{\sqrt{1-kr^2}} \mathrm{d}r. \tag{5.34}$$

The substitution of Eqs. (5.33) and (5.34) into Eq. (5.32) yields,

$$\psi(z) = J(z)\; n_C. \tag{5.35}$$

For the purpose of this thesis, it is more convenient to express the number counts dN in terms of the redshift,

$$\left[\frac{\mathrm{d}N}{\mathrm{d}z}\right]_{\mathrm{obs}} = J(z) \frac{\mathrm{d}N}{\mathrm{d}z}, \tag{5.36}$$

and considering Eq. (5.35), it can be rewritten as,

$$\left[\frac{\mathrm{d}N}{\mathrm{d}z}\right]_{\mathrm{obs}} = \frac{\psi}{n_C}\frac{\mathrm{d}N}{\mathrm{d}z} \quad \Rightarrow \quad \left[\frac{\mathrm{d}N}{\mathrm{d}z}\right]_{\mathrm{obs}} = \frac{V_C}{V_{Pr}}\frac{\psi}{n}\frac{\mathrm{d}N}{\mathrm{d}z}, \tag{5.37}$$

where the two volume definitions appear in the expression above because the relativistic number counts are originally defined in proper volume, so one requires a suitable volume transformation. V_C, V_{Pr}, n_C, n and $\mathrm{d}N/\mathrm{d}z$ are theoretical quantities obtained from the underlying spacetime geometry and, hence, they need to be determined in the chosen cosmological model so that we can obtain the observational differential number counts of Eq. (5.37). The only non-theoretical quantity in this equation is the selection function. In addition, as already discussed in Albani*et al.* (2007) and Iribarrem *et al.* (2012), if we substitute Eqs. (5.24) and (5.27) into Eq. (5.37) the term $\mathcal{M}_g$ cancels out and renders $[\mathrm{d}N/\mathrm{d}z]_{\mathrm{obs}}$ mass independent on first order.

Now, the theoretical differential number counts can be estimated assuming two possible cases for the average galactic mass: $\mathcal{M}_g \approx 10^{11}\mathcal{M}_\odot$ for all redshift ranges and Eq. 5.18. The implications of an evolving average galactic mass on the differential number can be evaluated by substituting both cases in Eq. (5.27). Fig. 5.8 shows the behaviour of the theoretical differential number counts $\mathrm{d}N/\mathrm{d}z$ using a constant and evolving $\mathcal{M}_g$, as well the values of $[\mathrm{d}N/\mathrm{d}z]_{\mathrm{obs}}$. The change from constant to evolving $\mathcal{M}_g$ does not impact in a significant way the general behaviour of $\mathrm{d}N/\mathrm{d}z$. Therefore, assuming a constant value for $\mathcal{M}_g$, as was done in Ribeiro & Stoeger (2003), Albani *et al.* (2007) and Iribarrem *et al.* (2012), can be considered as a very reasonable analytical simplification to the problem and, hence, the conclusions reached by this section holds in general, at least as far as the FDF survey is concerned.

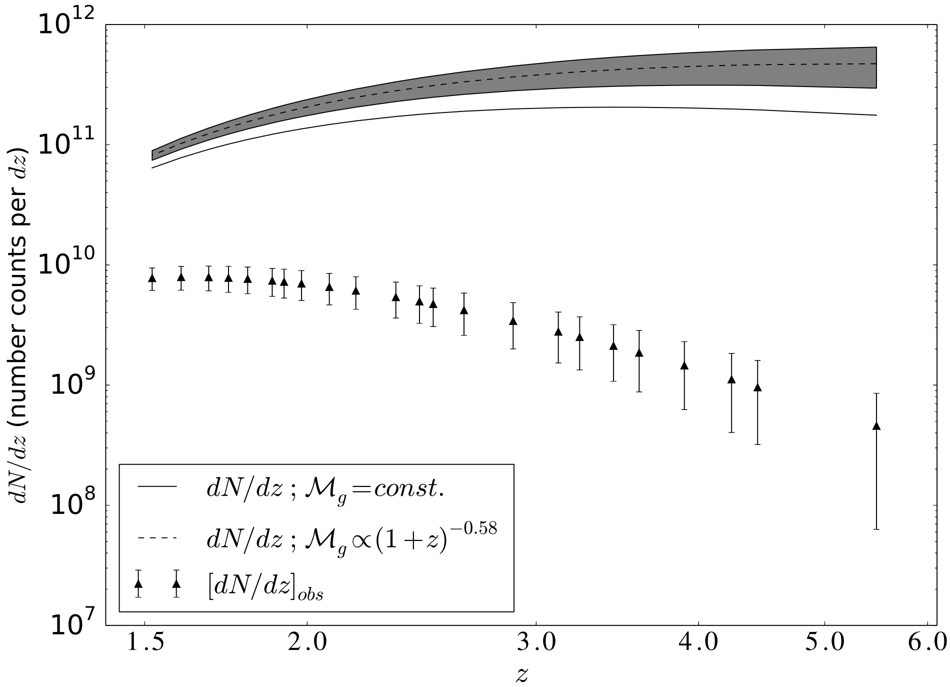

Figure 5.8: Redshift evolution of the theoretical differential number counts using constant and evolving values for $\mathcal{M}_g$, as well as the observational one for FDF data in ΛCDM cosmological model. The constant value used was the assumed local ($z \approx 0$) average galactic mass $\mathcal{M}_g = 10^{11}\mathcal{M}_{\odot}$. Symbols are as in legend and the grey area is the 1σ error of the power index of $\mathcal{M}_g(z)$. (Lopes *et al.* 2014)

5.4 Galaxy cosmological mass function

The GCMF contains information about the galactic number density at a certain redshift in terms of the average galactic mass $\mathcal{M}_g(z)$. It can be defined as follows (Lopes *et al.* 2014),

$$\zeta[\mathcal{M}_g(z), z] \equiv \frac{1}{V_C}\frac{\mathrm{d}N}{\mathrm{d}\left(\log \mathcal{M}_g\right)} = \frac{1}{V_C}\left[\frac{\mathrm{d}\left(\log \mathcal{M}_g\right)}{\mathrm{d}z}\right]^{-1}\frac{\mathrm{d}N}{\mathrm{d}z}. \tag{5.38}$$

Here the GCMF is derived following the standard practice in GSMF calculations, in which the galaxy mass function is written in terms of logarithmic mass and the comoving volume, since it is now standard practice to calculate $\phi(L, z)$ in terms of V_C.

Substituting Eq. (5.36) into Eq. (5.38), the following expression can be written,

$$\zeta(z) = \frac{1}{V_C}\left[\frac{\mathrm{d}\left(\log \mathcal{M}_g\right)}{\mathrm{d}z}\right]^{-1}\frac{1}{J(z)}\left[\frac{\mathrm{d}N}{\mathrm{d}z}\right]_{\mathrm{obs}}. \tag{5.39}$$

Then, it can also be defined the following expression,

$$[\zeta]_{\mathrm{obs}}(z) \equiv \zeta(z)\, J(z) = \frac{1}{V_C}\frac{[\mathrm{d}N/\mathrm{d}z]_{\mathrm{obs}}}{\mathrm{d}\left(\log \mathcal{M}_g\right)/\mathrm{d}z}. \tag{5.40}$$

5.4.1 FDF result

The relationship between the GCMF and $\mathcal{M}_g$ in the FDF sample assuming the standard cosmological model and its redshift dependence can be seen in Fig. 5.9. In this plot, one can note that the GCMF presents negative values, which are not due a logarithmic effect but a consequence of the method used to infer $\mathrm{d}\log\mathcal{M}_g/\mathrm{d}z$. Then, the number density of galaxies whose masses lie in the range $\mathcal{M}_g$, $\mathcal{M}_g+\mathrm{d}\mathcal{M}_g$ and at the redshift range z, $z+\mathrm{d}z$ is actually given by $\zeta\,\mathrm{d}\mathcal{M}_g$, and not simply by the function ζ.

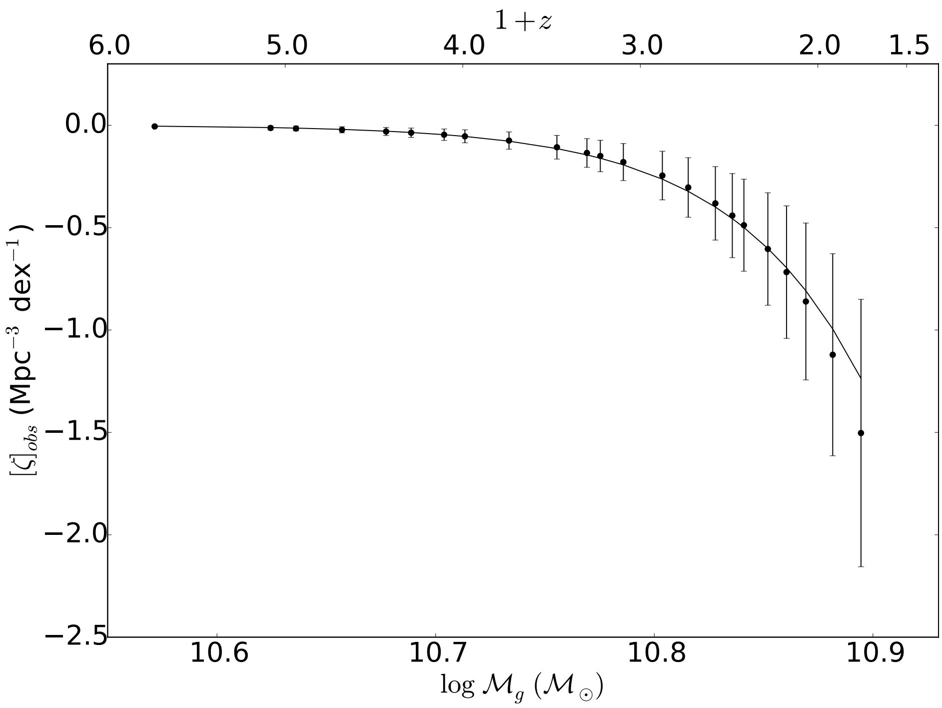

Figure 5.9: This graph shows the galaxy cosmological mass function in terms of the average galactic mass and its corresponding redshift evolution. The best fitted function has $\chi^2 = 0.029$, and its represented by the black solid line. (Lopes *et al.* 2014)

The GCMF data can be fitted by a simple Schechter function, Eq. (4.10), and the best-fit parameters are

$$\phi_1^* = -0.2 \pm 0.5\mathrm{Mpc}^{-3}, \tag{5.41}$$

$$\log\mathcal{M}^* = 10.8 \pm 0.1\mathcal{M}_\odot, \tag{5.42}$$

$$\alpha_1 = 7.5 \pm 0.7. \tag{5.43}$$

Although similar to the GSMF, the $[\zeta]_{\mathrm{obs}}$ is derived using a different approach and therefore, not directly compare to the literature GSMF. Hence, the Schechter parameters from both functions are unrelated. Also a direct comparison between the GSMF (e.g., Drory *et al.* 2004, 2005; Bundy *et al.* 2006; Pozzetti *et al.* 2007) is not possible because in the average mass it is not possible to verify the behaviour of different mass bins, a standard approach used to study the galaxy stellar masses.

The result of the GCMF suggests that on average galaxies were less massive in the past than in the present, a behaviour that agrees with predictions from the "bottom-up" (small objects form first) assembly of dark matter structures in cold dark matter models. It can be also noticed that there is a strong variation on the GCMF between $0.5 < z < 2.0$, which can be interpreted by means of galaxy mergers or by the evolution of the galaxy star formation history itself,as mentioned previously.

As last remarks, one should also keep in mind the limitations of the sample used and that the lack of morphological classification could imply that two or more different types of galaxies may cause different effects in the GCMF. Therefore, more analysis with different datasets needs to be done.

5.4.2 UVISTA results

Here the goal is to apply the same steps introduced in previous sections of this chapter in order to verify the results obtained with FDF data, and evaluate how dependent is the GCMF approach to the dataset selection. These results are part of Lopes *et al.* (2016b). The first step to calculate the GCMF is to derive the stellar mass density and the number density of galaxies using their definitions given by Eqs. (5.1) and (5.2), respectively, and the GSMF results described in Chapter 4. Fig. 5.10 shows the behaviour of these quantities for the full sample assuming ΛCDM, CGBH and OCGBH models. As expected from the GSMF analysis, both of these densities do not present a strong dependence with the cosmological model.

Next, the average galactic mass can be estimated by using Eq. (5.17) and the results presented in Fig. 5.10. As previously done for the FDF survey, the mass is assumed to evolve as a power-law with respect to the redshift. This is shown in Fig. 5.11. The fitted expressions are written as,

$$[\mathcal{M}_g]^{\Lambda CDM} \propto (1+z)^{-0.0208\pm0.0001}; \tag{5.44}$$

$$[\mathcal{M}_g]^{CGBH} \propto (1+z)^{-0.0278\pm0.0001}; \tag{5.45}$$

$$[\mathcal{M}_g]^{OCGBH} \propto (1+z)^{-0.0363\pm0.0001}. \tag{5.46}$$

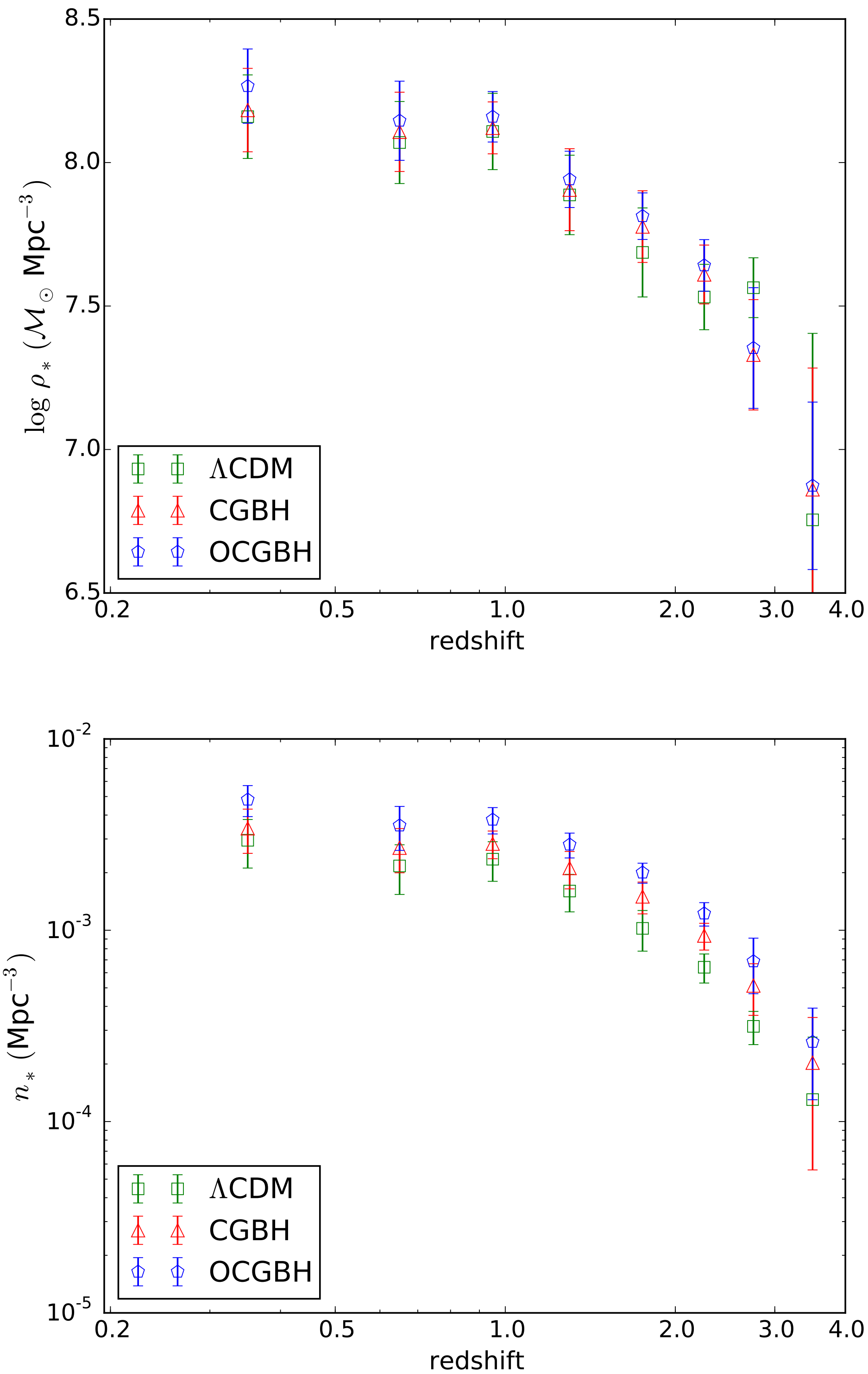

Figure 5.10: Redshift evolution of the stellar mass and number density of galaxies for the UVISTA survey using the GSMF data from the full sample, assuming 3 different cosmologies. (Lopes *et al.* 2016b)

Analyzing this figure, a difference in the indexes when compared to ΛCDM is found to be of about 0.0070 and 0.0155 for CGBH and OCGBH, respectively.

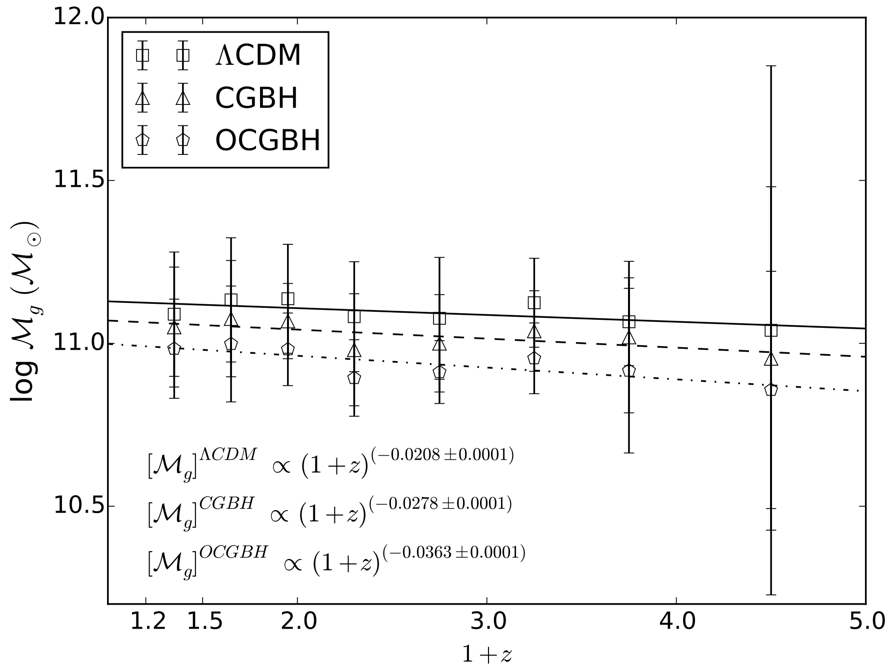

Figure 5.11: Redshift evolution of the average galactic mass for the UVISTA galaxy survey using the GSMF data from the full sample and assuming void-LTB and standard cosmologies. The data points are fitted by a mildly decreasing power law represented by the solid, dashed and dotdash lines for ΛCDM, CGBH and OCGBH, respectively. These results should be compared with the FDF ones shown in Fig. 5.5. (Lopes *et al.* 2016b)

Comparing the results of the standard model between the two datasets, the UVISTA $\mathcal{M}_g(z)$ agrees with the negative power index found for FDF dataset. However, the value of the index is significantly lower in UVISTA, -0.0208 ± 0.0001, as compared to the FDF one, -0.58 ± 0.22, indicating a slower growth in mass from high to low redshift values in UVISTA data. Thus, even if it happens an isolated increase of mass caused by galaxy mergers or by star formation itself, on average, the galactic mass is not greatly affected by it. The differences on the number of galaxies, $\sim 220,000$ for UVISTA and ~ 5558 for FDF, the limiting magnitude of the selected sample, $I_{AB} = 26.8$ for FDF and $K_S = 24$ for UVISTA, and the range of observed redshifts, $0.2 < z < 4.0$ for UVISTA and $0.5 < z < 5.0$, are three of the possible reasons for the different $\mathcal{M}_g(z)$.

The last step before the GCMF is to obtain the observational differential number counts $[\mathrm{d}N/\mathrm{d}z]_{obs}$ given by

$$\left[\frac{\mathrm{d}N}{\mathrm{d}z}\right]_{\mathrm{obs}} = \frac{V_C}{V_{Pr}}\frac{n_*}{n}\frac{\mathrm{d}N}{\mathrm{d}z}, \tag{5.47}$$

which is a variation of Eq. (5.37) with the selection function being replaced by n_*. This can be done because both functions essentially represent the same quantity, the number density of galaxies, as can be seen if one compares Eq. (5.2) with Eq. (5.6). Fig. 5.12 represents $[\mathrm{d}N/\mathrm{d}z]_{obs}$ in the standard and LTB cosmologies. No significant variation is seen on $[\mathrm{d}N/\mathrm{d}z]_{obs}$ from one cosmology to another.

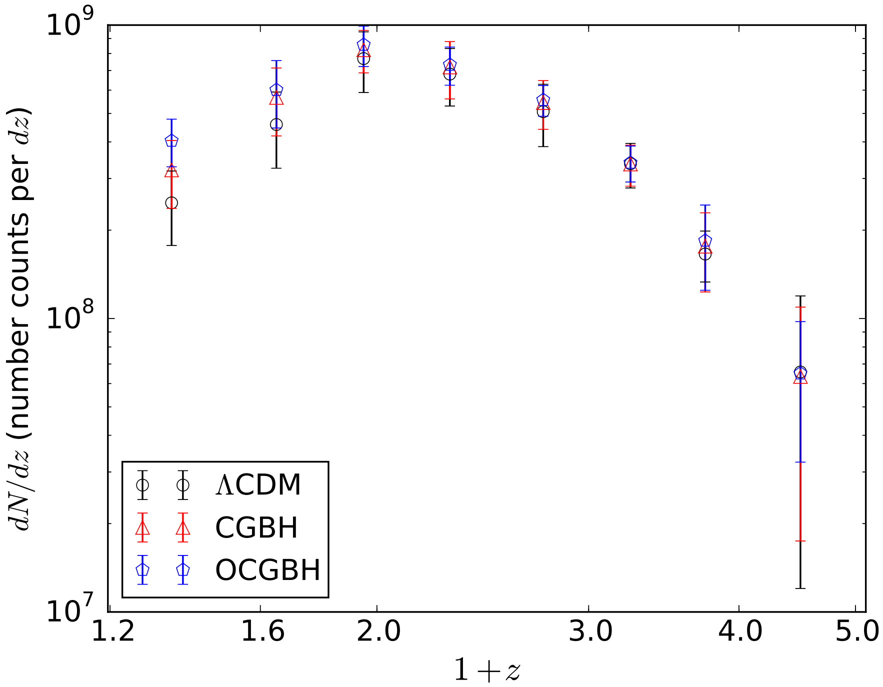

Figure 5.12: Observational differential number counts in the standard (ΛCDM) and LTB (CGBH, OCGBH) cosmological models, based on the UVISTA full sample. Symbols are as in the legend. (Lopes *et al.* 2016b)

Finally, the GCMF can be calculated using Eq. (5.40) and be adjusted by the simple Schechter function, Eq. (4.10). Fig. 5.13 shows $[\zeta]_{obs}$ vs. $\log \mathcal{M}_g$. Similar to FDF GCMF, the UVISTA GCMF also exhibits negative values due to $\mathrm{d}(\mathcal{M}_g)/\mathrm{d}z$, which is derived from Eqs. (5.44) to (5.46).

The best-fit parameters from the Schechter function, Eq. (4.10), assuming different cosmologies are described in Table 5.3. Considering the best-fit parameters and its respective errorbars, for the different cosmological models, there is only a difference on the α parameter.

Table 5.3: Schechter fit parameters to GCMF for the UVISTA dataset and 3 different cosmologies. (Lopes *et al.* 2016b)

Cosmology	ϕ_1^* (Mpc^{-3} dex^{-1})	$\log \mathcal{M}^*$ ($\mathcal{M}_\odot$)	α_1
ΛCDM	-0.2 ± 0.2	10.989 ± 0.04	148 ± 14
CGBH	-0.3 ± 0.3	10.988 ± 0.04	117 ± 10
OCGBH	-0.2 ± 0.3	10.983 ± 0.04	101 ± 10

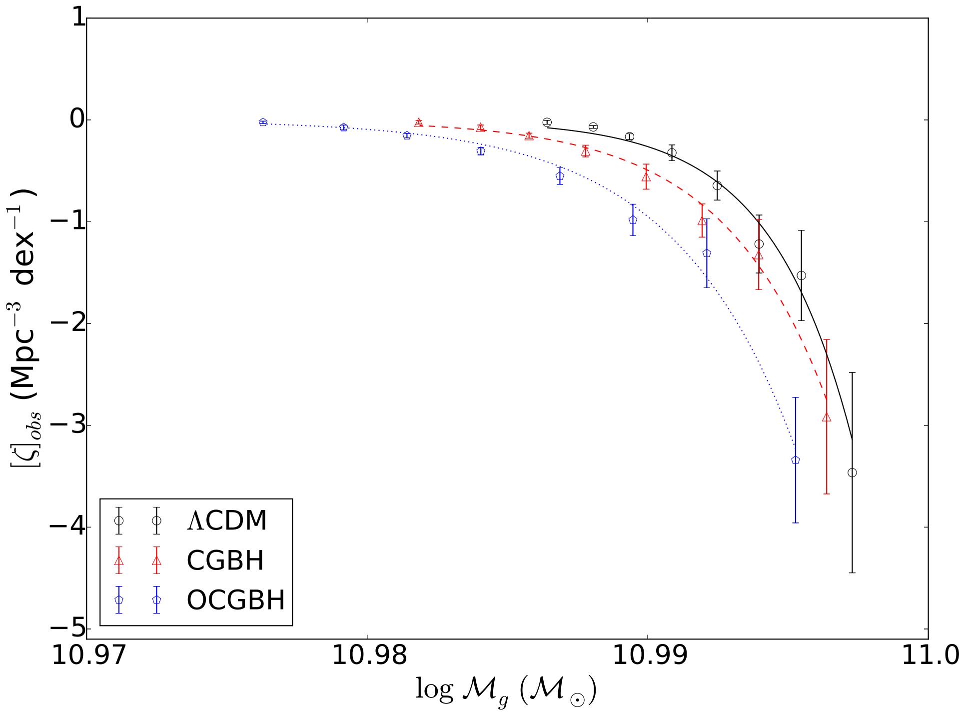

Figure 5.13: Galaxy cosmological mass function in terms of the average galactic mass for different cosmologies and UVISTA data. Symbols are as in the legends. The lines represent the Schechter function with best-fit parameters given in table 5.3.

The comparison between the GCMF derived for UVISTA survey, Fig. 5.13, and the one for FDF, Fig. 5.9, shows a similar behaviour. However a close analysis to the fitted parameters demonstrate a bigger difference among both results, especially related to $\log \mathcal{M}^*$ and α_1. Thus, the general trend agrees with a "bottom-up" assembly of mass found in FDF, but with a significant lower mass range evolution, i.e., the assembly of galactic mass is not strong on an average scale analysis. Moreover, the $\log \mathcal{M}_g$ axis range is significantly different in the two surveys, reflecting the differences on $\mathcal{M}_g(z)$.

From the distinct results from FDF and UVISTA, one concludes that the choice of survey is essential to the analysis.

Conclusions

This thesis studied the mass evolution of galaxies in a cosmological perspective. It follows two distinct approaches. In the first part it is discussed the effects of a change of cosmology on the galaxy stellar mass function (GSMF), while in a second part it is introduced an alternative tool to constrain the galaxy mass evolution, the galaxy cosmological mass function (GCMF). Throughout this text it was used the standard ΛCDM and the void-LTB cosmological models, along with galaxy datasets from the FDF and UVISTA surveys.

Chapter 1 gave the necessary cosmological background information to the analysis. The standard models follows the usual FLRW metric and the parameters are $\Omega_m = 0.3$, $\Omega_\Lambda = 0.7$ and $H_0 = 70$ Mpc/km/s. Regarding LTB cosmology, it is used the constrained models from Garcia-Bellido & Haugbølle (2008) with parametrization made by Zumalacárregui *et al.* (2012) using type Ia supernovae, cosmic microwave background and baryonic acoustic oscillation data.

Chapter 2 summarized important theoretical galaxy formation concepts, while Chapter 3 detailed how the observational photometric data becomes galactic mass.

In Chapter 4 the GSMF was computed for a sample of $\sim 220,000$ galaxies selected in the K_S -band from UVISTA in $0.2 < z < 4$. The stellar mass of these data was calculated assuming ΛCDM and void-LTB models using an alternative version of the open source code *Le Phare*, which allows the physical properties from the galaxies to be estimated from a SED-fitting procedure in different cosmological models. These results enabled us to answer the question about how strong is the dependency of the stellar mass with the cosmology. It was found that the main source of discrepancy is the luminosity distance, which, on average, changes the masses up to $\approx 27\%$ at $z \sim 4$. A secondary quantity that affects the mass is time, although it affects a fewer number of galaxies it can lead to objects with up to $40 - 50\%$ less massive.

Once the stellar masses were calculated, the GSMF was obtained by the $1/V_{max}$ methodology. It was found that for the full sample of galaxies no meaningful difference in double Schechter parameters α_1 , α_2 and ϕ_2^* were seen in the studied redshift range, while $\mathcal{M}^*$ and ϕ_1^* suffer an slightly bigger influence on its values related to the introduction of different cosmologies, but still $< 3\sigma$ significance. These differences are not strong enough to change the shape of the GSMF, and, consequently, the physical interpretation of its behavior.

Additionally, a distinction between red and blue populations were performed and it was verified that the red galaxies seem to be more affected by the change of cosmology than the blue galaxies, probably due to these type of galaxies having more high-mass than low-mass values, and older ages. It was also found an important variation, up to 6σ, on the values of the normalization parameter ϕ_1^* for the red galaxies, but these differences do not affect the shape neither the interpretation of the GSMF for these population.

The conclusion is that any model well constrained by the combination of cosmological observations are enough to yield a robust estimate for the GSMF, especially at lower mass values, $\mathcal{M} < 10^{11}\mathcal{M}_\odot$. Moreover, all conclusions from the GSMF in ΛCDM remain the same in the observationally constrained void-LTB model and in the redshift range studied.

In Chapter 5 it was discussed a semi-empirical relativistic approach capable of calculating the observational GCMF in a relativistic cosmology framework. The GCMF describes the evolution of the average galactic mass $\mathcal{M}_g$. To obtain such quantity, two methodologies were employed, one using luminosity function (LF) and stellar mass-to-light ratio $\mathcal{M}_{stellar}/L$, and another applying GSMF data. In order to verify the differences between the results derived using each approach, it was chosen the B-band LF data described by Gabasch *et al.* (2004) and the GSMF data from Drory & Alvarez (2008) for FDF galaxy survey in the redshift range $0.5 < z < 5.0$. The first method led to a galaxy average luminosity evolution given by $L_B \propto (1+z)^{(2.40\pm0.03)}$ and a stellar mass-to-light ratio power-law behavior, $\mathcal{M}_{stellar}/L_B \propto (1+z)^{(-1.2\pm0.4)}$, that combined resulted in a redshift evolution of the average galactic mass given by $\mathcal{M}_g \propto (1+z)^{(1.1\pm0.2)}$, that is, a power-law behavior with positive power index. Alternatively, the $\mathcal{M}_g(z)$ estimated by means of the GSMF data, resulted in a power law with a negative power index, given by $\mathcal{M}_g \propto (1+z)^{(-0.58\pm0.22)}$. The former approach was considered less reliable because it has more data manipulation, not only on LF but also on $\mathcal{M}_{stellar}/L_B$. This produced more strongly biased results, and the latter result was adopted in latter calculations.

Then, following the technique discussed in Ribeiro & Stoeger (2003), Albani *et al.* (2007), and Iribarrem *et al.* (2012), the observational GCMF can be computed in both standard and LTB cosmological models. For the FDF data the analysis was only made assuming the ΛCDM cosmology, and it was found that the GCMF decreases as the galactic average mass increases. This pattern is well fitted by a Schechter function with very different parameters values from the values found in literature for the GSMF. This general behavior seems to support the prediction of cold dark matter models in which the less massive objects are formed earlier. Moreover, in the range of $0.5 < z < 2.0$ the GCMF varies strongly, which might be interpreted to be a result of a high number of galaxy mergers in more recent epochs or as a strong evolution in the star formation history of these galaxies.

Next, the same approach used in FDF dataset was applied to the full UVISTA sample. The importance of this work was to evaluate the procedure in a different survey with a better statistics, $\sim 220,000$ galaxies while the FDF had ~ 5558. Moreover, there is the possibility of analyzing GCMF for more than one cosmology. The average galactic mass was derived using the GSMF obtained in Chapter 4, finding a power-law behavior with negative index for $\mathcal{M}_g(z)$ in all cosmologies. The difference between the indexes compared to the standard model is of about 0.0070 and 0.0155 for CGBH and OCGBH, respectively. Comparing the results from FDF and UVISTA standard model, one can noticed that the value of the power-law index is significantly lower in the UVISTA, -0.0208 ± 0.0001, than in FDF, -0.58 ± 0.22, which indicates that in UVISTA sample the mass grows slower from high to low redshift values than in the FDF data. Therefore, the conclusion based on UVISTA results is that isolated increase of mass caused by galaxy mergers or by star formation itself, on average, does not affect greatly the galactic mass. The variation of the results from one survey to the other are most probably related to the completeness and statistics of each survey. The FDF dataset is composed of 5558 I-band selected galaxies within an apparent magnitude limit of $I_{AB} = 26.8$ in a redshift range of $0.5 < z < 5.0$, while UVISTA has 220,000 K_S-band selected objects with limiting $K_S = 24$ in a range of $0.2 < z < 4.0$.

Then, the GCMF based on the $\mathcal{M}_g(z)$ derived from UVISTA is estimated and adjusted to a simple Schechter function. Analyzing the best-fit parameters and its respective errorbars, it is found that for the different cosmological models, there is only a difference on the faint-end slope parameter α of the single Schechter function.

The comparison between the GCMF derived for UVISTA survey and the one for FDF shows a similar general behavior but with a $\log \mathcal{M}_g$ axis range significantly different in the two surveys, reflecting the differences on $\mathcal{M}_g(z)$. Therefore, the UVISTA analysis supports the "bottom-up" assembly of mass found in FDF but with a significant lower mass range variation. This means that the UVISTA results may lead to the conclusion that the galactic mass assembly is not strong on an average scale. Also a more detail analysis to the fitted parameters demonstrated a big difference among both results related to $\log \mathcal{M}^*$ and α.

From the distinct results from FDF and UVISTA, one concludes that the choice of survey is essential to the GCMF analysis.

Bibliography

[1] Acquaviva, V., Gawiser, E., Guaita, L. 2011, ApJ, 737, 47

[2] Albani, V.V.L., Iribarrem, A.S., Ribeiro, M.B. & Stoeger, W.R. 2007, ApJ, 657, 760, arXiv:astro-ph/0611032 (**A07**)

[3] Alfedeel, A. H. A. & Hellaby, C. 2010, Gen. Rel. Grav., 42, 1935

[4] Allen, D. A. 1976, MNRAS, 174, 29

[5] Amendola, L., Tsujikawa, S. 2010, Dark Energy: Theory and Observations, Cambridge University Press

[6] Appenzeller, I., Bender, R., Bö, *et al.* 2004, The Messenger, 116, 18

[7] Arnouts, S., Cristiani, S., Moscardini, L., *et al.* 1999, MNRAS, 310, 540

[8] Arnouts, S., Ilbert, O. 2011, LePHARE: Photometric Analysis for Redshift Estimate, astrophysics Source Code Library, ascl:1108.009

[9] Baldry, I.K., Glazebrook, K., Driver, S.P. 2008, MNRAS, 388, 945

[10] Baldry, I.K., Driver, S.P., Loveday, J., Taylor, E.N., *et al.* 2012, MNRAS, 421, 621

[11] Barbaro, G., Poggianti, B. M. 1997, A&A, 324, 490

[12] Bastian, N., Covey, K. R., Meyer, M. R. 2010, ARA&A, 48, 339

[13] Baum, W. A. 1957, AJ, 62, 6

[14] Bender, R., Appenzeller, I., Böhm, A., *et al.* 2001, in ESO/ECF/STScI Workshop on Deep Fields, ed. S. Christiani (Berlin: Springer), 327

[15] Bennett, J.O., Donahue, M.O., Schneider, N. & Voit, M. 2008, The Essential Cosmic Perspective, Addison-Wesley

[16] Bolejko, K., Hellaby, C. & Alfedeel, A. H. A. 2011, J. Cosmology Astropart. Phys., 9, 11

[17] Bolzonella, M., Miralles, J.-M., & Pelló, R. 2000, A&A, 363, 476

[18] Bolzonella, M., Kovac, K., Pozzetti, L., *et al.* 2010, A&A, 524, A76+

[19] Böhringer, H., Chon, G., Bristow, M. & Collins, C. A. 2015, A&A,574, A26

[20] Bondi, H. 1947, MNRAS, 107, 410

[21] Bonnor, W. B. 1972, MNRAS, 159, 261

[22] Boylan-Kolchin, M., Bullock, J. S. & Kaplinghat, M. 2011, MNRAS, 415, 40

[23] Boylan-Kolchin, M., Bullock, J. S. & Kaplinghat, M. 2012, MNRAS, 422, 1203

[24] Brammer, G. B., van Dokkum, P. G., Coppi, P. 2008, ApJ, 686, 1503

[25] Bruzual, G. 2001, ApSSS, 277, 221

[26] Bruzual, G., Charlot, S. 1993, ApJ, 405, 538

[27] Bruzual, G., Charlot, S. 2003, MNRAS, 344, 1000

[28] Bull, P., Clifton, T. & Ferreira, P. G. 2012, Phys. Rev. D, 85, 024002

[29] Bull, P. & Clifton, T. 2012, Phys. Rev. D, 85, 103512

[30] Bundy, K., *et al.* 2006, ApJ, 651, 120

[31] Calzetti, D., Armus, L., Bohlin, R. C., *et al.* 2000, ApJ, 533, 682

[32] Capak, P., Abraham, R. G., Ellis, R. S., *et al.* 2007, ApJS, 172, 99

[33] Caputi, K. I., Cirasuolo, M., *et al.* 2011, MNRAS, 413, 162

[34] Chabrier, G. 2003, PASP, 115, 763

[35] Chaisson, E. & McMillan, S. 2011, Astronomy Today, Pearson Education Inc.

[36] Charlot, S., Bruzual, G. 1991, ApJ, 367, 126

[37] Chiosi, C., Bertelli, G., Bressan, A. 1988, A&A, 196, 84

[38] Cimatti, A., *et al.* 2008, A&A, 482, 21

[39] Clowe, D., Bradac, M., Gonzalez, A. H., *et al.* 2006, ApJ, 648, 109

[40] Cole, D. R., Dehner, W., Wilkinson, M. I. 2011, MNRAS, 416, 1118

[41] Cole, S., Lacey, C. G., Baugh, C. M., Frenk, C. S. 2000, MNRAS, 319, 168

[42] Conroy, C. 2013, ARA&A, 51, 393

[43] Conroy, C., Gunn, J. E., White, M. 2009, ApJ, 699, 486

[44] Copeland, E. J., Sami, M. Tsujikawa, S. 2006, International Journal of Modern Physics D, 15, 1753

[45] Corbelli, E., Palla, F., Zinnecker, H. 2005, The Initial Mass Function 50 Years Later (Dordrecht: Springer)

[46] Dayal, P., Ferrara, A., Dunlop, J. & Pacucci, F. 2014, MNRAS, 445, 2545

[47] De Lucia, G., Springel, V., White, S. D. M, *et al.* 2006, MNRAS, 366, 499

[48] de Putter, R., Verde, L. & Jimenez, R. 2013, J. Cosmology Astropart. Phys., 2, 047

[49] Domínguez-Sánchez, H., Pozzi, F., Gruppioni, C., *et al.* 2011, MNRAS, 417, 900

[50] Drory, N. & Alvarez, M. 2008, ApJ, 680, 41

[51] Drory, N., *et al.* 2004, ApJ, 608, 742

[52] Drory, N., *et al.* 2005, ApJ, 619, L131

[53] Drory, N., Bundy, K., Leauthaud, A., *et al.* 2009, ApJ, 707, 1595

[54] Dubinski, J. & Carlberg, R. G. 1991, ApJ, 378, 496

[55] Eggen, O. J., Lynden-Bell, D., Sandage, A. R. 1962, ApJ, 136, 748

[56] Ellis, G. F. R. 1971, in General Relativity and Cosmology, ed. R.K. Sachs, Proc. Int. School Phys. Enrico Fermi (New York: Academic Press), reprinted in Gen. Rel. Grav., 41, 581, 2009

[57] Ellis, R.S., Abraham, R.G. & Menanteau, F. 2000, Astronomy and Geophysics, vol. 41, p. 2.10.

[58] Ellis, G. F. R. 2007, Gen. Rel. Grav., 39, 1047

[59] Emerson, J. P. & Sutherland, W. J. 2010, Proc. SPIE, 7733, 773306

[60] Eminian, C., Kauffmann, G., Charlot, S., *et al.* 2008, MNRAS, 384, 930

[61] Encyclopedia of Astronomy and Astrophysics, ed. Murdin, P., NY and London: Nature Publishing Group and Institute of Physics Publishing Co., 2001

[62] Etherington, I. M. H. 1933, Phil. Mag. ser. 7, 15, 761; reprinted in Gen. Rel. Grav. 39, 1055, 2007

[63] Faber, S. M. 1972, A&A, 20, 361

[64] February, S., Larena, J., Smith, M. & Clarkson, C. 2010, MNRAS, 405, 2231

[65] Fitzpatrick, E. L. 1985, ApJ, 299, 219

[66] Fontana, A., Salimbeni, S., Grazian, A., *et al.* 2006, A&A, 459, 745

[67] Fontana, A., Santini, P., Grazian, A., *et al.* 2009, A&A, 501, 15

[68] Fontanot, F., *et al.* 2009, MNRAS, 397, 1776

[69] Gabasch, A., *et al.* 2004, A&A, 421, 41

[70] Gallazzi, A., Bell, E. F. 2009, ApJS, 185, 253

[71] García-Bellido, J. & Haugbølle, T. 2008, J. Cosmology Astropart. Phys., 4, 3

[72] Garrison-Kimmel, S., Boylan-Kolchin, M., Bullock, J. S. & Kirby, E. N. 2014, MNRAS, 444, 222

[73] Guidi, G., Scannapieco, C., Walcher, C. J. 2015, MNRAS, 454, 2381

[74] Guo, Y. 2013, ApJS, 207, 24

[75] Heidt, J., Appenzeller, I., Gabasch, A., *et al.* 2003, A&A, 398, 49

[76] Hellaby, C. 2012, J. Cosmology Astropart. Phys., 1, 43

[77] Hellaby, C. & Alfedeel, A. H. A. 2009, Phys. Rev. D, 79, 043501

[78] Hoyle, B., Tojeiro, R., Jimenez, R., *et al.* 2013, ApJL, 762, L9

[79] Hubble, E. P. 1929, Proc. Natl. Acad. Sci. USA, 15, 168

[80] Humphreys, N. P., Maartens, R. & Matravers, D. R. 2012, Gen. Rel. Grav., 44, 3197

[81] Ilbert, O., Arnouts, S., McCracken, H. J., *et al.* 2006, A&A, 457, 841

[82] Ilbert, O., Capak, P., Salvato, M., *et al.* 2009, ApJ, 690, 1236

[83] Ilbert, O., Salvato, M., Le Floc'h, E., *et al.* 2010, ApJ, 709, 644

[84] Ilbert, O., McCracken, H. J., Le Fèvre, O., *et al.* 2013, A&A, 556, A55

[85] Iribarrem, A.S., **Lopes, A.R.**, Ribeiro, M.B. & Stoeger, W.R. 2012, A&A, 539, A112, arXiv:1201.5571

[86] Iribarrem, A., Andreani, P., Gruppioni, C., *et al.* 2013, A&A, 558, A15

[87] Johnson, S. 2013, SATMC: SED Analysis Through Monte Carlo, astrophysics Source Code Library, ascl:1309.005

[88] Jones, M. H., Lambourne, R. 2003, An Introduction to Galaxies and Cosmology, Cambridge: Cambridge University Press

[89] Kajikawa, Y., Yasunari, T. & Wang, B. 2009, Geophys. Res. Lett., 36, 6810

[90] Kannappan, S. J. & Gawiser, E. 2007, ApJL, 657, L5

[91] Keenan, R. C., Barger, A. J. & Cowie, L. L. 2013, ApJ, 775, 62

[92] Kent, S. M. 1986, AJ, 91, 1301

[93] Kinney, A. L., Calzetti, D., Bica, E. & Storchi-Bergmann, T. 1994, ApJ, 429, 172

[94] Kinney, A. L., Calzetti, D., Bohlin, R. C., *et al.* 1996, ApJ, 467, 38

[95] Kirby, E. N., Bullock, J. S., Boylan-Kolchin, M., Kaplinghat, M. & Cohen, J. G. 2014, MNRAS, 439, 1015

[96] Koekemoer, A., *et al.* 2007, ApJS, 172, 196

[97] Komatsu, E., Dunkley, J., Nolta, M. R., *et al.* 2009, ApJS, 180, 330

[98] Komatsu, E., Smith, K. M., Dunkley, J., *et al.* 2011, ApJS, 192, 18

[99] Krasiński, A. 1997, Inhomogeneous Cosmological Models, Cambrigde: Cambrigde University Press

[100] Kriek, M., van Dokkum, P. G., Labbé, I., *et al.* 2009, ApJ, 700, 221

[101] Kroupa, P, 2002, in Astronomical Society of the Pacific Conference Series, Vol. 285, Modes of Star Formation and the Origin of Field Populations, ed. E. K. Grebel & W. Brandner, 86

[102] Kroupa, P., Tout, C. A., Gilmore, G. 1993, MNRAS, 262, 54

[103] Larson, R. B., Tinsley, B. M. & Caldwell, C. N. 1980, ApJ, 237, 692

[104] Lee, H.-c., Worthey, G., Trager, S. C., Faber, S. M., 2007, ApJ, 664, 215

[105] Lee, K.-S., Ferguson, H. C., Wiklind, T., *et al.* 2012, ApJ, 752, 66

[106] Lemaître, G. 1933, Ann. de la Soc. Scient. de Bruxelles, A53, 51

[107] Linde, A. 2014, arXiv:1402.0526

[108] Longhetti, M., Saracco, P. 2009, MNRAS, 394, 774

[109] **Lopes, A.R.**, Iribarrem, A., Ribeiro, M.B. & Stoeger, W.R. 2014, A&A, 572, A27

[110] **Lopes, A.R.**, Gruppioni, C., Pozzetti, L., *et al.* 2016a, MNRAS, submitted

[111] **Lopes, A.R.** & Ribeiro, M.B. 2016b, in preparation

[112] Magain, P. & Chantry, V. 2013, arXiv:1303.6896

[113] Mannucci, F., Basile, F., Poggianti, B. M., *et al.* 2001, MNRAS, 326, 745

[114] Maraston, C. 1998, MNRAS, 300, 872

[115] Maraston, C. 2005, MNRAS, 362, 799

[116] Maraston, C., Pforr, J., Renzini, A., *et al.* 2010, MNRAS, 407, 830

[117] Marchesini, D., van Dokkum, P. G., *et al.* 2009, ApJ, 701, 1765

[118] Marulli, F., Bianchi, D., Branchini, E., *et al.* 2012, MNRAS, 426, 2566

[119] McCracken, H. J., Milvang-Jensen, B., Dunlop, J., *et al.* 2012, A&A, 544, A156

[120] McLure, R.J., *et al.* 2009, MNRAS, 395, 2196

[121] Meures, N. & Bruni, M. 2012, MNRAS, 419, 1937

[122] Milgrom, M. 1983, ApJ, 270, 365

[123] Mobasher, B., Dahlen, T., Ferguson, H. C. 2015, ApJ, 808, 101

[124] Mortlock, A., *et al.* 2011, MNRAS, 413, 2845

[125] Moss, A., Zibin, J.P., Scott, D. 2011, Phys. Rev. D, 83, 103515

[126] Moster, B. P., Somerville, R. S., Newman, J. A. & Rix, H. 2011, ApJ, 731, 113

[127] Mustapha, N., Hellaby, C., Ellis, G. F. R. 1997, MNRAS, 292, 817

[128] Muzzin, A., Marchesini, D., van Dokkum, P.G., *et al.* 2009, ApJ, 701, 1839

[129] Navarro, J. F., Eke, V. R., Frenk, C.S. 1996, MNRAS, 283, 72

[130] Netzer, H. 2009, MNRAS, 399, 1907

[131] Nishikawa, R., Yoo, C.-M. & Nakao, K.-I. 2012, Phys. Rev. D, 85, 103511

[132] O'Connell, R. W. 1976, A&A, 206, 370

[133] Papastergis, E., Giovanelli, R., Haynes, M. P. & Shankar, F. 2015, A&A, 574, 113

[134] Peebles, P. J. E. 2000, ApJ, 534, 127

[135] Peel, A., Ishak, M. & Troxel, M. A. 2012, Phys. Rev. D, 86, 123508

[136] Percival, W. J., Reid, B. A., Eisenstein, D. J., *et al.* 2010, MNRAS, 401, 2148

[137] Pérez-González, P. G., Rieke, G. H., *et al.* 2008, ApJ, 675, 234

[138] Perlmutter, S., Aldering, G., Goldhaber, G., *et al.* 1999, ApJ, 517, 565

[139] Persic, M., Salucci, P., Stel, F. 1996, MNRAS, 281, 27

[140] Pforr, J., Maraston, C., Tonini, C. 2012, MNRAS, 422, 3285

[141] Pickles, A. J. 1985, ApJS, 59, 33

[142] Planck Collaboration I, Planck 2015 results. I. Overview of products and results. 2015, arXiv:1502.01582

[143] Plebánski, J. & Krasiński, A. 2006, An Introduction to General Relativity and Cosmology (Cambridge University Press)

[144] Polletta, M., Tajer, M., Maraschi, L., *et al.* 2007, ApJ, 663, 81

[145] Pozzetti, L., Bolzonella, M., *et al.* 2007, A&A, 474, 443

[146] Pozzetti, L., Bolzonella, M., Zucca, E., *et al.* 2010, A&A, 523, A13

[147] Prevot, M. L., Lequeux, J., Prevot, L., *et al.* 1984, A&A, 132, 389

[148] Pritchet, C. 1977, ApJS, 35, 397

[149] Renzini A., Buzzoni A. 1986, in Astrophysics and Space Science Library, Vol. 122, Spectral Evolution of Galaxies, Chiosi C., Renzini A., eds., pp. 195

[150] Renzini, A., Fusi Pecci, F. 1988, ARA&A, 26, 199

[151] Ribeiro, M. B. 1992, ApJ, 395, 29

[152] Ribeiro, M. B. 1993, ApJ, 415, 469

[153] Ribeiro, M. B. 2005, A&A, 429, 65

[154] Ribeiro, M.B. & Stoeger, W. R. 2003, ApJ, 592, 1, arXiv:astro-ph/0304094

[155] Riess, A. G., Filippenko, A. V., Challis, P., *et al.* 1998, AJ, 116, 1009

[156] Romano, D., Chiappini, C., Matteucci, F., Tosi, M. 2004, arXiv:astro-ph/0409473

[157] Roos, M. 1994, Introduction to Cosmology (Chichester: Wiley)

[158] Salpeter, E. E. 1955, ApJ, 121, 161

[159] Sanders, D. B., Salvato, M., Aussel, H., *et al.* 2007, ApJS, 172, 86

[160] Santini, P., Fontana, A., Grazian, A., *et al.* 2012, A&A, 538, 33

[161] Scalo, J. M. 1986, Fund. Cosmic Phys., 11, 1

[162] Scalo, J. M. 1998, in The Stellar Initial Mass Function, ed. G. Gilmore and D. Howell (San Francisco: ASP), ASP Conference Series, Vol. 142, p. 201

[163] Schechter, P. 1976, ApJ, 203, 297

[164] Schmidt, M. 1968, ApJ, 151, 393

[165] Silk, J. 2011, IAU Symposium: Tracing the Ancestry of Galaxies, 277, 273

[166] Scoville, N., Abraham, R. G., Aussel, H., et. al. 2007, ApJS, 172, 38

[167] Sorba, R., Sawicki, M. 2015, MNRAS, 452, 235

[168] Sparke, L. S., & Gallagher, J. S. 2000, Galaxies in the Universe (Cambridge University Press)

[169] Spinrad, H., Taylor, B. J. 1971, ApJS, 22, 445

[170] Steigman, G. 2002, Fortschritte der Physik, 50, 562

[171] Stoeger, W. R., Stanley, S. J., Nel, D., Ellis, G. F. R. 1992, Class. Quantum Grav., 9, 1711

[172] Tinsley, B. M. 1980, Fund. Cosmic Phys., 5, 287

[173] Tolman, R. C. 1934, Proc. Natl. Acad. Sci. USA, 20, 169

[174] Toomre, A. 1977, ARA&A, 15, 437

[175] Tsujikawa, S. 2010, in Lect. Notes Phys. 800 (Berlin: Springer Verlag), ed. G. Wolschin, 99

[176] Turnrose, B. E. 1976, ApJ, 210, 33

[177] Walker, M. G. & Peñarrubia, J. 2011, ApJ, 742, 20

[178] Wang, H. & Zhang, T.-J. 2012, ApJ, 748, 111

[179] Whitbourn, J. R. & Shanks, T. 2014, MNRAS, 437, 2146

[180] Wuyts, S., Labbé, I., Franx, M., *et al.* 2007, ApJ, 655, 51

[181] Wuyts, S., Franx, M., Cox, T. J., *et al.* 2009, ApJ, 700, 799

[182] Valkenburg, W., Marra, V., Clarkson, C. 2012, MNRAS, 438, L6

[183] Zamojski, M.A., Schiminovich, D., Rich, R.M., *et al.* 2007, ApJS, 172, 468

[184] Zentner, A.R. & Bullock, J.S. 2003, ApJ, 598, 49

[185] Zibin, J.P. & Moss, A. 2011, *Class. Quant. Grav.*, 28, 164005, arXiv:1105.0909

[186] Zumalacárregui, M., García-Bellido, J. & Ruiz-Lapuente, P. 2012, J. Cosmology Astropart. Phys., 10, 9

[187] Zwicky, F. 1933, Helv. Phys. Acta, 6, 110